Multi-Scale, Multi-Compartment Coupled Flow-Oxygen Models of Ischaemic Stroke



Yun Bing

Wadham College

University of Oxford

A thesis submitted for the degree of

Doctor of Philosophy

Michaelmas 2022

Multi-Scale, Multi-Compartment Coupled Flow-Oxygen Models of Ischaemic Stroke

Yun Bing

Abstract

Cerebrovascular accident, also known as stroke, constitutes a major cause of death and disability worldwide. Ischaemic stroke, accounting for 85% of all stroke, occurs when a cerebral artery is occluded. The consequence is a significant reduction of blood flow in the affected region leading to an insufficient supply of oxygen which is vital for the survival of cerebral tissue.

The development of novel therapies for ischaemic stroke has been dependent on experiments in animals, mostly in rats and mice, followed by clinical trials. However, the fundamental differences between the human brain and the rodent brain restrict the translation of therapies from animal to human. Computational physiological models provide a promising alternative for therapy development and improvement, as well as quantitative assessment of individual treatment plans and predicting patient outcome.

The *in silico* clinical trials for treatment of acute ischaemic stroke (INSIST) consortium aims to build a computational framework to simulate acute ischaemic stroke and to evaluate its treatments. In parallel with the INSIST project, this thesis presents a multi-scale, multi-compartment oxygen transport and tissue metabolism model of the human brain, which sets the foundation for estimating treatment outcomes.

The proposed model is coupled to an established circulation model and both take a porous continuum approach. The finite element method is employed for numerical implementation which is verified using the method of manufactured solutions. Effective geometric parameters capturing the micro-scale heterogeneities are obtained using statistically accurate microvascular networks; the maximum consumption rate

of oxygen is optimised to uniquely define the oxygen distribution.

Simulations of healthy state and right middle cerebral artery (R-MCA) occlusion are then carried out on a patient-specific brain mesh. The oxygen predicted lesion appears to be more homogenous and has a larger volume than the one estimated by perfusion alone, possibly due to the effect of oxygen diffusion and metabolism in the tissue. The simulated infarct volume is in qualitative agreement with computed tomography images of a patient who suffered from a R-MCA stroke and compares well to quantitative data reported in the literature.

Acknowledgements

First and foremost, I would like to express my greatest gratitude towards my supervisor, Stephen Payne; not only for his guidance, understanding and belief in my abilities, but also for creating a supportive environment in which I felt encouraged to explore, reflect, and grow. I would also like to extend my sincere thanks to Tamás Józsa who has helped me with various technical aspects of the work, and to Wahbi El-Bouri, with whom I had great pleasure to work during the first year of this project.

For all those who have taken this DPhil journey with me: Ciara, Barbara, Caroline, Miren and Anna, thank you for all your emotional support during a challenging period of time; Daniel, for your invaluable contributions to the project we worked on together; and to all members of 'Payne's gang': our time in the lab may have been cut short by the lockdowns, but those moments will not be forgotten. I also wish to say a belated thank you to my Master's supervisors, Will Coombs and Charles Augarde — if it were not for their inspirations, I would not have pursued a doctoral degree.

I am also grateful to all my amazing friends, especially, Minjie, Susan, Yumo and Yiren, for always being there for me. Last but not the least, the completion of my DPhil studies would not have been possible without the unconditional support from my parents — thank you for always believing in me.

Contents

List of Tables **i**

List of Figures **iii**

1 Introduction **1**

1.1 Ischaemic stroke 1

1.2 Computational modelling of the brain 2

1.3 Aim and objectives 3

1.4 Synopsis 4

2 Literature review **6**

2.1 Introduction 6

2.2 The brain 6

2.2.1 Brain anatomy 6

2.2.2 Vasculature 8

2.2.3 Cerebral tissue 18

2.3 Oxygen transport and metabolism 19

2.3.1 Oxygen 19

2.3.2 Metabolism 23

2.4 Theoretical models 26

2.5 Chapter review 31

3 Multi-compartment models **32**

3.1 Introduction 32
3.2 Circulation model 33
3.3 Oxygen model 36
3.3.1 Model assumptions 36
3.3.2 Model derivation 38
3.4 Chapter review 45

4 Model parameters **46**
4.1 Introduction 46
4.2 Parameters obtained from literature 46
4.3 Geometric parameters 47
4.3.1 Capillary parameters 48
4.3.2 Arteriole parameters 54
4.4 Chapter review 64

5 Numerical implementation **66**
5.1 Finite element method 66
5.2 Manufactured solution 69
5.3 One-dimensional brain tissue column 76
5.3.1 Three-compartment model 78
5.3.2 Two-compartment model 83
5.4 Parameter optimisation 85
5.5 Sensitivity analysis 95
5.6 Chapter review 97

6 Brain model **99**
6.1 Introduction 99
6.2 Simulations of the healthy case 100
6.3 Stroke simulations 103
6.4 Chapter review 115

7 Discussion and conclusion **117**

7.1 Result summary and discussion 117

7.2 Limitation and future work 120

7.2.1 Model 121

7.2.2 Parameters 121

7.2.3 Mesh 125

7.2.4 Future work 126

A Transformation matrix for the permeability tensors **128**

B Source terms of the manufactured solutions **130**

Bibliography **132**

List of Tables

2.1 Diameters of the penetrating arteriolar and venular trunks by classification groups. 10

2.2 Statistics of the microvascular morphometry presented as mean (range). 16

3.1 Parameter values of the flow model. 35

4.1 Oxygen-related parameters values found in the literature. 47

4.2 Mean parameter values of each voxel size. 49

4.3 Best-fit curve coefficients of the capillary parameter means. 50

4.4 Best-fit line coefficients of the standard deviation of capillary parameters. 52

4.5 Comparison between the statistically computed capillary oxygen parameters and the physiological values in the literature. 54

4.6 Simplified expression of the scaled voxel volume (V_{vox}^{s}), trunk vessel length (L_a) and the voxel base area (s_a^2). 59

4.7 Effective volume fraction of all 5 cases for both the 25 $\pm$ 5 μm model and the 25 $\pm$ 10 μm model. 60

4.8 Values of the segment density, original volume fraction and modified volume fraction obtained by the 25 $\pm$ 5 μm model for Case 1 and 4. . 61

4.9 Best-fit curve coefficients of the arteriolar parameter means. 62

4.10 Best-fit line coefficients of the standard deviation of arteriolar parameters. 63

4.11 Comparison between the statistically computed oxygen parameters and the physiological values in the literature. 64
4.12 Values of the geometric oxygen parameters and the REV computed based on the statistically accurate microvasculature. 64

5.1 Mesh convergence study result. 74
5.2 Selected parameter values for the oxygen model. 77
5.3 Volume averaged values of oxygen concentration, partial pressure, saturation, and $CMRO_2$ of the 3-compartment oxygen model in a 1D tissue column with the G_{max} values listed in Table 5.2. 80
5.4 Volume averaged values of oxygen concentration, partial pressure, saturation, and $CMRO_2$ of the 3-compartment oxygen model in a 1D tissue column with no metabolism. 80
5.5 Volume averaged values of oxygen concentration, partial pressure, saturation, and $CMRO_2$ of the 2-compartment oxygen model in a 1D tissue column with metabolic rate taken from Mintun *et al.* 85
5.6 Volume averaged values of oxygen concentration, partial pressure, saturation, and $CMRO_2$ of the 2-compartment oxygen model in a 1D tissue column with metabolic rate taken from An *et al.* 86
5.7 Volume averaged values of oxygen concentration, partial pressure, saturation, and $CMRO_2$ of the 2-compartment oxygen model in a 1D tissue column with optimised metabolic rates. 93
5.8 Range of selected parameters for sensitivity analysis. 96
5.9 Relative percentage change of capillary and tissue concentration. . . . 97

6.1 Results for brain mesh convergence analysis. 103
6.2 Infarct volume estimated by the coupled flow-oxygen model and the perfusion model with $\gamma = 0.004$. 111

List of Figures

2.1 Illustrations of the structure of the brain. 7

2.2 Illustration of the large arterial vessels that supply blood to the brain. 9

2.3 Morphology of the intra-cortical vessels 11

2.4 Depth coded projection (left) and the corresponding skeleton (right) of penetrating vessels and capillary bed. 13

2.5 Vascular density of the cortical depth for human, macaque and marmoset. 14

2.6 Illustrations of the vessel wall structure of artery (left) and vein (right). 17

2.7 Illustration of a neurovascular unit showing the cell associations at the blood brain barrier. 18

2.8 Illustration of a neuron and its components (left) and the brain tissue comprises neurons and glial cells (right). 19

2.9 Theoretical oxygen dissociation curve 20

2.10 Highly simplified cellular metabolism. 24

2.11 Illustration of (a) Krogh model geometry and (b) parallel capillaries with interconnected vessels. 26

2.12 Reconstruction of microvascular oxygen level in rat cortex. 28

2.13 Visualisation of the statistically accurate microvascular networks. . . 30

3.1 A schematic overview of the multi-compartment flow-oxygen model. . 32

3.2 Tangent lines of $\vec{e}_{local}$ representing the local characteristic direction of the penetrating vessels. 35

3.3 Illustration of inter-compartment oxygen transport processes. 36
3.4 Illustration of a compartmental control volume. 39

4.1 A statistically generated capillary network. 48
4.2 Error bar plots of the capillary parameter means against voxel size and their best-fit curves (blue line). 51
4.3 Best-fit curves of the capillary geometric parameters. 53
4.4 Percentage errors of the capillary voxel parameter means. 55
4.5 Examples of randomly generated morphologically accurate arteriolar trees. 56
4.6 ϕ_a distribution of selected tree units from Case 4. 62
4.7 Best-fit curves of the arteriolar geometric parameters. 65

5.1 An illustration of the unit cube. 70
5.2 Visualisation of the manufactured solutions in a unit cube. 71
5.3 Plot of $G_{\max}^{\mathrm{MS}}$ along the sampling line. 72
5.4 Illustrations of the unit cube mesh at different refinement levels. . . . 73
5.5 Plots of mesh convergence. 76
5.6 Simulation results of the 3-compartment oxygen model in a 1D tissue column with the $G_{\max}$ values listed in Table 5.2. 78
5.7 Simulation results of the 3-compartment oxygen model in a 1D tissue column with no metabolism. 81
5.8 Inter-compartment advection coefficients plotted along the sampling line. 82
5.9 Simulation results of the 2-compartment oxygen model in a 1D tissue column with two sets of metabolic rates. 84
5.10 Convergence plots of $G_{\max}$ and cost function (J) of the grey and white matter from a typical optimisation. 92
5.11 Simulation results of the 2-compartment oxygen model in a 1D tissue column with optimised metabolic rates. 93

5.12 Mean values of $P^t_{O_2}$ vs depth for closed and opened skull rats. 95

6.1 Illustrations of the brain mesh. 99

6.2 Healthy simulation results using first-order elements for pressure and discontinuous Galerkin elements for velocity with (a) baseline mesh, (b) locally refined mesh and (c) uniformly refined mesh. 101

6.3 Healthy simulation results using the baseline mesh with (a) p^1v^0 elements, (b) p^1v^1 elements and (c) p^2v^1 elements. 102

6.4 Projection of the perfusion territories of the large arteries on the pial surface. 104

6.5 Pressure distribution post R-MCA occlusion. 104

6.6 Pressure distribution of the arteriole compartment post R-MCA occlusion with various TLC index. 106

6.7 Oxygen concentration distribution post R-MCA occlusion with $\gamma = 0.004$. 107

6.8 Qualitative comparison between CT images of a patient and oxygen simulation results. 109

6.9 Side-by-side comparison between the oxygen lesion based on (a) absolute and (b) relative threshold and (c) the perfusion lesion post R-MCA occlusion with $\gamma = 0.004$. 111

6.10 Distribution of partial pressure of tissue oxygen with various tissue level collateral. 113

6.11 Comparison between reference infarct volumes and simulated infarct volumes with various tissue level collateral. 114

7.1 Relationship between $P^b_{O_2}$ and C_b. 122

7.2 Coronal view of (a) perfusion and (b) capillary oxygen concentration distribution under the healthy condition. 124

7.3 Coronal view of (a) the brain mesh and (b) the MRI image of a healthy subject (IXI025). 126

Chapter 1

Introduction

1.1 Ischaemic stroke

Stroke remains one of the leading cause of death and disability worldwide [1]; the clinical and economical burdens caused by stroke are shown to be high and are likely to grow in the next decades [2,3]. In the UK, stroke incidence is estimated to increase by 60% over a 20-year period (2015-2035) [2]. The total cost of stroke care for people aged 45 and over is projected to be £75 billion in 2035 — an increase of 195% compared to what it was in 2015 [2].

Ischaemic stroke, accounting for approximately 85% of all stroke [4], is characterised by a significant reduction in blood flow caused by cerebral artery occlusions. This leads to an insufficient supply of oxygen and glucose to the brain region downstream of the blockage site. As brain metabolism is almost exclusively dependent on the oxidation of glucose, inadequate production of energy initiates the ischaemic cascade leading to oedema formation, cell death and neurological impairments [5].

Because the cells at the ischaemic core experience irreversible damage within minutes of stroke onset, the main clinical goal is to salvage the tissue around the core that has been supported by collateral flow via reperfusion therapies, i.e., thrombolysis [6] and thrombectomy [7, 8]. While clot dissolving agent is used in thrombolysis to resolve the blockage, thrombectomy removes the blood clot mechanically by a stent

retriever delivered through a catheter. Although these treatments have been proven to increase the proportion of patients with improved functional outcomes [8, 9], their therapeutic windows are limited. These therapies also present the risk of further complications, such as angioedema, haemorrhagic transformation and distal embolisation [10, 11].

The development of novel treatments has been dependent on experimental stroke models in animals, mostly in rats and mice, followed by clinical trials [12]. On average, a single pivotal trial costs over £15 million and the largest cost driving factor is the number of participants required to prove the treatment effects [13]. However, the fundamental differences between the human brain and the rodent brain, such as structural and functional organisations, vascular anatomy and immune systems, cast doubts on the validation of the experimental models, which is reflected in the limited translation of stroke therapies from animal to human [14]. Computational physiological models are promising tools that can help to gain a deeper understanding of the mechanisms underlying stroke and its novel treatments. Upon validation, simulations have the potential to estimate treatment efficacy *a priori* and thus sharpen the focus of future clinical trails [15].

1.2 Computational modelling of the brain

There has been a growing body of research on computational modelling of both the healthy and the diseased brain, such as on the topics of transcranial brain stimulations [16,17], traumatic brain injury [18], oedema formation and propagation [19–21], and decompressive craniectomy [22,23]. More recently, the *in silico* clinical trials for treatment of acute ischaemic stroke (INSIST) consortium developed a computational framework to simulate acute ischaemic stroke (AIS) and to evaluate its treatments [24, 25].

The proposed framework characterises AIS as a series of discrete events that change the condition of virtual patients, e.g., from healthy state to cerebral artery occlusion

followed by treatments. The physiological modelling module currently includes a one-dimensional (1D) large arterial model describing the arterial blood flow from the heart to the pial surface [26], which was extended to include the leptomeningeal circulation [27]. A three-dimensional (3D) multi-scale perfusion model representing the blood flow in the microcirculation [28, 29]. A three-state tissue death model [25, 30], and micro-scale oxygen models investigating the effects of microthrombi on tissue health [30, 31]. Although decreasing in blood flow initiates infarct formation, it is the oxygen level of the cerebral tissue that determines the state of the damage. Despite having an oxygen model at the micro-scale, the modelling module lacks a model that also accounts for the oxygen transport behaviours observed at the organ level which defines the physiological and pathological conditions.

However, such a multi-scale model for oxygen transport in the brain is yet to be developed. The majority of the oxygen transport models rely on discrete networks of the capillary bed, such as the aforementioned micro-scale models [30, 31]. The models that consider the whole microcirculation, however, are lumped compartment models [32–35], which have no spatial variation within the compartments and the micro-scale heterogeneities are neglected.

1.3 Aim and objectives

Despite the recent advancement in computational modelling of cerebral blood flow and metabolism, oxygen distribution post AIS has not been investigated at the organ level. In order to evaluate the impact of stroke treatments on patients' functional outcomes, it is essential for models to include the brain's reaction to oxygen shortage. Therefore, this thesis is set out to develop a multi-scale oxygen transport model for the human brain that captures the response of oxygen distribution to large vessel occlusions.

The objectives of this thesis are listed below:

1. Develop a macro-scale mathematical and computational oxygen transport model

of the human brain. This continuum model should take into account the micro-scale heterogeneities through parameters estimated from microvascular networks.

2. Determine the values of the geometric model parameters, i.e., blood vessel volume fraction and surface area to volume ratio, by analysing well-established micro-scale vascular networks. Estimate the value of the maximum consumption rate of oxygen through optimisation and obtain the remaining parameter values based on literature.

3. Verify the multi-scale oxygen model through the method of manufactured solution. Validate the model using animal and human data from the literature. Quantify the model uncertainties by performing sensitivity analyses with parameter values changed one at a time.

4. Perform ischaemic stroke simulation with right middle cerebral occlusion. Estimate the subsequent special oxygen concentration distribution in the brain.

1.4 Synopsis

The remainder of the thesis is organised as follows. In Chapter 2, an overview of the relevant physiology of the brain is firstly presented with details on the microcirculation. Oxygen transport and metabolism are introduced next with mathematical models for their respective processes. Lastly, current theoretical models of oxygen transport in the brain are reviewed.

Chapter 3 presents the derivation of the multi-scale coupled flow oxygen model. The relevant oxygen transport compartments within the brain are identified first. Due to the coupled nature of the blood flow and oxygen transport, a brief description of the perfusion model is given next. Assumptions of the model are then introduced, simplifying the model into arteriole, capillary and tissue compartments. Finally, the model is derived directly on the macro-scale.

Chapter 4 identifies the effective values of the parameters required in the governing equations. Geometric parameters that capture the micro-scale heterogeneities are computed from statistically accurate microvascular networks and their values are validated against physiological data. The rest of the parameters are either obtained from literature or computed from the perfusion model.

In Chapter 5, the coupled flow-oxygen model is implemented using the finite element method. The numerical implementation is verified using the method of manufactured solutions. A new assumptions is introduced after testing the 3-compartment model on a 1D tissue column, reducing the model to 2 compartments. Volume-averaged equations of the 2-compartment model are then used to optimise the maximum consumption rate of oxygen. Additionally, a sensitivity analysis is carried out to quantify the model uncertainties.

In Chapter 6, the 2-compartment flow-oxygen model is implemented within a patient-specific brain mesh. A convergence test is firstly performed under the healthy conditions. Tissue level collaterals are then introduced to aid the convergence of the stroke simulations. Both qualitative and quantitative comparisons are carried out between the simulation results and clinical data. Lastly, the effects of tissue level collaterals on the infarct volume estimates are analysed.

Finally, Chapter 7 first summaries the findings of the thesis. Then, limitations of the model, how they affect the results and what could be done to minimise their effects are discussed. Last but not least, potential future work is presented.

Chapter 2

Literature review

2.1 Introduction

This chapter provides an overview of the background knowledge on cerebral physiology and a review on existing theoretical models of oxygen transport in the brain. Firstly, a brief introduction of the brain anatomy is presented in Section 2.2.1 followed by a detailed review on the microvasculature in Section 2.2.2. The mechanisms of oxygen transport and metabolism are presented next in Section 2.3. Finally, the theoretical models are discussed in Section 2.4.

2.2 The brain

2.2.1 Brain anatomy

The brain is located in the cranial cavity and protected by the skull and three layers of meninges: the dura mater, the arachnoid mater and the pia mater (Figure 2.1). The space between the arachnoid and pia maters is filled with cerebrospinal fluid (CSF). Not only does the CSF contribute to the removal of metabolic waste and the maintenance of homeostasis [36, 37], it also acts as a shock absorber during mechanical injuries and compensate small change in brain volume [37, 38].

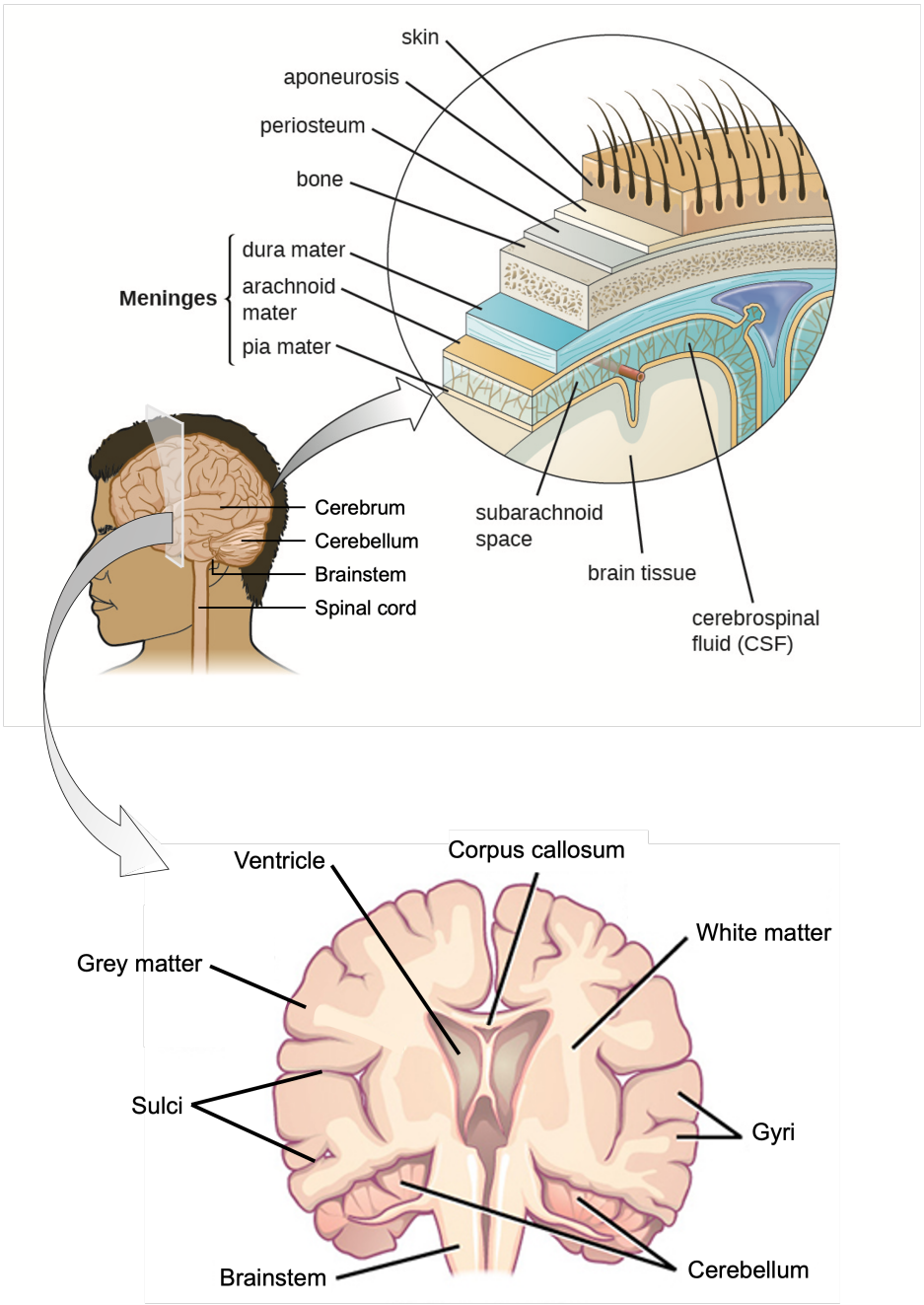


Figure 2.1: Illustrations of the structure of the brain. Top: overview of the main components of the brain with protective layers shown in the expanded circle. Bottom: a slice of the brain in coronal view showing its main features. Adapted with additional annotation from OpenStax [39, 40] under license CC BY 4.0 (https://creativecommons.org/licenses/by/4.0/)

The brain itself has three components: the brainstem, the cerebellum and the cerebrum. The brainstem connects the brain to the spinal cord and provides the latter with sensory inputs and motor outputs [37]. The cerebellum is mainly in charge of coordinating voluntary movements and maintaining balance [37]. The cerebrum, be-

ing the largest of the three, is responsible for the majority of the functions including voluntary motor activities, communication, learning and memory [37].

As shown in Figure 2.1, the cerebrum consists two distinctive layers. The outer layer is the cerebral cortex (grey matter) which has a wrinkled appearance that maximises the surface area of the grey matter within the limited intracranial space. The cortex is divided into two hemispheres (left and right) and connected by a thick fibre bundle — corpus callosum — located in the underlying white matter. Additionally, the cavities enclosed by the brain are the ventricles where CSF is produced.

2.2.2 Vasculature

Cerebral circulation

The brain receives its blood supply through four large vessels, as shown in Figure 2.2, the left and right internal carotid arteries (ICAs) and the left and right vertebral arteries (VAs). The latter two first join together to form the basilar artery (BA) which branches into smaller arteries that supply the brainstem and the cerebellum. The vertebrobasilar system is connected to the ICAs through the circle of Willis, an anastomotic ring of arteries that can preserve the cerebral circulation by providing alternative blood flow pathways if one part of the flow is disrupted. This makes the circle of Willis the primary collateral system of the brain.

The circle of Willis comprises the left and right posterior cerebral arteries (PCAs), the posterior communication arteries, the anterior cerebral arteries (ACAs) and the anterior communicating arteries. Both ACAs and PCAs are major supplies of the cerebrum. While the former feeds the medial region of the frontal and parietal cortices, the latter delivers blood to the inferior and medial surface of the occipital and temporal lobes. Additionally, the left and right middle cerebral arteries (MCAs) are responsible for perfusing large parts of the frontal, temporal and parietal lobes. Figure 2.2 is an illustration of a complete circle of Willis; however, it is worth noting that considerable variations of its structure are found across the population [42, 43].

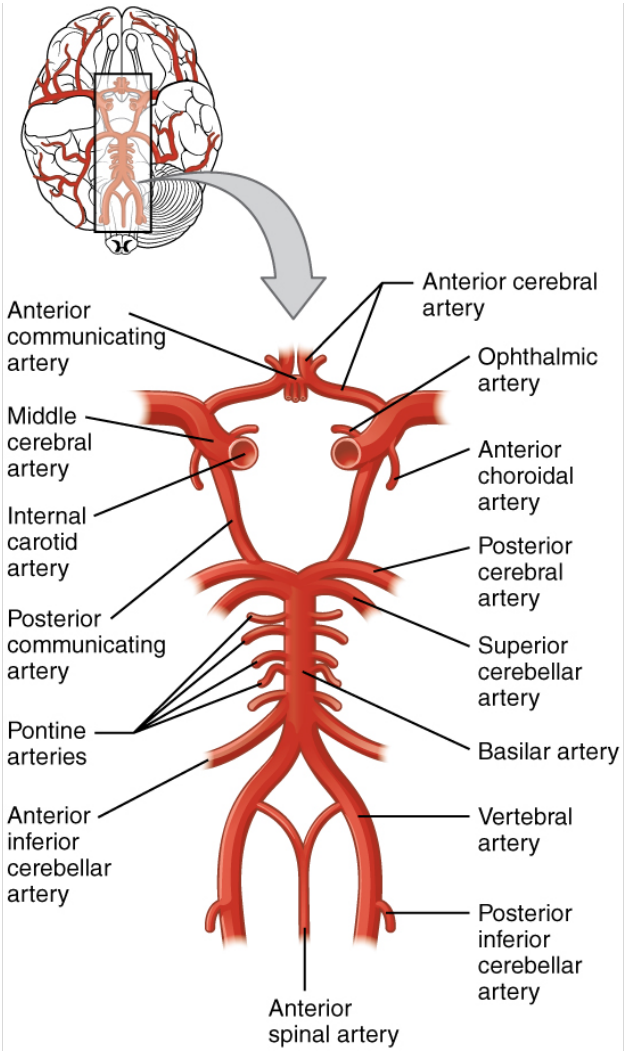


Figure 2.2: Illustration of the large arterial vessels that supply blood to the brain. Reproduced without change from OpenStax [41] under license CC BY 4.0 (https://creativecommons.org/licenses/by/4.0/).

Branches of the six main cerebral arteries run along the cortical surface and form the pial networks, which are located in the subarachnoid space. The pial vessels may form anastomoses, often referred to as leptomeningeal collaterals. These interconnected vessels are part of the secondary collateral system and are shown to reroute blood supply to the territory of an occluded major artery [44]. Diving into the cortex at right angles are the tree-like penetrating arterioles which ramify into a highly interconnected network of small vessels known as the capillary bed. The deoxygenated blood is taken back to the brain surface through the penetrating venules, then to a series of sinuses via the pial veins, and finally back to the heart by the jugular veins.

Penetrating vessels

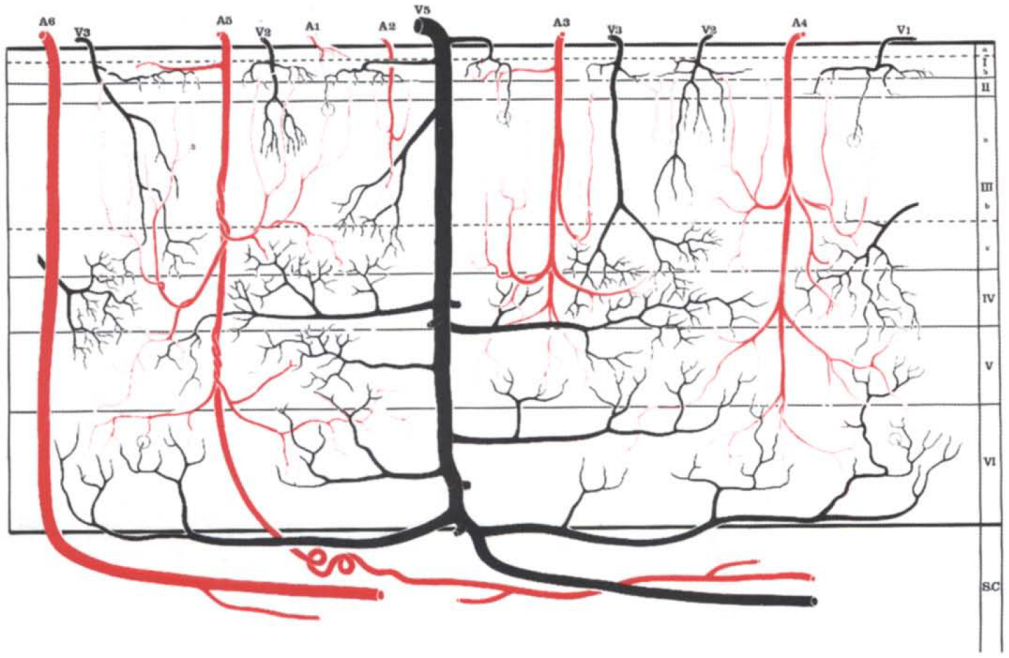
While the large cerebral arteries are often examined using magnetic resonance (MR) or computed tomography (CT) angiography, most of our knowledge on the human microvascular morphology is based on scanning electron micorscopy of Indian ink injected vascular corrosion casts [45, 46]. According to the comprehensive study by Duvernoy *et al.* [45], the penetrating vessels have diameters ranging between 10 [μm] and 240 [μm] and the majority of them penetrate to the middle of the cortex. These tree-like vessels can be classified into 5 groups, based on both their penetration depth and branching patterns, plus a 6th one for the arterioles (Figure 2.3a). Table 2.1 shows the approximate diameters of the penetrating vessels in each group; the venular diameters are larger than that of the arterioles in the same group.

Group	Diameters [μm]	
	Arteriole	Venule
1	10	20
2	15 – 25	30
3	15 – 30	45
4	30 – 40	65
5	30 – 75	120 – 125
6	50 – 240	-

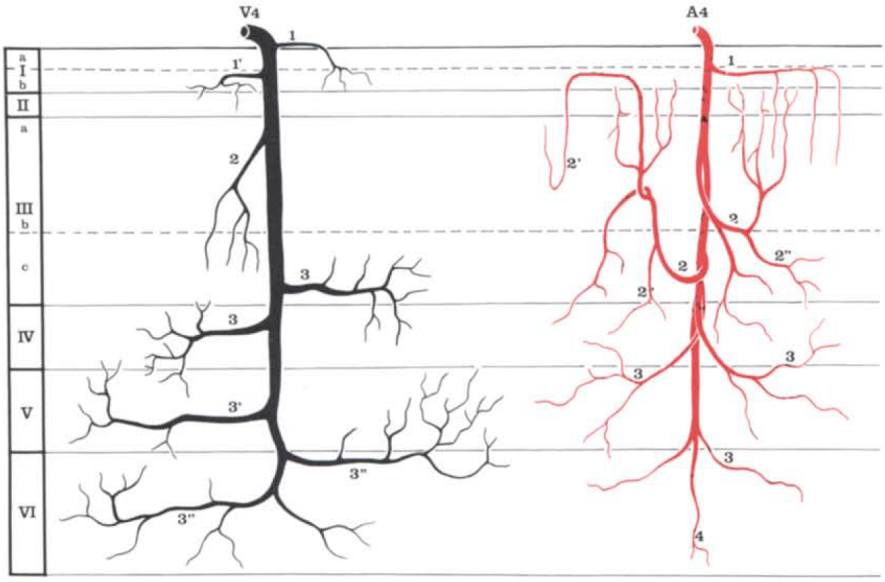
Table 2.1: Diameters of the penetrating arteriolar and venular trunks by classification groups. Data from Duvernoy *et al.* [45].

Although vessels in Group 3 appears to be the most numerous, Group 4 vessels are the most representative [45]. As shown in Figure 2.3b, both the arterioles and venules in this group penetrate to the grey matter and white matter interface. The arteriolar trunk diameters remain constant throughout the cortex; whereas the venular trunks have a slightly tapered shape. As for the branching patterns, the venular branches tend to enter the main trunk at right angles and are found to be longer in the deeper layers with a bush-like arborization. On the other hand, the arteriolar branches can coil around the main trunk for a long distance before developing into recurrent branches that have a candelabra shape. While arterioles from Group 1, 2, 3 and 5

share many similarities with that of Group 4, the Group 6 arterioles are larger in size and only vascularise the white matter.



(a) Classification of penetrating vessels



(b) Typical penetrating vessels

Figure 2.3: Morphology of the intra-cortical vessels: (a) classification of the penetrating arteriolar (A1–A6) and venular (V1–V5) trees and (b) typical penetrating vessels. I–VI: cortical cellular layers. SC: sub-cortical white matter. Reproduced with permission from Duvernoy *et al.* [45].

While the main morphological features of the penetrating vessels have been well delineated, quantitative analysis of the human microvasculature in its three-dimensional

nature had not been conducted until recently [47]. This was due to the limitation of the imaging technologies and computational power in obtaining a sufficiently large volume of cortex with high resolution and processing it [48]. The first study that investigated human microvascular topology was performed by Cassot *et al.* [49]. By utilising confocal laser microscopy and thick sections of human brain from the Duvernoy *et al.* collection [45], they developed an algorithm to acquire the microvascular statistics within a large cortex section [49]. Following this work, parameters such as branching angles, diameter and length distributions, length-to-diameter ratio, vessel length density, vessel volume fraction, vessel surface area-to-volume ratio, tortuosity, and Murray's exponent of both human and non-human primates have been reported in the literature [49–56].

Although only less than 10% of the total number of microvascular vessels is composed of penetrating vessels [52], their volume contributes to approximately half of the total microvascular volume [51,54]. This is because of the square dependence of volume on the radius which is larger in penetrating vessels. While a few studies have analysed the ratio between the number of arterioles and that of venules, which has a value around 2 [52, 55, 57, 58], the volume ratio between the two is still an area of open research. Estimations have been made using a range of lower resolution techniques and a value of $\sim$29% is suggested to be the arteriolar blood volume [47, 59].

In terms of the pial surface distribution of the penetrating vessels, Duvernoy *et al.* noted that there were no paired arterioles and venules, rather, a ring distribution of arterioles surrounding a larger venule was suggested [45]. The same pattern was observed by Adams *et al.* in the superficial layers of macaque primary visual cortex [58]. However, the interconnection between arterioles and venules is more complicated within the cortex.

Blood flow simulations on casts of large microvascular networks have been done to identify the tissue territories fed or drained by arterioles or venules [57,60]. Although neighbouring arterioles and venules were found to be coupled haemodynamically,

the overlap between their territories was not significant from an anatomical point of view [57]. Through the complex capillary network, an arteriole may be connected to a venule even though their pial vessels were far away [57]. This raised to a high convergence between the arteriolar input and venular output; on average, 14 arterioles, instead of 2 as suggested by the arteriole/venule ratio, were drained by one venule [57].

Capillary bed

The capillary bed connects the descending arteries and the ascending venules. Unlike the penetrating trees, the capillary bed is constituted of highly interconnected vessels forming a mesh-like structure (Figure 2.4) and it is generally described as homogeneous on a large scale [47, 61]. This feature gives the capillaries a high robustness (or redundancy) when blood flow is reduced [57]. The reported cut-off values for capillary diameter is approximately 6 [μm] with the upper limit being around 10 [μm] [45, 46, 49, 51, 54, 55].

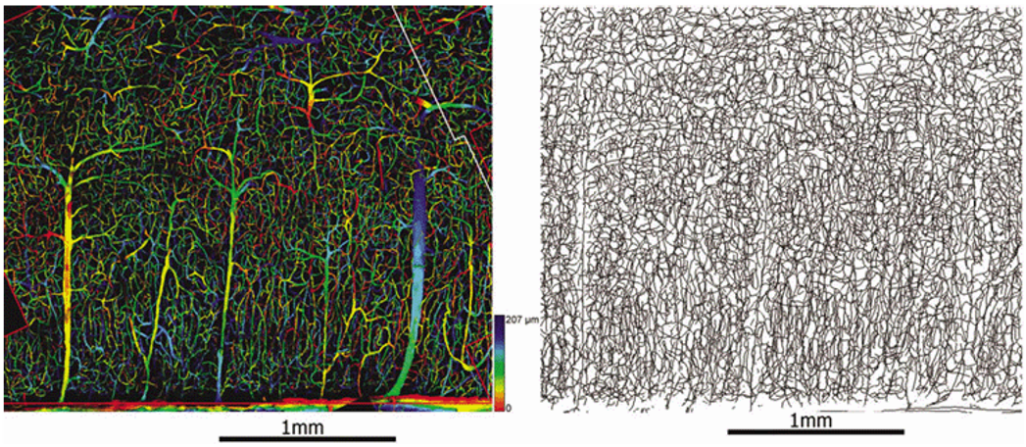


Figure 2.4: Depth coded projection (left) and the corresponding skeleton (right) of penetrating vessels and capillary bed. Reproduced with permission from Cassot *et al.* [49] © 2010 John Wiley & Sons, Ltd.

The characteristic mesh-width of the capillary network, i.e., the intercapillary distance, is 25–75 [μm] [61]. Although the capillary bed is homogenous on a length scale larger than the mesh-width, heterogeneity of its spatial distribution exits not only across different cerebral regions but also through the cortical depth [47–49, 51, 54, 55].

From the marmoset samples analysed by Risser *et al.*, the sensory area appeared strongly vascularised by capillaries (volume fraction=2.36%) in comparison with the integration area (volume fraction=1.60%) [54]. In terms of depth dependent variations, it has been observed in humans that there is a clear band devoid of capillaries in the superficial layer followed by a rough increase on its density which gradually reaches a maximum in the middle third of the cortex [49, 51]. The variations of the microvascular density with respect to both cortical depth and regions are illustrated in Figure 2.5.

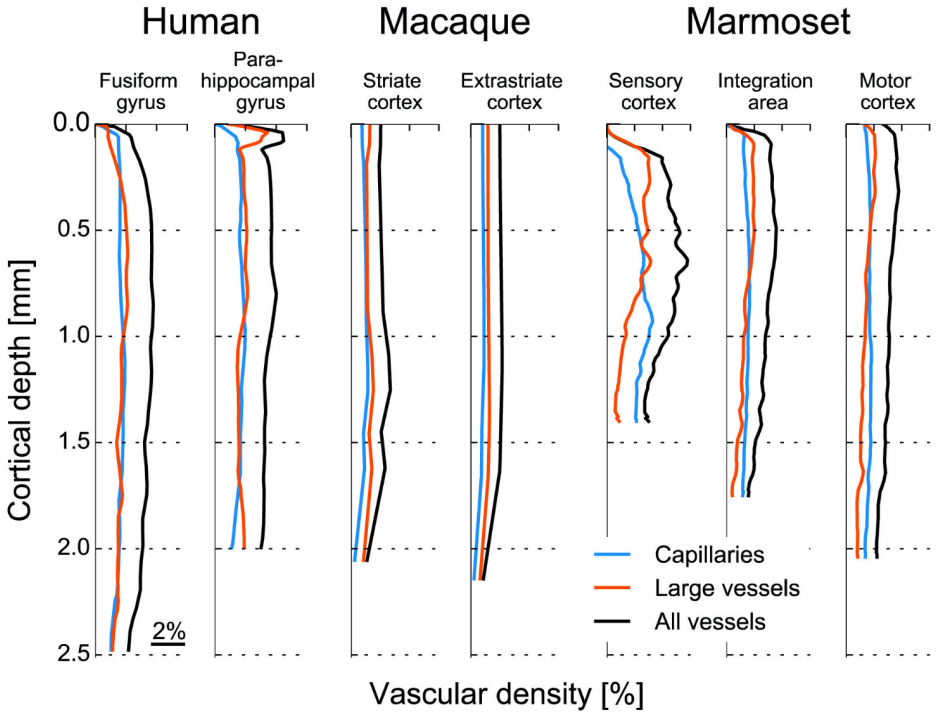


Figure 2.5: Vascular density of the cortical depth for human, macaque and marmoset. The cut off diameters between capillaries and large vessels are 10 [μm], 6 [μm] and 11.2 [μm] for human, macaque and marmoset, respectively. Adapted with permission from Schmid *et al.* [47].

Interestingly, there is also a capillary-free zone around each penetrating arteriole (Pfeifer space) with a radius of approximately 50 [μm] which is in the same order of magnitude as the extravascular distance (mesh-width) [45, 49, 58, 62]. It has been found that the penetrating arterioles directly contribute to tissue oxygenation [63,64] and may be the sole source of oxygen for the capillary-depleted tissue cylinders [62]. Additionally, the popular belief of the positive correlation between cellular density

and vascular density was proved to be weak, especially in the upper cortical layers. On the other hand, a tight relationship was found between metabolic demand and vascular density through COX staining [55].

Similarly to the penetrating vessels, other topological data of the capillary mesh including diameter and length distribution, vessel length density and vessel orientation, were also derived from the reconstructed networks [49, 51]. These parameters are important because not only do they make blood flow and oxygen transport simulations on a physiologically accurate capillary network possible [60, 65], but also allow the development of statistical networks that match these morphological features [66–68].

Microvascular statistics

As the resolution of the current clinical imagining technologies is not able to distinguish the microvasculature from its surroundings, the aforementioned studies are all based on *ex vivo* brains. Although issues, such as tissue shrinkage, incomplete filling of the vessel and artifactual imagine noise, are raised during the sample preparation and segmentation processes [45, 49, 51, 54], these studies have provided valuable insights on the microvascular morphology and topology.

The quantitative analyses of the microvascular architecture are particularly useful as they transform physiological phenomena into statistics which can be used to construct mathematical models of the microcirculation without being restricted by the sample size. Table 2.2 summarises the microvascular statistics that are relevant to the following chapters.

Blood vessels

The structure of blood vessels only varies slightly across different types; all vessel walls have up to three distinct layers enclosing a hollow space (lumen) for blood to flow through. As shown in Figure 2.6, these three layers are the tunica externa (or adventitia) comprising mostly elastin and collagen, the tunica media consisting

	Unit	Cassot *et al.* [49]	Lauwers *et al.* [51]	Risser *et al.* [54]	Weber *et al.* [55]
Species	-	Human	Human	Marmoset	Macaque
Capillary cut-off diameter	[μm]	9	10	11.2	8
Mean capillary diameter	[μm]	6.24	6.47	-	5.53 (5.43–5.61)
Mean large vessel diameter	[μm]	-	-	15.2 (14.70–15.88)	10.23 (10.16–10.37)
Mean overall vessel diameter	[μm]	7.32	7.82	9.40 (8.34–9.88)	7.36 (7.15–7.45)
Capillary volume fraction	[%]	1.27*	1.35*	1.53 (0.92–2.36)†	0.88 (0.83–0.97)
Large vessel volume fraction	[%]	-	-	1.21 (0.48–1.94)†	1.23 (1.19–1.29)
Overall vessel volume fraction	[%]	2.44 (2.43–2.45)	2.7 (2.39–3.02)	2.74 (2.02–4.30)	2.14 (2.03–2.22)
$\frac{\text{Vessel surface area}}{\text{Sample volume}}$	$\left[\frac{\text{mm}^2}{\text{mm}^3}\right]$	5.37 (5.33–5.42)	11.74 (10.19–12.85)	7.87 (5.32–11.32)	10.97 (10.25–11.50)
$\frac{\text{Vessel volume}}{\text{Vessel surface area}}^{\dagger}$	[μm]	4.55 (4.53–4.56)	2.3 (2.1–2.4)	3.43 (2.56–3.91)	1.95 (1.93–1.98)

Table 2.2: Statistics of the microvascular morphometry presented as mean (range). * values obtained by interpreting the figures provided in the literature; † values calculated using the data provided in the literature.

mainly the smooth muscle cells and the tunica intima containing primarily endothelial cells.

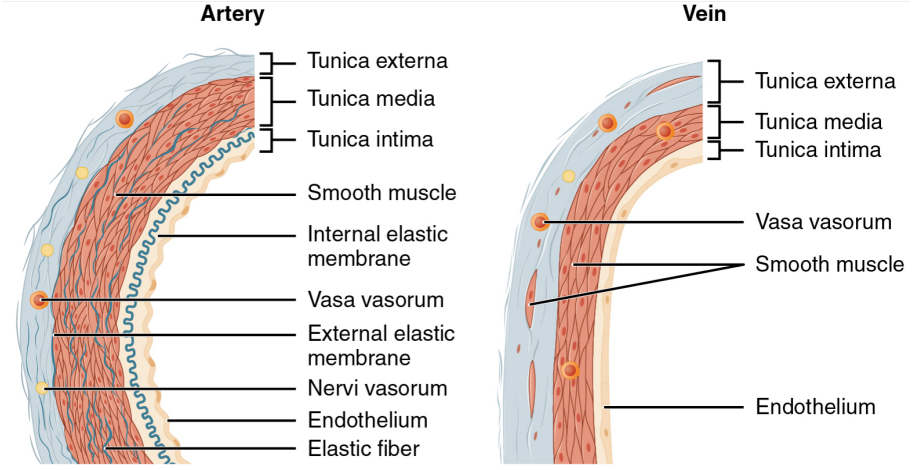


Figure 2.6: Illustrations of the vessel wall structure of artery (left) and vein (right). Adapted from OpenStax [41] under license CC BY 4.0 (https://creativecommons.org/licenses/by/4.0/).

Out of the three types of cortical vessels, arterioles have the thickest wall with a large fraction of smooth muscle cells to control blood flow with changing pressure. As the arterioles penetrate deeper into the brain and give off branches along the way, blood pressure decreases so are the arteriolar diameters and wall thicknesses. A wide range of wall thickness can be found in the literature spanning from 2 to 20 [μm] [69–72]. Capillaries, on the other hand, have very thin walls with no smooth muscle cells for the purpose of supplying nutrients to the surrounding tissue. The typical wall thickness of capillaries is between 0.3 to 1 [μm] [69, 71–73]. Venules have a thinner wall than arterioles and valves can be found in larger veins to prevent backflow due to the low blood pressure.

A special feature of the cerebral microvessels is the blood brain barrier (BBB) formed by the endothelial cells and tight junctions that seal the paracellular pathways in-between [74]. The BBB plays an important role in protecting the central nervous system (CNS) and maintaining the brain homeostasis. While oxygen and carbon dioxide can diffuse freely across the barrier, nutrients, ions and neurotransmitters are regulated by transporters in the endothelial cell membranes; the BBB also prevent

neurotoxins and most macromolecules from entering the CNS [75]. Contributing to the regulation and maintenance of the barrier are pericytes, astrocytes and microglia; together with neurons these form a neurovascular unit (Figure 2.7) [74].

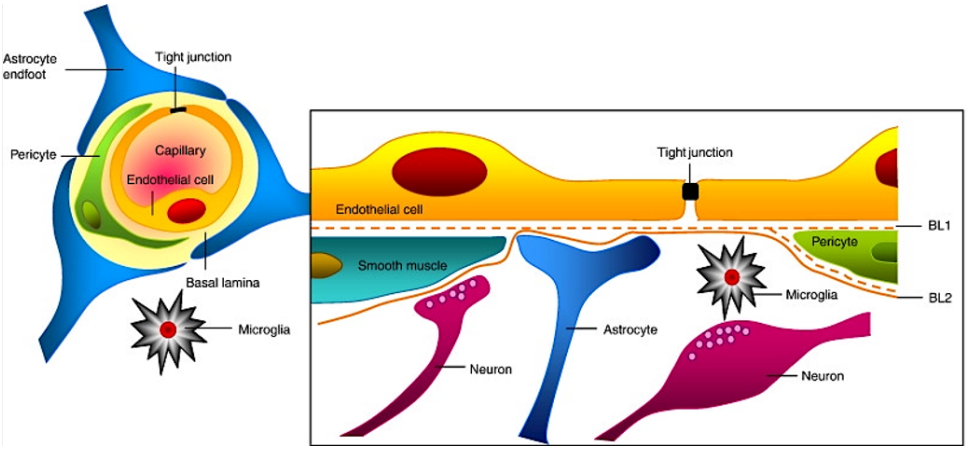


Figure 2.7: Illustration of a neurovascular unit showing the cell associations at the blood brain barrier. BL1: basal lamina; BL2: brain parenchyma. Reproduced with permission from Abbott *et al.* [75].

2.2.3 Cerebral tissue

In the CNS, there are essentially two types of brain cells: neurons and glial cells which include the aforementioned astrocytes and microglia, as well as oligodendrocytes and ependymal cells. Neurons are responsible for communication between cells throughout the body and transmitting information in the brain. Figure 2.8 (left) shows the schematic of a typical neuron; information is received at the cell body from neighbouring cells via dendrites, travels down the axon as electrical signals and is then passed to the target cells through neurotransmitters released at the synapses. The axon is wrapped in segments of myelin sheath which provides insulation and facilitates the propagation of electrical signals.

As shown in Figure 2.8, the myelin sheaths are processes extended from the cell body of the oligodendrocytes; each oligodendrocyte myelinates several axon segments, either for the same or separate axons. In addition to supporting the BBB, astrocytes also maintain the chemical concentration in the extracellular space and remove excess neurotransmitters. Microglia are smaller glial cells that ingest and

digest diseased or damaged cells. The last type of glial cell — ependymal cell — lines the ventricles and is responsible for filtering blood to produce CSF.

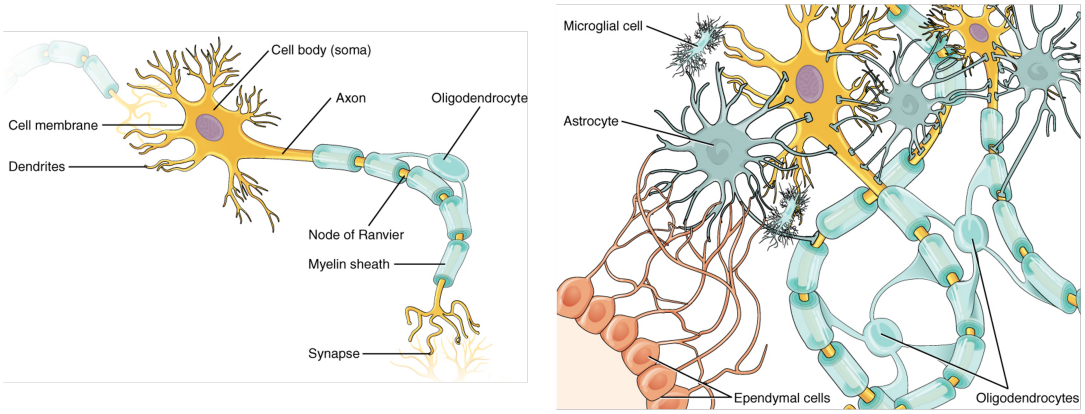


Figure 2.8: Illustration of a neuron and its components (left) and the brain tissue comprises neurons and glial cells (right). Adapted from OpenStax [41] under license CC BY 4.0 (https://creativecommons.org/licenses/by/4.0/).

While glial cells are present in both the grey matter and the white matter, the former comprises the neuron cell bodies, dendrites and the axon terminals and the latter is made of myelinated axon tracts connecting different parts of the cortex. Corpus callosum, as shown earlier in Figure 2.1, is one example of these axon bundles. Since synaptic transmission is highly energy demanding, the grey matter has a higher perfusion [76] and metabolic rate [77].

2.3 Oxygen transport and metabolism

2.3.1 Oxygen

Oxygen (O_2), being the vital nutrient for brain cells to survive, is delivered to the tissue through blood flow. The main composition of blood is erythrocytes (red blood cells) and plasma which together make up 98% of the blood volume; the other 2% is occupied by leukocytes (white blood cells) and platelets. On average, 45% of the blood volume is comprised of red blood cells (RBCs) and this fraction is known as the haematocrit.

RBCs play a very important role in transporting oxygen as only a small amount is

able to dissolve in plasma [78] which is not enough for cells to function. Almost all of the oxygen in blood is carried by haemoglobin (Hb) — a protein in the RBCs. A haemoglobin molecule has four haem groups and each can reversibly bind to one oxygen molecule forming oxyhaemoglobin; the overall percentage of oxygen-occupied haem groups is termed oxygen saturation (S_{O_2}). Haemoglobin's affinity for oxygen in a given blood environment is characterised by the oxygen dissociation curve (ODC), as shown in Figure 2.9, which describes the relationship between S_{O_2} and the partial pressure of oxygen in blood ($P^b_{O_2}$).

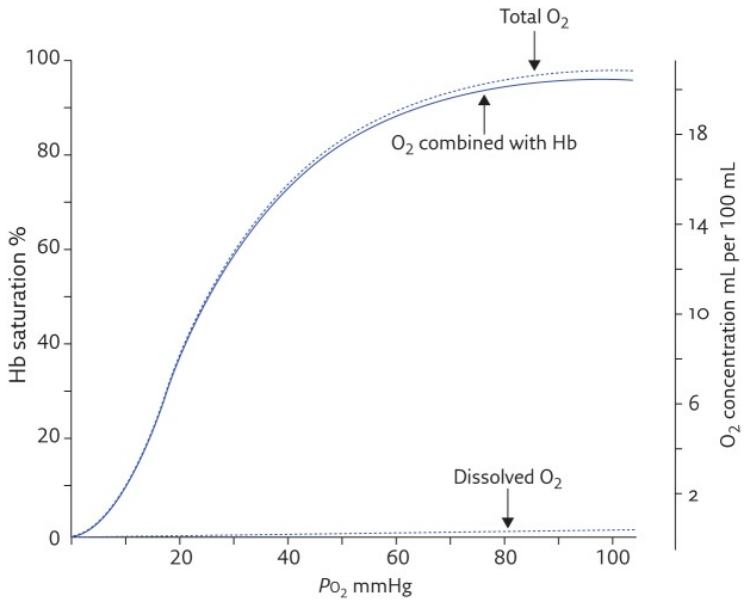


Figure 2.9: Theoretical oxygen dissociation curve illustrating the relationship between S_{O_2} (or haemoglobin saturation) and $P^b_{O_2}$ (solid line). The relationship between oxygen concentration and $P^b_{O_2}$ including the dissolved oxygen is also shown (dashed lines). Reproduced with permission of the © ERS 2024: Breathe Sep 2015, 11 (3) 194-201; DOI: 10.1183/20734735.001415 [79].

Once an O_2 is bound to a haemoglobin molecule, it facilities the subsequent binding processes [79]. This property attributes to the rapid incline of the ODC at low level of oxygenation. As all haemoglobin become fully saturated at high oxygen level, the curve flattens. Mathematically, the ODC can be approximated by the Hill equation:

$$S_{O_2} = \frac{\left(\frac{P^b_{O_2}}{P_{50}}\right)^n}{1 + \left(\frac{P^b_{O_2}}{P_{50}}\right)^n}, \tag{2.1}$$

where P_{50} is defined as the $P^b_{O_2}$ at 50% oxygen saturation with a value of 26.2 [mmHg] and n is the Hill coefficient with a value of 2.5 for normal human adults [80].

Oxygen saturation of the systemic arterial blood can be measured through blood gas analysis or a pulse oximeter. Its value is between 96% and 98% for a healthy individual [79], equivalent to about 93 to 124 [mmHg]. However, $P^b_{O_2}$ of the cortical vessels is less easy to measure and data on human are rare. The traditional method uses microelectrodes which is invasive [81,82] and the newer imaging techniques, such as the two-photon microscopy-based phosphorescence lifetime imaging ($PLIO_2$) [83], may only be used on rodents. Measurements in animal cortex suggest a $P^b_{O_2}$ of 60–100 [mmHg] in arterioles [62, 63, 83–88], 28–60 [mmHg] in capillaries [62, 83, 85, 86] and 33–50 [mmHg] in venules [62, 83, 85–88].

The relationship shown in Figure 2.9, however, is not constant. Factors affecting the position of the ODC include temperature, the local partial pressure of carbon dioxide ($P^b_{CO_2}$), pH and 2,3-BPG (a molecule that facilitates oxygen release and stabilises deoxygenated haemoglobin) [89]. The ODC is shifted to the right with a higher temperature, $P^b_{CO_2}$ and 2,3-BPG level and a lower pH [89], reducing the affinity of haemoglobin for oxygen and aiding its dissociation which is, under normal conditions in a healthy context, beneficial to metabolising tissues. As CO_2 enters the bloodstream increasing the blood's acidity, it promotes haemoglobin to release oxygen into plasma which is then ready to diffuse into the tissue.

The total oxygen content (concentration, C_b) in blood is the amount of oxygen combined with haemoglobin and that dissolved in the blood, which can be calculated as

$$C_b = B_{O_2} C_{\mathrm{Hb}} S_{O_2} + \alpha_b P^b_{O_2}, \tag{2.2}$$

where B_{O_2} is the Hüfner constant representing the oxygen binding capacity of haemoglobin, which has a theoretical value of 1.39 [mL O_2/g Hb] [90]; C_{Hb} is the haemoglobin concentration in normal blood that has a value of 0.15 [g Hb/mL blood] [79]; and α_b is the oxygen solubility in whole blood which is around $3{\times}10^{-5}$

[mL O_2/(mL blood $\cdot$ mmHg)] [91,92]. For a healthy individual, C_b is estimated to be 20 mL oxygen per 100 mL blood. The relationship between C_b and $P^b_{O_2}$ is strongly non-linear due to the ODC, which makes it very difficult to solve the governing equations and numerical methods are usually adopted.

As mentioned before, oxygen can diffuse freely across the BBB into brain cells. This process is driven by the oxygen partial pressure gradient and is often modelled by Fick's law [35] that is

$$j = \frac{\kappa}{h}(P^b_{O_2} - P^t_{O_2}), \tag{2.3}$$

where j is the oxygen flux across the vessel wall, κ represents the wall's permeability to oxygen, h is the thickness of the wall and $P^t_{O_2}$ is the oxygen partial pressure in tissue. Data on permeability of the cortical vessels are not available and values, in the range between 4.2–6.8$\times 10^{-10}$ [mL O_2/(mmHg $\cdot$ cm $\cdot$ s)] [72, 93], reported for other organs are often used.

When compared to oxygen partial pressure of cortical vessels, more data on human cerebral tissue oxygen partial pressure are available. Measurements were generally carried out in normal appearing tissues using electrode on patients undergoing craniotomy [94]. The range of $P^t_{O_2}$ was found to be 22–54 [mmHg] [95–97]. Among these studies, Dings *et al.* measured $P^t_{O_2}$ at different depth below the dura level and found that the mean $P^t_{O_2}$ decreased with brain depth [97]. Treating the cerebral tissue as a well-mixed matter, its oxygen concentration (C_t) can be assumed to be proportional to its partial pressure and follows Henry's law,

$$C_t = \alpha_t P^t_{O_2}, \tag{2.4}$$

where α_t is the solubility of oxygen in tissue and has a value of 1.97–3.95$\times 10^{-5}$ [mL O_2/(mL tissue $\cdot$ mmHg)] [93, 98, 99]. Therefore, a rough estimation of tissue oxygen concentration is about 0.1 mL oxygen per 100 mL tissue.

On the continuum level, oxygen transport can be modelled by the following advection-

diffusion-reaction equation:

$$\frac{\partial C}{\partial t} + \vec{u} \cdot \nabla C = \nabla \cdot (D \nabla C) + \mathcal{R}, \tag{2.5}$$

where t represent time, $\vec{u}$ is the velocity field, D is the diffusion coefficient and $\mathcal{R}$ is the net quantity of the substance resulting from reactions such as metabolism. In the bloodstream, diffusion is often neglected as the effect of this is small compared with advection; whereas, the opposite holds in brain tissue. A uniform and constant effective oxygen diffusion coefficient in tissue is often used with a value between 1.2–2.0×10^{-5} [cm^2/s] [93, 98]. Although it has been found that the diffusion coefficient is smaller intracellularly than extracellularly, there are no major diffusion barriers for oxygen to travel from the blood to mitochondria where it is utilised [100].

2.3.2 Metabolism

Another important nutrient for the brain is glucose (GLC, $C_6H_{12}O_6$) which is also delivered to the tissue via blood flow. Unlike oxygen, glucose gets across the BBB by facilitated diffusion. Both oxygen and glucose are utilised in the brain cells to produce adenosine triphosphate (ATP) — an organic compound that provides cells with energy to function. Figure 2.10 shows a highly simplified overview of the energy production processes which are explained below.

Firstly, glucose is converted into pyruvate (PYR, $C_3H_4O_3$) through the process of glycolysis in the cytoplasm:

$$C_6H_{12}O_6 + 2ATP + 2NAD^+ + 4ADP + 2P_i \rightarrow 2C_3H_4O_3 + 4ATP + 2NADH + 2H^+, \tag{2.6}$$

where a net of 2 moles of ATP is produced per mole of glucose; NAD^+ and NADH are the oxidised and reduced form of nicotinamide adenine dinucleotide, respectively; and ADP is adenosine diphosphate.

If oxygen and functioning mitochondria are present, pyruvate is oxidised to form

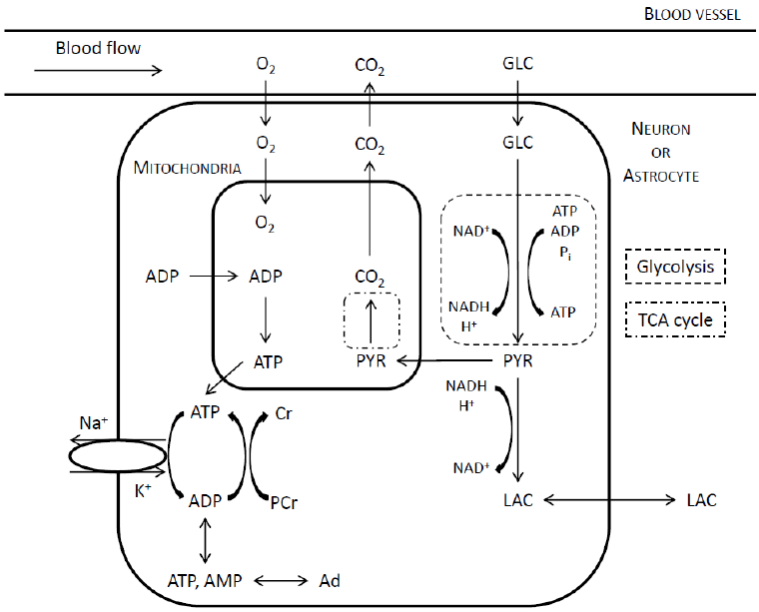


Figure 2.10: Highly simplified cellular metabolism. Reproduced with permission from *Cerebral Blood Flow and Metabolism: A Quantitative Approach*, Stephen J Payne, Copyright @ 2018, World Scientific [35].

acetyl-CoA which is then transported to the tricarboxylic acid (TCA) cycle inside the mitochondria. Reduction of NAD^+ in the TCA cycle results in the production of NADH and hydrogen ions (H^+) along with carbon dioxide (CO_2) as a waste product. NADH and H^+ are then passed through the electron transport chain reacting with oxygen which yields water (H_2O) and a large amount of ATP. The overall reaction of this aerobic metabolism can be summarised as:

$$6O_2 + C_6H_{12}O_6 + 36\text{ADP} + 36P_i \rightarrow 6CO_2 + 6H_2O + 36\text{ATP}. \tag{2.7}$$

The break down of the ATP through ATPases releases energy that supports the ion pumps along the cell's membrane and contributes to cell maintenance. In the situation of insufficient oxygen or no functioning mitochondria, pyruvate undergoes anaerobic respiration and forms lactic acid (LAC) which is also known to be an energy source for neurons [101].

There are many studies dedicated to model the cellular metabolism and the related interactive mechanisms, such as the works of Aubert and Costalat [102, 103],

Cloutier *et al.* [104] and Jolivet *et al.* [105]. Despite being valuable in understanding the metabolic processes and testing various hypotheses, these models are too complicated to be employed directly at the organ level. The model that Aubert and Costalat developed for testing the concept of astrocyte-neuron lactate shuttle comprises 20 differential equations and around 85 parameters [103]. Therefore, cerebral tissue is generally considered as a well-mixed matter and the Michaelis-Menten kinetics [106] is widely used for oxygen and glucose consumptions:

$$G = \frac{G_{\max} C_t}{C_t + C_{50}}, \tag{2.8}$$

where G is the substance uptake rate, C_t is the substance concentration in tissue, $G_{\max}$ is the maximum rate of uptake and C_{50} is the Michaelis constant defined as the substance concentration at half $G_{\max}$.

Clinically, G of oxygen is measured as the cerebral metabolic rate of oxygen ($CMRO_2$). The reference standard for measuring $CMRO_2$ is position emission tomography (PET) imaging with [^{15}O]-gas tracers inhaled continuously or in boluses. Fan *et al.* [77] performed a thorough review on the different approaches adopted by past studies and their technical considerations, and presented a meta-analysis on the results. An averaged value of 3.06 [mL O_2/(100g tissue $\cdot$ min)] was determined to be the whole brain $CMRO_2$ [77]. It is not surprising that $CMRO_2$ in the grey matter (4.45 [mL O_2/(100g tissue $\cdot$ min)]) is substantially and consistently higher than that in the white matter (1.68 [mL O_2/(100g tissue $\cdot$ min)]) [77], despite the high heterogeneity across studies.

Another important measurement is the oxygen extraction fraction (OEF) which is the ratio of oxygen consumption to delivery. It can either be determined based on cerebral blood flow (CBF) and PET parameters [107] or by evaluating the venous oxygen saturation using magnetic resonance imaging (MRI) [108]. The latter calculates OEF as

$$\text{OEF} = \frac{S^a_{O_2} - S^v_{O_2}}{S^a_{O_2}} \approx \frac{C_a - C_v}{C_a}, \tag{2.9}$$

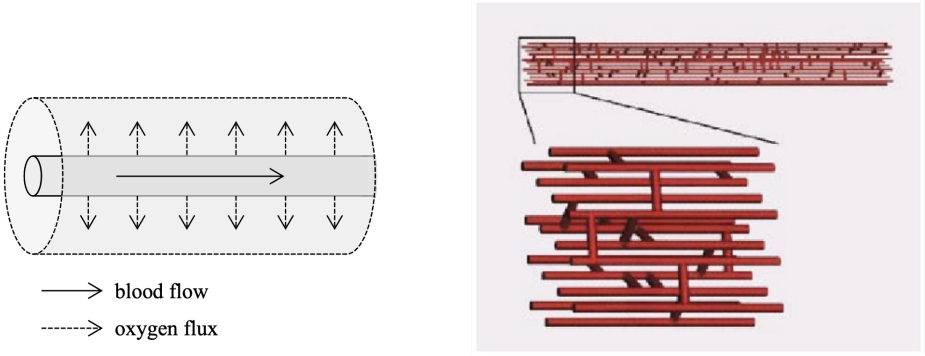
where a and v indicate arteries and veins, respectively. OEF and $CMRO_2$ are linked through CBF by the following relationship:

$$CMRO_2 = OEF \cdot CBF \cdot C_a. \tag{2.10}$$

In spite of the almost three-fold difference in oxygen consumption (and blood flow) between grey matter and white matter, OEF remains relatively uniform across a healthy brain with an averaged value of 43% in resting state [77, 109]. This emphasises the close matching between blood flow and oxygen consumption.

2.4 Theoretical models

Being the primary site for oxygen exchange, the cerebral microcirculation plays a very important role in meeting the energy requirements of the brain. Many theoretical models have been developed to gain insights into both normal physiological functions and diseases. The earliest model of oxygen transport and exchange is the Krogh cylinder [110]. Inspired by the parallel structure of muscle fibres and capillaries in the skeletal muscle, the Krogh cylinder models the capillary bed using a single cylindrical vessel that supplies oxygen to its surrounding cylinder of tissue (Figure 2.11a).



(a) (b)

Figure 2.11: Illustration of (a) Krogh model geometry and (b) parallel capillaries with interconnected vessels (from Beard and Bassingthwaighte [111]; reproduced with permission from Springer Nature).

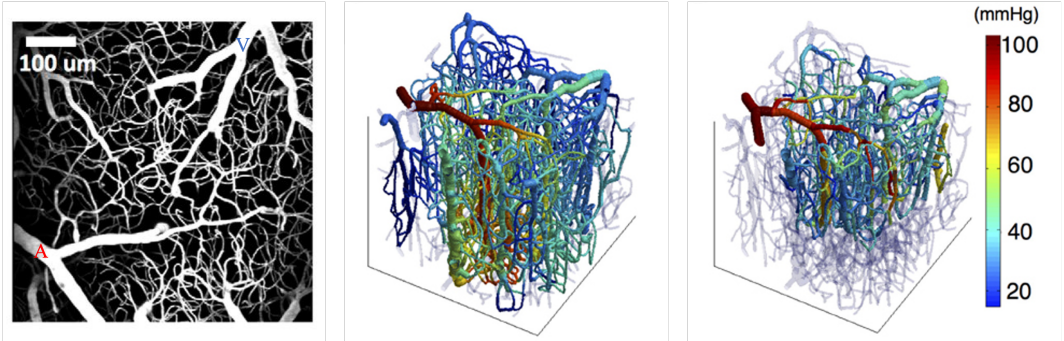
The basic Krogh model later assumed equally spaced parallel vessels each with its tissue cylinder. Several original assumptions have also been relaxed, including changing the uniform and constant oxygen consumption rate to a P_{O_2}-dependent one, often modelled by the Michaelis-Menten kinetics [112, 113]; adding time dependence to oxygen transport [114]; and taking into account the effect of axial diffusion in tissue [112, 113, 115]. Models with interconnected parallel vessels (Figure 2.11b) were also developed highlighting the influence of network geometry on oxygen delivery [111, 116, 117].

However, as shown in Section 2.2.2, the cerebral microvessels do not show a strong alignment in one direction; application of the Krogh type models in this situation would not be adequate. This has motivated the development of models with more realistic networks for analysing oxygen delivery. One of these models is by Secomb *et al.* [92, 118, 119] which considers an arbitrary vascular network in a continuum of tissue. Blood vessels are represented by a set of discrete oxygen sources and no assumption is made about the region to which a vessel supplies. Oxygen is then transported by diffusion within the tissue and the final P_{O_2} distribution is determined as the superposition of the fields resulting from each source. Results obtained from this method have shown that oxygen distribution around micro-scale blood vessels is highly heterogeneous; with the same vascular density, the Krogh type models overestimate the tissue P_{O_2} at which hypoxia occurs [119].

With the advancement of imaging techniques and computer technology, studies using microvascular networks extracted from three-dimensional (3D) angiograms started to emerge. Fang *et al.* [120] presented a general work-flow for simulating the process of oxygen advection and diffusion in a 3D anatomical microvascular network. They manually graphed a relatively small network ($230\times230\times450$ [μm^3]) extracted from two-photon scans of a rat's somatosensory cortex. This network included a pair of pial arteriole and venule with intervening capillary network. The unsteady oxygen model, comprised of 1D advection within the vessels, 1D oxygen flux across the vessel walls and 3D diffusion in the tissue, was solved using the finite element method

(FEM). The simulated arteriole P_{O_2} at a given vessel diameter agreed well with experimental data but both the capillary and venule P_{O_2} were lower due to the incomplete vascular graphs; the spatial tissue P_{O_2} was in qualitative agreement with experiment data.

To understand the relationship between microscopic vascular behaviour and macroscopic BOLD (blood oxygen level-dependent) signals, Gagnon *et al.* used rat microvascular networks ($600\times600\times660$ [μm^3]) reconstructed from angiograms (see Figure 2.12a) to simulate the vessel oxygenation at resting state and with functional activations [121]. The oxygen level was computed using the FE algorithm developed by Fang *et al.* [120] with $CMRO_2$ calculated from measured S_{O_2} and a fixed CBF. Vessel P_{O_2} distribution at rest (Figure 2.12b) was validated against *in vivo* measurements shown in Figure 2.12c. Oxygen changes during forepaw stimulations were computed by updating the blood flow and volume as well as $CMRO_2$, which compared well with experiment measurements in [88]. They then predicted the BOLD signals from first principles. Despite the fact that the microvasculature was obtained from rats, the model predicted a 40% change in the BOLD signal caused by the folds in cortex which was in good agreement with measurements in humans.



(a) (b) (c)

Figure 2.12: Reconstruction of microvascular oxygen level in rat cortex: (a) angiogram obtained by multi-photon laser scanning microscopy; (b) P_{O_2} distribution in vessels from FE simulations; (c) *in vivo* measurement of vessel P_{O_2}. Adapted with annotation from Gagnon *et al.* [121] under license CC BY 4.0 (https://creativecommons.org/licenses/by/4.0/).

As larger networks are hard to acquire through imaging and segmentation errors are prominent in microvessels, other studies have set out to computationally generate realistic microvasculatures. Linninger *et al.* used a combination of reconstruction (for penetrating vessels) and computational algorithms (for capillary bed) and generated a 3×3×3 [mm^3] subsection of the human secondary cortex [67]. Treating the tissue as a homogenous porous media, they used the network to compute axial P_{O_2} gradients and found that 20% of the total oxygen was extracted from arterioles while the majority was extracted through the capillary bed. Tissue P_{O_2} profile was heterogeneous and had a higher value around the penetrating arterioles which may explain the observation of the Pfeifer space (see Section 2.2.2) around each arteriole. Additionally, Köppl *et al.* developed a growth algorithm guided by local P_{O_2} gradients for generating vessels between segmented penetrating trees [122].

On the other hand, pure statistical models of the capillary bed [66, 68] and penetrating trees [123] that match human morphological data have also been developed (Figure 2.13). Su used such capillary networks to simulate oxygen delivery to tissue and to investigate whether a simple porous-based continuum model coupled between blood flow and oxygen was able to approximate the results of discrete networks [124]. Two pairs of source and sink were placed inside a capillary cube and after reaching steady-state, one source was removed to simulate a blockage induced ischaemic condition. The simulation was carried out on 10 different networks and the spatially-averaged tissue oxygen levels shared a similar course throughout the simulation. The continuum model was shown to capture the overall behaviour and spatially-averaged tissue oxygen level of the discrete networks when given the appropriate permeability values.

More recently, Xue *et al.* developed a oxygen model to quantify the effects of microthrombi on tissue hypoxia in statistically accurate capillary networks [30]. A selected number of vessels were randomly occluded to give a blockage fraction between 1–20% and the inlet P_{O_2} was varied between 13 and 50 [mmHg]. The simulation was performed on two sizes of periodic capillary cube with 10 different network

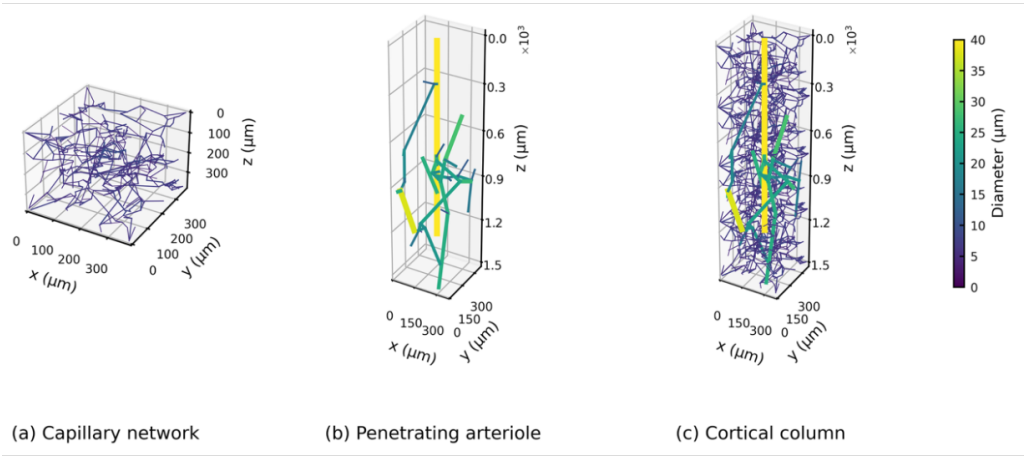


Figure 2.13: Visualisation of the statistically accurate microvascular networks: (a) a capillary network; (b) a penetration arteriole; and (c) a cortical column with four capillary cubes stacked along the length of an arteriole. Reproduced without change from Xue *et al.* [31] under license CC BY 4.0 (https://creativecommons.org/licenses/by/4.0/).

geometries each. Despite the spatial heterogeneity seen in oxygen distribution, results of average tissue P_{O_2}, hypoxic fraction (fraction of tissue with P_{O_2} below 10 [mmHg]), OEF and $CMRO_2$ showed little variation among network geometries and sizes, demonstrating that oxygen transport in capillaries is largely independent of length scale above a few hundred microns.

This model was later extended to quantify hypoxic regions in tissue as a result of arteriolar occlusions [31]. Four periodic capillary cubes were stacked vertically and coupled to a penetrating arteriolar tree forming a cortical column (Figure 2.13c). A highly heterogeneous tissue P_{O_2} distribution was observed under healthy condition which seemed to be heavily dependent on the arteriolar geometry. Two additional simulations were performed to examine the influence of network geometries on oxygen distribution; one with a different capillary network than shown in (Figure 2.13) and the other changed the arteriolar tree. It was shown that the effects of local P_{O_2} variations were negligible on the overall P_{O_2} distribution in the tissue column. Ninety one occlusion scenarios in 10 cortical column geometries were simulated and the hypoxic regions were found to be distant from the occlusion sites, which is primarily caused by the decrease in blood supply downstream. The simulation results had a good spatial agreement with the experiments reported in the same paper.

2.5 Chapter review

This chapter firstly provided an overview of the brain anatomy and the cerebral circulation with a detailed review on the microvasculature. Statistics of the microvascular morphometry that is relevant to this thesis was then summarised. Oxygen transport and metabolism were introduced next including mathematical models for their respective processes and clinical practices in measuring oxygen partial pressure and metabolic rates.

Finally, selective theoretical models of oxygen transport, representing the range of models available in the literature, were reviewed. Unlike the development of blood flow models, the majority of the current models of oxygen transport in the microcirculation focus only on the capillary bed and rely on discrete networks. There are a few lumped compartment/2D network models of oxygen transport that consider the whole microcirculation, such as the works of [32–34, 72]; however, there is no spatial variation within the compartment and the micro-scale heterogeneities are neglected.

The closest multi-scale model that came to model oxygen transport in the brain is the framework developed by Hodneland *et al.* [125], where a tracer was circulated within the bloodstream. The cerebral tissue was considered as a porous media with two fluid compartments modelling the arterial and venous sides of the capillary bed. A volumetric source term was defined to distribute blood flow around the terminals of the discrete large-vessel-network, which connected the blood flow in the 1D large vessels to that of the 3D tissue. However, this framework is not capable of stroke simulations because of the inaccurate representation of the connections between the large vessels and the tissue regions.

Nevertheless, this framework is a step forward in modelling oxygen transport within the brain. This thesis too will adopt a porous approach and the derivation of a multi-compartment, multi-scale model for oxygen transport is presented in the next chapter.

Chapter 3

Multi-compartment models

3.1 Introduction

This chapter presents the derivation of a novel continuum-based porous multi-scale, multi-compartment oxygen model that is coupled to an established blood flow model developed by Józsa *et al.* [28]. Figure 3.1 shows a schematic overview of the coupled model.

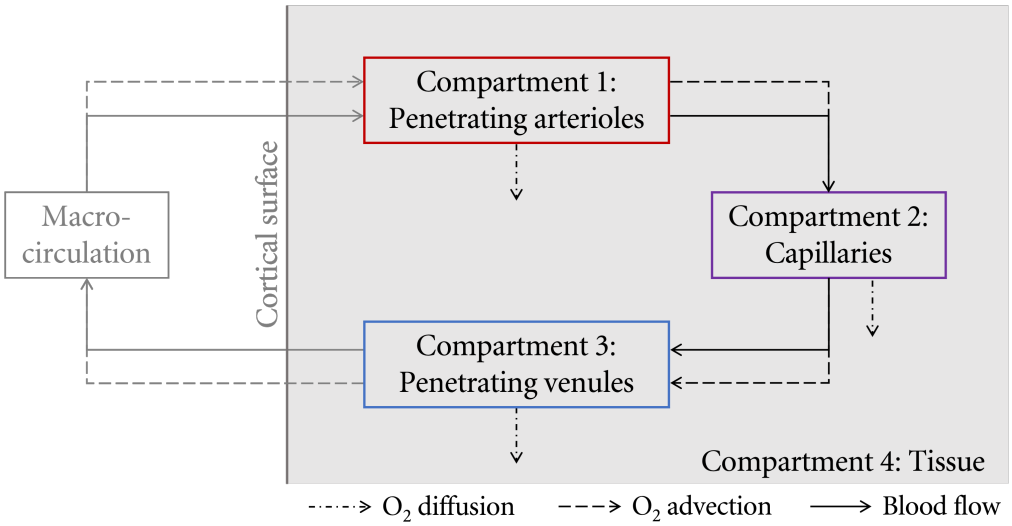


Figure 3.1: A schematic overview of the multi-compartment flow-oxygen model.

In line with the porous circulation model, the cerebral microvasculature below the cortical surface is divided into 3 discrete compartments according to their geometrical characteristics and their roles in oxygen transport. These three compartments

are the penetrating arterioles, capillaries, and penetrating venules. Additionally, a fourth compartment concerning tissue (including the interstitial space) is considered. As illustrated in the schematic diagram above, the microvascular compartments receive oxygen from the macrocirculation through bulk flow of blood. Oxygen is supplied to the tissue by the arterioles, capillaries and venules via diffusion across the vessel wall, and it is then metabolised in the tissue compartment.

3.2 Circulation model

Due to the coupled nature of the flow-oxygen model, a brief introduction of the perfusion model is firstly presented here. All the work described under this section was published in Józsa *et al.* [28]. Utilising homogenisation and Darcy's law with the assumptions that the scale between each compartment is well separated and the fluid flow is incompressible within rigid walls, the steady-state governing equations for a three-compartment porous model are

$$\nabla \cdot \left(\overline{\overline{K}}_a \nabla p_a\right) - \beta_{ac}(p_a - p_c) = 0, \tag{3.1a}$$

$$\nabla \cdot \left(\overline{\overline{K}}_c \nabla p_c\right) + \beta_{ac}(p_a - p_c) - \beta_{cv}(p_c - p_v) = 0, \tag{3.1b}$$

$$\nabla \cdot \left(\overline{\overline{K}}_v \nabla p_v\right) + \beta_{cv}(p_c - p_v) = 0. \tag{3.1c}$$

The subscripts a, c, and v represent the arteriole, capillary, and venule compartments, respectively. The unknown Darcy pressure is denoted as p [Pa]. Parameter $\overline{\overline{K}}_i$ [mm^{3}s/g] is the permeability tensor for compartment i, and β_{ij} [1/(Pa$\cdot$s)] is the coupling coefficient between compartments i and j. Additionally, the Darcy velocity $\vec{u}_i$ [mm/s] for compartment i can be calculated as

$$\vec{u}_i = -\overline{\overline{K}}_i \cdot \nabla p_i. \tag{3.2}$$

The complex microvascular structure is captured by the three 9-component permeability tensors $\overline{\overline{K}}_i$ assuming that the permeabilities are the same in grey and white

matters. It has been shown that the permeability tensor of the capillary compartment can be assumed isotropic and described by a single scalar (k_c) [28,66,68]. The penetrating arterioles and venules, on the other hand, have a strong preference on orientation; these tree-like vessels tend to penetrate the cortical surface at right angles [51]. Therefore, the permeability tensors of the penetrating vessel compartments are anisotropic and inhomogeneous [28].

To characterise the orientation preference, the penetrating tree trunks are first modelled in a reference cortical column as a 'vessel bundle' delivering blood only in the direction that is perpendicular to the pial surface [28]. By defining the z-direction as vertically inwards from the column surface, the reference permeability tensors can then be written as:

$$\overline{\overline{K}}_a^{ref} = \begin{bmatrix} 0 & 0 & 0 \\ 0 & 0 & 0 \\ 0 & 0 & k_a \end{bmatrix} \quad \text{and} \quad \overline{\overline{K}}_v^{ref} = \begin{bmatrix} 0 & 0 & 0 \\ 0 & 0 & 0 \\ 0 & 0 & k_v \end{bmatrix}. \tag{3.3}$$

The reference permeability ($\overline{\overline{K}}_i^{ref}$) is then mapped to $\overline{\overline{K}}_i$ via a local characteristic direction, $\vec{e}_{local}$. Due to the limitation of the imaging technologies, $\vec{e}_{local}$ could not directly be obtained. Instead, a computational approach that depends only on the geometry of the domain of interest is used to acquire $\vec{e}_{local}$ [28]. Figure 3.2 shows an illustration of $\vec{e}_{local}$. This transformation ensures that the patient-specific tensor $\overline{\overline{K}}_i$ only supports blood flow parallel to $\vec{e}_{local}$. Full details on the transformation process and its formulation can be found in the work of Józsa *et al.* [28] and Appendix A.

The side branches of the penetrating trees, in this model, were lumped together to represent the blood flow between compartments; therefore, their effects are accounted for by the coupling coefficients [28]. Each coupling coefficient (β_{ij}) consists of two constant values representing flow conductance in grey (β_{ij}^G) and white (β_{ij}^W) matters, and the ratio between β_{ij}^G and β_{ij}^W was assumed to be constant in [28]. Furthermore, a relationship between β_{ij}^G and the volume-averaged pressure drop across

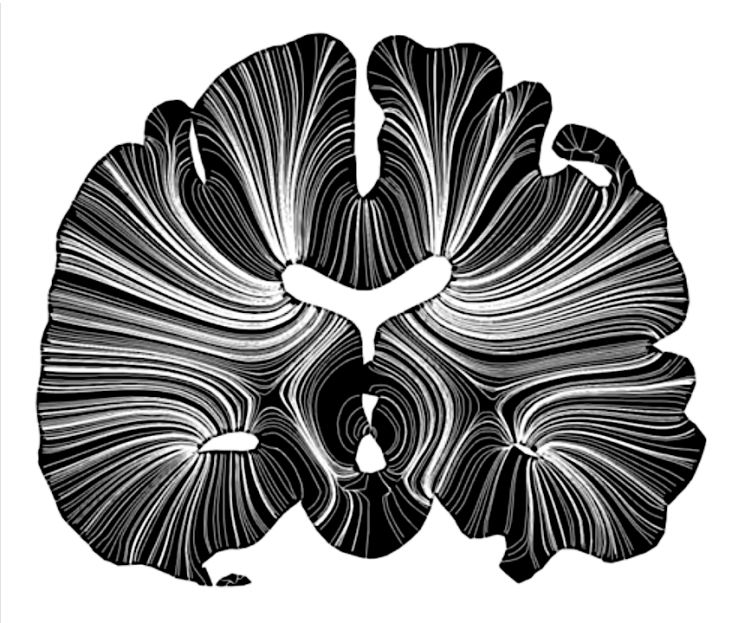


Figure 3.2: Tangent lines of $\vec{e}_{local}$ representing the local characteristic direction of the penetrating vessels. Reproduced with permission from Józsa *et al.* [28].

compartment i and j was derived, and a ratio of $\beta_{cv}^G/\beta_{ac}^G = 3.5$ [28] was determined from experimental data from the rat brain [126]. Finally, the unknown parameters k_a, k_v, β_{ij}^G and β_{ij}^W were determined through optimisation [28]. The goal of the optimisation was to obtain physiologically accurate average perfusion values for the grey and white matters; the optimised values are summarised in Table 3.1.

Permeability [$\times 10^{-3}$ mm$^3 \cdot$s/g]			Coupling coefficients [$\times 10^{-6}$ 1/(Pa$\cdot$s)]			
k_a	k_c	k_v	β_{ac}^G	β_{ac}^W	β_{cv}^G	β_{cv}^W
1.234	4.28×10^{-4} [68]	2.468	1.326	0.522	4.641	1.828

Table 3.1: Parameter values of the flow model from [28].

It is worth noting that these parameter values have high uncertainties, especially the coupling coefficients. For example, values of β_{ac}^G that can be found in the literature are 1.5×10^{-7} [1/(Pa$\cdot$s)] [127] and 1.5×10^{-19} [1/(Pa$\cdot$s)] [128, 129]. A sensitivity analysis of the parameters' influence on both perfusion and infarct volume estimations was performed in [29]. It was found that the model was least sensitive to the permeabilities and showed strong sensitivity towards the coupling coefficients which were in charge of most of the system resistance. Unfortunately, mapping and tuning

parameter values in physiological models are difficult with insufficient experimental data and high variability between patients.

3.3 Oxygen model

3.3.1 Model assumptions

Because of the complex nature of oxygen transport in the cerebral microvascular system, a number of assumptions are made here to simplify the compartmental model. Figure 3.3 gives a more detailed illustration of processes involved in the inter-compartment oxygen transport; the arrows indicate the direction of net oxygen exchange. Processes 1–3 are the movement of O_2 via advection from arterioles to capillaries, capillaries to venules, and arterioles to venules (through anastomoses/preferential channels[1]), respectively. Processes 4–7 are O_2 diffusion from arterioles directly to the close by venules via diffusion shunts (4) and from vessels to tissue (5–7). Metabolism in tissue is shown as Process 8.

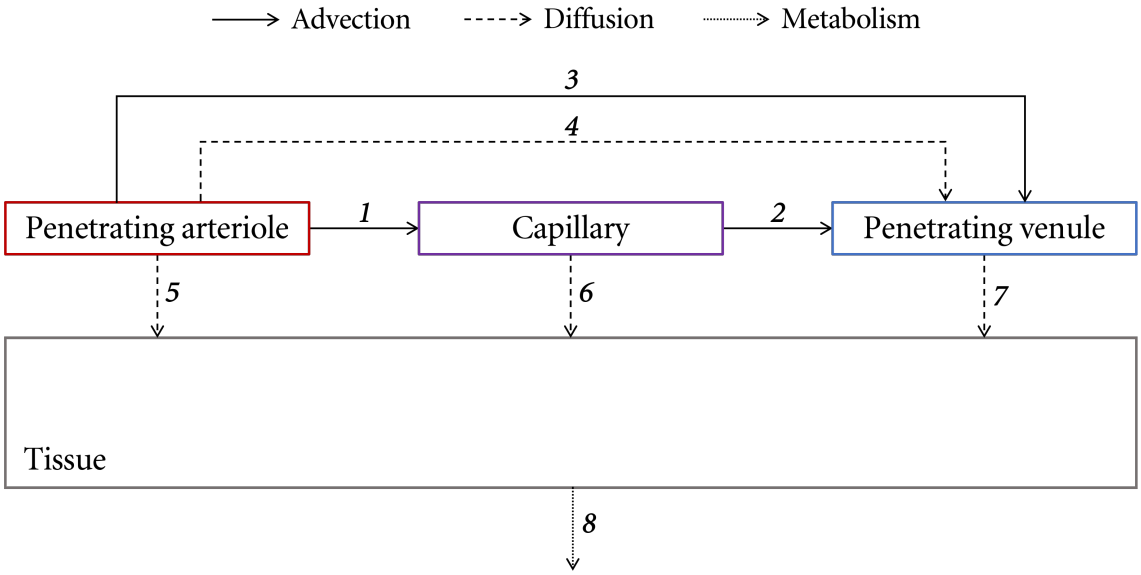


Figure 3.3: Illustration of inter-compartment oxygen transport processes.

The following assumptions are made on the system described above:

[1]The preferential channels, also called the 'thoroughfare channels', are short microvessels joining arterioles and venules at the precapillary level. Capillaries that branch off the channel have sphincters at their origin; thus, blood can bypass the capillary bed when the sphincters are closed.

Assumption 1: No direct O_2 transport from arteriolar to venular compartment. First of all, the idea of arteriovenous anastomoses and preferential channels in the cerebral microvasculature is controversial. Although Hasegawa *et al.* observed both unbranched arteriovenous anastomoses and the presence of preferential channels in human brain [130], their presence was rejected in a later work by Reina-DeLa Torre *et al.* [46]. Duvernoy *et al.* may have discovered vessels that were preferential channels, but they questioned whether these vessels could just be capillaries with a larger diameter [45]. Nonetheless, even if arteriovenous anastomoses do exits, they account for a very small fraction of the vascular branches.

The arteriovenous diffusion shunts refer to the phenomenon that oxygen leaving the arteries by diffusion enters the nearby veins. Although this phenomenon is generally accepted in the renal circulation [131], few studies have investigated its presence in the brain. Lecoq *et al.* observed an increase in P_{O_2} of a venule when crossing a nearby arteriole in rats' olfactory bulb [132]. However, this effect has not been quantified. Given that the olfactory bulb has a very low capillary content, this phenomenon may not be as prominent in other areas of the brain. Therefore, direct oxygen transport, both advective and diffusive, from arterioles to venules is not considered in the current model.

Assumption 2: No O_2 transport from venular to tissue compartment. As mentioned in Chapter 2, the diffusion of O_2 across the vessel wall commonly assumes a linear relationship between the oxygen flux (j) and the difference of the partial pressure of oxygen (P_{O_2}), i.e. Fick's law. That is

$$j = \frac{\kappa}{h}(P^b_{O_2} - P^t_{O_2}), \tag{3.4}$$

where superscript b and t represent blood and tissue, respectively, κ is the oxygen permeability of the vessel wall and h is the thickness of the vessel wall. As the P_{O_2} gradient around venules is small [133] which means $P^{\mathrm{v}}_{O_2} \simeq P^{\mathrm{t}}_{O_2}$, O_2 diffusion from venules to tissue is negligible. Therefore, Process 7 is ignored in the oxygen model

and the compartment of penetrating venules is thus essentially considered to be an oxygen sink.

Assumption 3: Blood is well-mixed and the radial concentration gradient within the vessel is negligible. As the distribution of red blood cells is not uniform along the radius of the vessel, radial gradient of oxygen is expected [134]. This gradient was also captured on imaging by two-photon P_{O_2} microscopy inside arterioles [64]. Longitudinal dispersion in vessels may become relevant if their Péclet numbers are large. From a blood flow simulation in a microvascular network [135], it was shown that most Péclet numbers are above 1 indicating that effects of Taylor's dispersion is also important in the capillaries [136]. However, Berg *et al.* [136] have shown that the radial gradient of oxygen has little effect on processes slower than 1 Hz. In other words, the well-mixed model is able to give reasonably accurate results for oxygen transport. Additionally, capturing the suspension nature of the blood using a continuum-based model is challenging and considering dispersion effects would significantly increase the complexity of the mass transport model. Many studies have employed the well-mixed assumption [67, 92, 137], and thus here we follow the same approach.

3.3.2 Model derivation

The multi-scale mass transport model is derived directly on the macro-scale based on mass conservation and the volume averaging technique [138]. Effective parameter values that properly describe the physical behaviour of the macro-scale are then identified either from literature or by using statistically accurate microvascular networks (see Chapter 4).

Considering a control volume within compartment i as illustrated in Figure 3.4, the base length of the control volume is Δx [mm] and the side surface area is A [mm^2]. An oxygen flux ($\vec{F_i}$ [mm^3 O$_2$/(mm^2 $\cdot$ s)]) enters the control volume at the left surface and leaves through the right surface. $\mathcal{S}_i$ [g O$_2$/s], representing sources/sinks, is the

rate of substance entering/leaving the control volume through inter-compartment transport and metabolism.

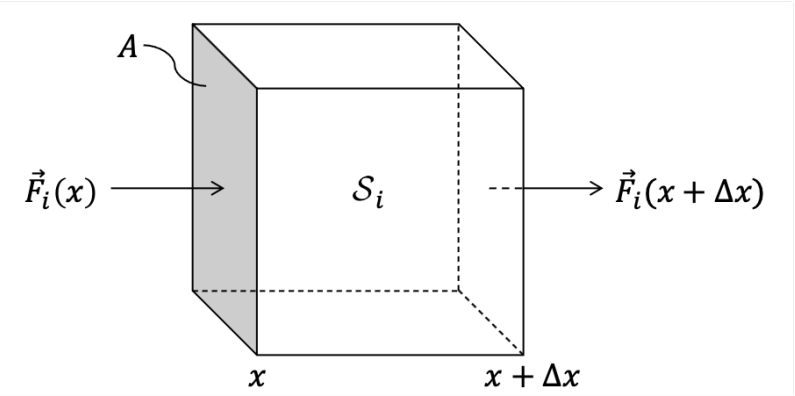


Figure 3.4: Illustration of a compartmental control volume.

Utilising conservation of mass, the following relationship exists for the control volume over a time period of Δt [s]:

$$(m_i(t+\Delta t) - m_i(t)) = \left(\vec{F}_i(x) - \vec{F}_i(x+\Delta x)\right) A\Delta t\rho_{O_2} + \mathcal{S}_i\Delta t, \tag{3.5}$$

where $m_i = C_i\Delta x A\phi_i\rho_{O_2}$ [g O_2] is the mass of oxygen for compartment i with ρ_{O_2} [g/mm^3] being the oxygen density, C_i [mm^3 O_2/mm^3 blood or tissue] being the oxygen concentration, and ϕ_i [%] being the volume fraction (porosity). We now apply Equation (3.5) to each compartment, and replace i with a, c, v and t to indicate variables that are specific to the arteriolar, capillary, venular and tissue compartment, respectively.

Arteriolar compartment

Starting with the arteriolar compartment, there is no source but there are two sinks: advection to the capillary compartment and diffusion to the tissue compartment, i.e., $\mathcal{S}_a = \mathcal{S}_a^{\text{adv}} + \mathcal{S}_a^{\text{diff}}$ (Processes 1 and 5 in Figure 3.3). Given that $p_a > p_c$, the rate of oxygen transported by advection can be expressed through the coupling term in the circulation model as

$$\mathcal{S}_a^{\text{adv}} = -\beta_{ac}(p_a - p_c)C_a\Delta x A\rho_{O_2}. \tag{3.6}$$

The mass flow rate of oxygen from arterioles to tissue via diffusion has the following form

$$\mathcal{S}_a^{\text{diff}} = -j_{at}\mathcal{A}_a\rho_{O_2} = -\frac{\kappa_a}{h_a}(P_{O_2}^a - P_{O_2}^t)\mathcal{A}_a\rho_{O_2}, \tag{3.7}$$

where j_{at} [$\text{mm}^3\,\text{O}_2/(\text{mm}^2 \cdot \text{s})$] is the oxygen flux as described by Equation (3.4); κ_a, h_a, and P_{O_2} have units of [$\text{mm}^3\,\text{O}_2/(\text{mmHg} \cdot \text{mm} \cdot \text{s})$], [mm] and [mmHg], respectively; and $\mathcal{A}_a$ [mm^2] is the total surface area of the vessel in the control volume. To relate tissue oxygen partial pressure to its concentration, Henry's law is employed giving

$$C_t = \alpha_t P_{O_2}^t \tag{3.8}$$

with α_t [$\text{mm}^3\,\text{O}_2/(\text{mm}^3$ tissue $\cdot$ mmHg)] being the solubility of oxygen in tissue. As only the oxygen dissolved in the blood (C_a^p) is free to diffuse, $P_{O_2}^a$ is linked to the total blood oxygen concentration as

$$C_a^p = \alpha_b P_{O_2}^a = \tau C_a \tag{3.9}$$

where α_b [$\text{mm}^3\,\text{O}_2/(\text{mm}^3$ blood $\cdot$ mmHg)] is the solubility of oxygen in blood, and $\tau = C_a^p/C_a$ is a constant obtained by linearising the ODC [139].

As it is highly challenging to directly obtain the total surface area of the vessels for the whole brain, the concept of a representative elementary volume (REV) [2] is employed. Statistically accurate microvascular networks are used to find the effective macro-scale parameters (see Chapter 4). As the network size increases, the microscopic parameters asymptotically tend to the converged macro values. Suppose S_a/V_a [mm^2/mm^3] is the ratio of the vessel surface area to lumen volume in the arteriolar REV, $\mathcal{A}_a$ can then be expressed as

$$\mathcal{A}_a = \frac{S_a}{V_a}\Delta x A \phi_a \tag{3.10}$$

[2]The REV is generally defined to be the smallest volume within which the macroscopic properties remain relatively constant.

with ϕ_a [%] being the volume fraction of the arteriolar lumen volume of the REV, i.e., V_a/V_{REV}. The term $\Delta x A \phi_a$ represents the total arteriolar blood volume inside the control volume.

Substituting Equations (3.6)–(3.10) into (3.5), eliminating the common variables, ρ_{O_2} and A, and dividing both sides by Δx and Δt, leads to

$$\phi_a \frac{C_a(t+\Delta t) - C_a(t)}{\Delta t} = \frac{\vec{F}_a(x) - \vec{F}_a(x+\Delta x)}{\Delta x} - \beta_{ac}(p_a - p_c)C_a - \frac{\kappa_a}{h_a}\frac{S_a}{V_a}\phi_a \left(\frac{\tau C_a}{\alpha_b} - \frac{C_t}{\alpha_t}\right). \tag{3.11}$$

Rearranging and taking the limit of Equation (3.11) as $\Delta t \to 0$ and $\Delta x \to 0$ results in

$$\phi_a \frac{\partial C_a}{\partial t} + \frac{\partial \vec{F}_a}{\partial x} = -\beta_{ac}(p_a - p_c)C_a - \frac{\kappa_a}{h_a}\frac{S_a}{V_a}\phi_a \left(\frac{\tau C_a}{\alpha_b} - \frac{C_t}{\alpha_t}\right). \tag{3.12}$$

Generalising the above one-dimensional equation provides the three-dimensional form which reads as

$$\phi_a \frac{\partial C_a}{\partial t} + \nabla \cdot \vec{F}_a = -\beta_{ac}(p_a - p_c)C_a - \frac{\kappa_a}{h_a}\frac{S_a}{V_a}\phi_a \left(\frac{\tau C_a}{\alpha_b} - \frac{C_t}{\alpha_t}\right). \tag{3.13}$$

Assuming oxygen diffusion is isotropic, the arteriolar oxygen flux is given by

$$\vec{F}_a = \vec{u}_a C_a - \phi_a D_a \nabla C_a; \tag{3.14}$$

as we chose to simplify the model by neglecting dispersion effects (Assumption 3), D_a [mm^2/s] is simply the molecular diffusion coefficient because O_2 is able to dissolve in the lipid membrane of cells eliminating the consideration of tortuosity [140]. We also assume D_a to be constant. Additionally, $\vec{u}_a$ is the Darcy velocity of the arteriolar compartment and is calculated according to Equation (3.2). This accounts for the anisotropy of the perfusion model's permeability tensor.

Substituting Equation (3.14) and rearranging the result finally gives the oxygen

transport equation for the arteriolar compartment:

$$\underbrace{\phi_a \frac{\partial C_a}{\partial t}}_{\text{I}} + \underbrace{\vec{u}_a \cdot \nabla C_a}_{\text{II}} = \underbrace{\phi_a D_a \nabla^2 C_a}_{\text{III}} - \underbrace{\beta_{ac}(p_a - p_c)C_a}_{\text{IV}} - \underbrace{\frac{\kappa_a}{h_a}\frac{S_a}{V_a}\phi_a \left(\frac{\tau C_a}{\alpha_b} - \frac{C_t}{\alpha_t}\right)}_{\text{V}}. \quad (3.15)$$

The physical significance of each term in Equation (3.15) is: I the local change of oxygen concentration; II advection within the compartment; III diffusion within the compartment; IV inter-compartment advection term; V inter-compartment diffusion term.

Capillary compartment

For the capillary compartment, there is a source and there are two sinks in $\mathcal{S}_c$: advection from the arteriolar and to the venular compartment and diffusion to the tissue compartment (Processes 1, 2 and 6 in Figure 3.3). Following the same notation as above, we have

$$\mathcal{S}_c^{\text{adv}} = \beta_{ac}(p_a - p_c)C_a \Delta x A \rho_{O_2} - \beta_{cv}(p_c - p_v)C_c \Delta x A \rho_{O_2}, \quad (3.16)$$

$$\mathcal{S}_c^{\text{diff}} = -\frac{\kappa_c}{h_c}\frac{S_c}{V_c}\Delta x A \phi_c (P_{O_2}^c - P_{O_2}^t)\rho_{O_2}. \quad (3.17)$$

As the oxygen transport equation for the capillary compartment can be derived in the same fashion as for the arteriole compartment, the steps are omitted here and the result directly follows

$$\phi_c \frac{\partial C_c}{\partial t} + \vec{u}_c \cdot \nabla C_c = \phi_c D_c \nabla^2 C_c + \beta_{ac}(p_a - p_c)C_a - \beta_{cv}(p_c - p_v)C_c - \frac{\kappa_c}{h_c}\frac{S_c}{V_c}\phi_c \left(\frac{\tau C_c}{\alpha_b} - \frac{C_t}{\alpha_t}\right). \quad (3.18)$$

Tissue compartment

In terms of the tissue compartment, its oxygen source comes from the diffusion of both arteriolar and capillary compartment (Processes 5 and 6 in Figure 3.3) and its sink is the metabolic demand of the cells (Process 8). Considering Equation (3.10),

the total surface area in the tissue compartmental control volume is

$$\mathcal{A}_t = \left(\frac{S_a}{V_t} + \frac{S_c}{V_t}\right) \Delta x A \phi_t, \tag{3.19}$$

where S_i/V_t is the ratio of vessel surface area to tissue volume in the REV of compartment $i = a, c$. Subsequently, the diffusive volumetric source term reads as

$$\mathcal{S}_t^{\text{diff}} = \left(\frac{\kappa_a}{h_a}\frac{S_a}{V_t}(P_{O_2}^a - P_{O_2}^t) + \frac{\kappa_c}{h_c}\frac{S_c}{V_t}(P_{O_2}^c - P_{O_2}^t)\right) \Delta x A \phi_t \rho_{O_2}. \tag{3.20}$$

In order to account for the physiological limitation of a positive tissue O_2 concentration, the metabolic rate of oxygen (G [$\text{mm}^3\,O_2/(\text{mm}^3\ \text{tissue}\cdot\text{s})$]) at the macro-scale is modelled by the widely-used Michaelis–Menten kinetics [106] as

$$G = \frac{G_{\max} C_t}{C_t + C_{50}}, \tag{3.21}$$

where $G_{\max}$ [$\text{mm}^3\,O_2/(\text{mm}^3\ \text{tissue}\cdot\text{s})$] is the maximum consumption rate of oxygen and C_{50} [$\text{mm}^3\,O_2/(\text{mm}^3\ \text{tissue})$] is the tissue oxygen concentration at the half maximum consumption rate. Therefore, the metabolic volumetric sink term in the tissue is

$$\mathcal{S}_t^{\text{meta}} = -\rho_{O_2} \Delta x A \phi_t \frac{G_{\max} C_t}{C_t + C_{50}}. \tag{3.22}$$

Substituting Equations (3.20) and (3.22) into (3.5), and following the same steps as for the arteriolar compartment, we have

$$\phi_t \frac{\partial C_t}{\partial t} + \nabla \cdot \vec{F}_t = \frac{\kappa_a}{h_a}\frac{S_a}{V_t}\phi_t \left(\frac{\tau C_a}{\alpha_b} - \frac{C_t}{\alpha_t}\right) + \frac{\kappa_c}{h_c}\frac{S_c}{V_t}\phi_t \left(\frac{\tau C_c}{\alpha_b} - \frac{C_t}{\alpha_t}\right) - \phi_t \frac{G_{\max} C_t}{C_t + C_{50}}. \tag{3.23}$$

It is worth noting that the following relationships exist

$$\phi_t \frac{S_a}{V_t} = \frac{V_t}{V_{REV}} \times \frac{S_a}{V_t} = \frac{S_a}{V_{REV}} = \frac{V_a}{V_{REV}} \times \frac{S_a}{V_a} = \phi_a \frac{S_a}{V_a}. \tag{3.24}$$

Similarly, $\phi_t S_c/V_t$ can be substituted with $\phi_c S_c/V_c$. Equation (3.23) then becomes

$$\phi_t \frac{\partial C_t}{\partial t} + \nabla \cdot \vec{F}_t = \frac{\kappa_a}{h_a}\frac{S_a}{V_a}\phi_a \left(\frac{\tau C_a}{\alpha_b} - \frac{C_t}{\alpha_t}\right) + \frac{\kappa_c}{h_c}\frac{S_c}{V_c}\phi_c \left(\frac{\tau C_c}{\alpha_b} - \frac{C_t}{\alpha_t}\right) - \phi_t \frac{G_{\max} C_t}{C_t + C_{50}}. \quad (3.25)$$

As the vessel surface area to volume ratio will be determined by using the statistically accurate microvasculature with best-fit lines (see Chapter 4), Equation (3.25) is chosen over Equation (3.23) to avoid numerical differences resulted from the parameter computation.

Assuming that diffusion is the only means for oxygen to travel within the tissue, the oxygen flux $\vec{F}_t$ only contains the diffusion term, i.e.

$$\vec{F}_t = -\phi_t D_t \nabla C_t. \quad (3.26)$$

Substituting $\vec{F}_t$ into Equation (3.25) leads to a diffusion-reaction equation for the tissue compartment

$$\phi_t \frac{\partial C_t}{\partial t} = \phi_t D_t \nabla^2 C_t + \frac{\kappa_a}{h_a}\frac{S_a}{V_a}\phi_a \left(\frac{\tau C_a}{\alpha_b} - \frac{C_t}{\alpha_t}\right) + \frac{\kappa_c}{h_c}\frac{S_c}{V_c}\phi_c \left(\frac{\tau C_c}{\alpha_b} - \frac{C_t}{\alpha_t}\right) - \phi_t \frac{G_{\max} C_t}{C_t + C_{50}}. \quad (3.27)$$

Gathering together Equations (3.15), (3.18) and (3.27), the 3-compartment mass transport equations for oxygen thus read

$$\cancelto{0}{\phi_a \frac{\partial C_a}{\partial t}} + \vec{u}_a \cdot \nabla C_a = \phi_a D_a \nabla^2 C_a - \beta_{ac}(p_a - p_c) C_a - \frac{\kappa_a}{h_a}\frac{S_a}{V_a}\phi_a \left(\frac{\tau C_a}{\alpha_b} - \frac{C_t}{\alpha_t}\right); \quad (3.28a)$$

$$\cancelto{0}{\phi_c \frac{\partial C_c}{\partial t}} + \vec{u}_c \cdot \nabla C_c = \phi_c D_c \nabla^2 C_c + \beta_{ac}(p_a - p_c) C_a - \beta_{cv}(p_c - p_v) C_c - \frac{\kappa_c}{h_c}\frac{S_c}{V_c}\phi_c \left(\frac{\tau C_c}{\alpha_b} - \frac{C_t}{\alpha_t}\right); \quad (3.28b)$$

$$\cancelto{0}{\phi_t \frac{\partial C_t}{\partial t}} = \phi_t D_t \nabla^2 C_t + \frac{\kappa_a}{h_a}\frac{S_a}{V_a}\phi_a \left(\frac{\tau C_a}{\alpha_b} - \frac{C_t}{\alpha_t}\right) + \frac{\kappa_c}{h_c}\frac{S_c}{V_c}\phi_c \left(\frac{\tau C_c}{\alpha_b} - \frac{C_t}{\alpha_t}\right) - \phi_t \frac{G_{\max} C_t}{C_t + C_{50}}, \quad (3.28c)$$

with the temporal terms set to zero as this thesis will be focusing on the steady

state.

3.4 Chapter review

In this chapter, an established multi-compartment perfusion model was firstly introduced laying the foundation for the development of the coupled multi-compartment flow-oxygen model. The latter was then derived directly from mass conservation on the macro-scale. In the next chapter, effective parameters of the oxygen model will be identified partly from the literature with the rest computed from statistically accurate microvascular networks.

Chapter 4

Model parameters

4.1 Introduction

In this chapter, effective values of the parameters of the coupled flow-oxygen model will be identified. In the governing equations, oxygen (O_2) concentration (C_i) within each compartment (i) is the unknown of the system. The Darcy velocity ($\vec{u}_i$), Darcy pressure (p_i) and the flow coupling coefficient (β_{ij}, $j \neq i$) are the flow-related parameters, which are acquired from the outputs of the circulation model. The rest of the parameters are oxygen-related: values of the diffusion coefficient (D_i), oxygen permeability of the vessel wall (κ_i), vessel wall thickness (h_i), oxygen solubility in blood (α_b) and in tissue (α_t), the plasma O_2 to blood O_2 ratio (τ), and the Michaelis-Menten terms ($G_{\max}$ and C_{50}) are obtained from literature and their range is summarised in Section 4.2; statistically accurate microvascular networks, on the other hand, will be used to compute the porosity (ϕ_i) and vessel surface area to blood volume ratio (S_i/V_i) and this is presented in Section 4.3.

4.2 Parameters obtained from literature

Table 4.1 summaries the values of oxygen-related parameters found in the literature. Note that C_{50} — the tissue oxygen concentration at the half maximum consumption rate — is calculated via Henry's law (Equation (3.8)). The partial pressure of

oxygen at half maximum consumption rate ($P_{C_{50}}$) has a value ranges from 0.03 to 4 [mmHg] [119, 141–143]. C_{50} is then calculated by adopting $\alpha_t = 2.6 \times 10^{-5}$ [$\mathrm{mm^3\,O_2/(mm^3\,tissue \cdot mmHg)}$] [99] and $P_{C_{50}} = 1$ [mmHg]. Additionally, value of $G_{\max}$ is assumed to be the value of measured $\mathrm{CMRO_2}$ as C_{50} is very small compared to C_t. Because of the significant difference between $\mathrm{CMRO_2}$ in the grey matter (GM) and white matter (WM), their respective $\mathrm{CMRO_2}$ values are adopted.

Parameter	Value	Unit	Reference
D_a	1.57 – 1.65	$\times 10^{-3}$ $\mathrm{mm^2/s}$	[144, 145]
D_c	1.57 – 1.65	$\times 10^{-3}$ $\mathrm{mm^2/s}$	[144, 145]
D_t	1.2 – 2.0	$\times 10^{-3}$ $\mathrm{mm^2/s}$	[93, 98, 99]
κ_a	4.2 – 6.8	$\times 10^{-8}$ $\mathrm{mm^3\,O_2/(mmHg \cdot mm \cdot s)}$	[33, 67, 72, 93]
κ_c	4.2 – 6.8	$\times 10^{-8}$ $\mathrm{mm^3\,O_2/(mmHg \cdot mm \cdot s)}$	[33, 67, 72, 93]
h_a	2 – 20	$\times 10^{-3}$ mm	[69–72]
h_c	0.3 – 1	$\times 10^{-3}$ mm	[69, 71–73]
α_b	2.86 – 3.11	$\times 10^{-5}$ $\mathrm{mm^3\,O_2/(mm^3\,blood \cdot mmHg)}$	[91, 92, 146]
α_t	1.97 – 3.95	$\times 10^{-5}$ $\mathrm{mm^3\,O_2/(mm^3\,tissue \cdot mmHg)}$	[93, 98, 99]
τ	0.008 – 0.015	-	[139]
$G_{\max}^{\mathrm{GM}}$	5.05 – 10.33	$\times 10^{-4}$ $\mathrm{mm^3\,O_2/(mm^3\,tissue \cdot s)}$	[77, 99, 147, 148]
$G_{\max}^{\mathrm{WM}}$	2.05 – 4.73	$\times 10^{-4}$ $\mathrm{mm^3\,O_2/(mm^3\,tissue \cdot s)}$	[77, 99, 147, 148]
C_{50}	0.078 – 10.4	$\times 10^{-5}$ $\mathrm{mm^3\,O_2/(mm^3\,tissue)}$	-

Table 4.1: Oxygen-related parameters values found in the literature.

4.3 Geometric parameters

As discussed in Section 3.3.2, to capture the effect of the microvascular heterogeneities on oxygen transport at the macro-scale, the concept of a representative elementary volume (REV) in numerical homogenisation [149] will be utilised for determining the effective values of the geometric parameters. As the network size increases, the microscopic parameters converge to become independent of the network size. In addition to ϕ_i ($= V_i/V_{REV}$) and S_i/V_i, two more parameters will be calculated for validation against literature values: the blood volume to vessel surface area ratio (V_i/S_i) and the vessel surface area to network (voxel) volume ratio (S_i/V_{vox}). The REV is then the volume of the smallest voxel that hosts the

converged parameters, which means at this point $V_{REV} = V_{vox}$. In the following subsections, computation of the parameters of the capillary compartment is presented first followed by those of the arteriolar compartment.

4.3.1 Capillary parameters

Parameters of the capillary compartment are determined by using the capillary beds generated by El-Bouri and Payne [68] which consists of 10 different cubical voxel sizes with their side length (L) ranging from 125 [μm] to 625 [μm]. There are 500 networks for each voxel size, which enables the characterisation of the potential variability in the microvasculature. The diameters of the capillaries are assumed to be normally distributed with values of 6.3 $\pm$ 1.3 [μm] [68]. Figure 4.1 shows an example of the statistically generated capillary networks hosted in a 375 μm cube [68]. It was found that there were not enough vessel segments in the smallest cube ($L = 125$ [μm]) to generate a continuous distribution of permeability values [68]. Therefore, it is very likely that the 125 μm voxel would also give rise to discrete distributions of the oxygen parameters. For this reason, this voxel size is omitted from the following computations.

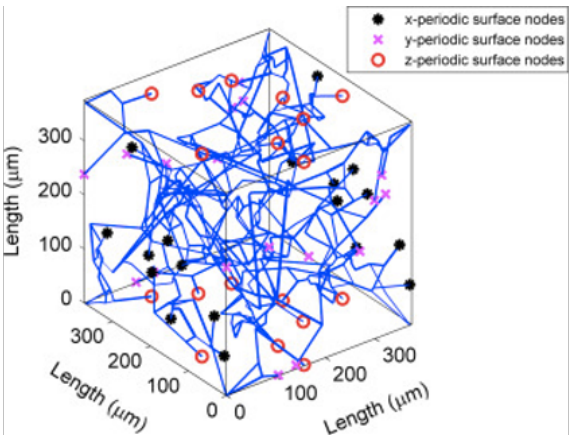


Figure 4.1: A statistically generated capillary network (voxel size: 375 [μm]). Reproduced with permission from El-Bouri and Payne [68].

Having the segment length (l) and the corresponding radius (r) of each vessel provided for each voxel, the total capillary blood volume and surface area are calculated

as

$$V_c = \sum_{i=1}^{N_s} \pi r_i^2 l_i \qquad \text{and} \qquad S_c = \sum_{i=1}^{N_s} 2\pi r_i l_i \,, \tag{4.1}$$

respectively, where N_s represents the number of vessel segments within a given voxel. The voxel volume is calculated as $V_{vox} = L^3$. Mean parameter values for each voxel size were then obtained. To characterise the statistics of each voxel size, all parameters were tested for normal distribution using the Anderson-Darling test [150] (a goodness-of-fit test using statistics based on the empirical distribution function) with a significant level of 1%. Only ϕ_c and S_c/V_{vox} for the 180 μm cube did not accept the null hypothesis, and the reason for this could still be that the number of vessel segments presented in the cubes was relatively small. Given that the other two parameters of the 180 μm cube fit the normal distribution, the values of ϕ_c and S_c/V_{vox} of this voxel size were kept. Table 4.2 summarises the mean parameter values for each voxel size and Figure 4.2 visualises the trends of the parameters as the voxel size increases.

Voxel size [μm]	ϕ_c [%]	$\frac{S_c}{V_c}\left[\frac{\text{mm}^2}{\text{mm}^3}\right]$	$\frac{V_c}{S_c}$ [μm]	$\frac{S_c}{V_{vox}}\left[\frac{\text{mm}^2}{\text{mm}^3}\right]$
180	1.55 ± 0.10	591 ± 9.65	1.69 ± 0.03	9.18 ± 0.54
250	1.57 ± 0.07	594 ± 7.38	1.69 ± 0.02	9.34 ± 0.34
300	1.38 ± 0.04	601 ± 5.71	1.67 ± 0.02	8.30 ± 0.22
375	1.43 ± 0.03	607 ± 5.01	1.65 ± 0.01	8.70 ± 0.16
425	1.41 ± 0.03	610 ± 4.04	1.64 ± 0.01	8.60 ± 0.13
450	1.44 ± 0.03	610 ± 3.98	1.64 ± 0.01	8.79 ± 0.12
500	1.41 ± 0.02	616 ± 3.28	1.62 ± 0.01	8.69 ± 0.10
550	1.45 ± 0.02	615 ± 2.77	1.63 ± 0.01	8.90 ± 0.09
625	1.42 ± 0.02	616 ± 2.25	1.62 ± 0.01	8.72 ± 0.07

Table 4.2: Mean parameter values of each voxel size.

To obtain the converged parameters, best-fit curves of the parameter means were determined. It can be observed in Figure 4.2 that, despite slower convergence rates, the parameter values converge in a similar fashion as the permeabilities computed in [68]. Therefore, the same formulation of the best-fit curve is employed and this

takes the following form:

$$\mu^c = ae^{-\frac{L}{L_{ch}}} + \mu^c_{eff}, \tag{4.2}$$

where μ^c is the mean of the parameters at every voxel size, a is a stretch coefficient, L is the voxel side length, L_{ch} is a characteristic length and μ^c_{eff} is the effective parameter. The root mean square error, $E = \sqrt{\frac{1}{N_d}\sum_{i=1}^{N_d}(ae^{-L_i/L_{ch}} + \mu^c_{eff} - \mu^c_i)^2}$ with N_d being the total number of data points, between the parameter mean and its best-fit curve was minimised and values of a, L_{ch} and μ^c_{eff} were found using the `fminsearch` function in MATLAB. The effective parameter values are shown in Table 4.3 and the best-fit curves are illustrated as blue lines in Figure 4.2.

	a	L_{ch} [μm]	μ^c_{eff}	$\%E$
ϕ_c	0.98 %	97.82	1.42 %	2.75
$\frac{S_c}{V_c}$	-67.32 $\frac{\text{mm}^2}{\text{mm}^3}$	319.52	627.31 $\frac{\text{mm}^2}{\text{mm}^3}$	0.25
$\frac{V_c}{S_c}$	0.19 μm	304.03	1.59 μm	0.25
$\frac{S_c}{V_{vox}}$	7.19 $\frac{\text{mm}^2}{\text{mm}^3}$	69.69	8.70 $\frac{\text{mm}^2}{\text{mm}^3}$	2.68

Table 4.3: Best-fit curve coefficients of the capillary parameter means.

As shown in Figures 4.2a and 4.2d, both ϕ_c and S_c/V_{vox} of the 250 μm cube and the 300 μm cube appear to deviate the most from their best-fit curves. For the 250 μm cube, the combination of having a relatively high mean segment density[1] and a large mean segment length[2] is responsible for the high mean values of ϕ_c and S_c/V_{vox}. On the other hand, both the segment density and the mean segment length of the 300 μm cube[3] are at the low end of the range, which results in smaller mean values of ϕ_c and S_c/V_{vox}. Additionally, as the 550 μm cube only has a value of mean segment density at the higher end of the range[4], the mean values of ϕ_c and S_c/V_{vox} of this

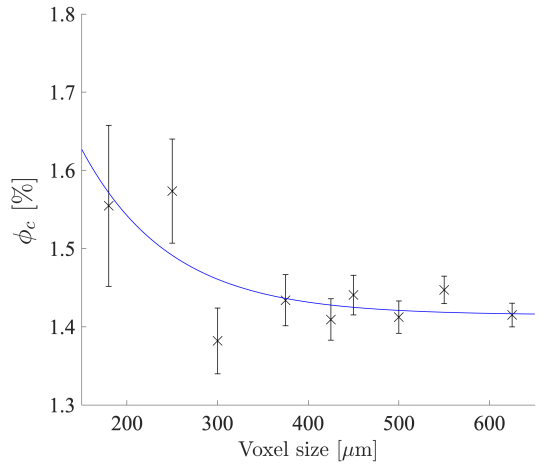
[1] 7991/mm^3 compared with a range of 7685–8272/mm^3 [68]

[2] 57.2 μm compared with a range of 53.5–57.2 μm [68]

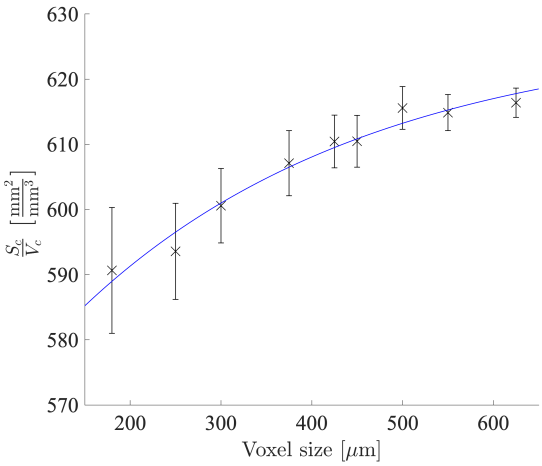
[3] For the 300 μm cube, values of the segment density and the mean segment length are 7685/mm^3 (range 7685–8272/mm^3) and 53.5 μm (range 53.5–57.2 μm), respectively [68].

[4] For the 550 μm cube, values of the segment density and the mean segment length are 8272/mm^3 (range 7685–8272/mm^3) and 54.9 μm (range 53.5–57.2 μm), respectively [68].

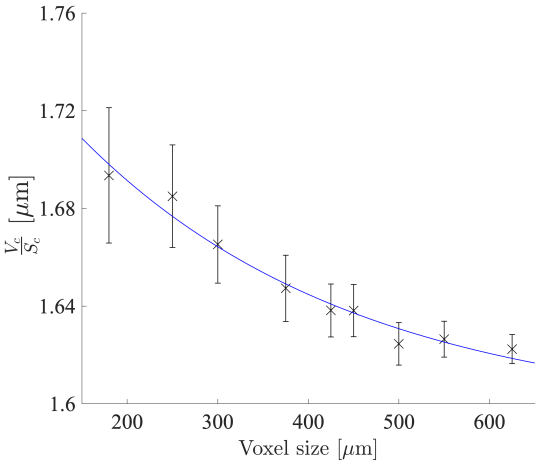
voxel size deviate slightly from the best-fit curves. Regardless of these variations, both ϕ_c and S_c/V_{vox} converged with acceptable root mean square errors. In contrast, the best-fit curves of S_c/V_c and V_c/S_c did not reach convergence despite having very small fitting errors. However, 625 [μm] remained as the upper limit of the cube size used in this work for voxel sizes larger than that are extremely computationally expensive to simulate [68]. In addition, the difference (around 1.84%) between the effective values and the means of the three largest cubes can be considered small.



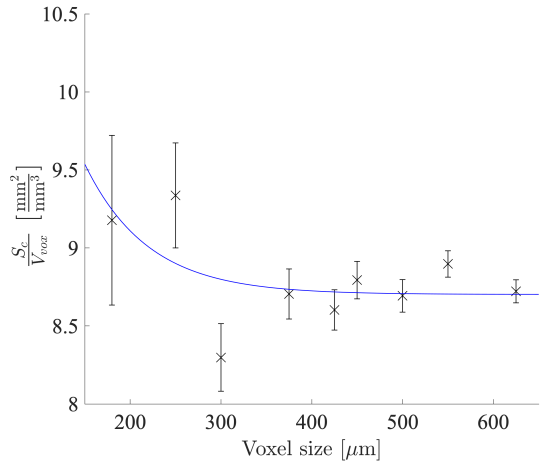
(a) Capillary blood volume fraction



(b) Vessel surface area to capillary blood volume ratio



(c) Capillary blood volume to surface area ratio



(d) Vessel surface area to voxel size ratio

Figure 4.2: Error bar plots of the capillary parameter means against voxel size and their best-fit curves (blue line).

The standard deviations (σ) of ϕ_c and S_c/V_{vox} decrease linearly with increasing voxel size when plotted on a log-log scale (Figure 4.3a). The same trend can be observed for $\sigma(S_c/V_c)$ and $\sigma(V_c/S_c)$ on a log-linear scale (Figure 4.3b). Because of

these observations, power functions of the form

$$\sigma = bL^k \tag{4.3}$$

were chosen to represent the standard deviations of ϕ_c and S_c/V_{vox}, and exponential functions of the form

$$\sigma = be^{kL} \tag{4.4}$$

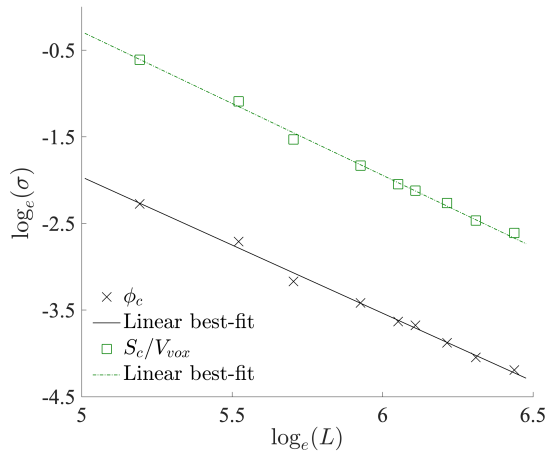
were chosen for the rest. The best-fit lines were found using the Curve Fitting Tool in MATLAB. RMSE (root mean square error) was used for evaluating the goodness of fit; the closer the value is to 0, the better the fit is. The coefficient values and the RMSEs are reported in Table 4.4 and the linear representations of the fitted lines are shown in Figures 4.3a and 4.3b.

	${\phi_c}^*$	$\frac{S_c}{V_c}^\dagger$	$\frac{V_c}{S_c}^\dagger$	$\frac{S_c}{V_{vox}}^*$
b	365.9	17.17	0.0517	2976
k	-1.573	-0.00335	-0.00361	-1.657
RMSE	0.0025	0.26	0.00077	0.010

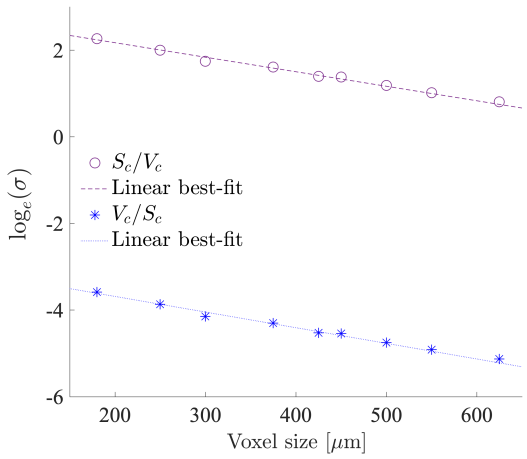
Table 4.4: Best-fit line coefficients of the standard deviation of capillary parameters. *using power fit with Equation (4.3); †using exponential fit with Equation (4.4).

Although, as mentioned earlier, ϕ_c and S_c/V_{vox} of the 180 μm cube did not fit the normal distribution, their standard deviations are in very good agreement with the fitted lines, which further justifies the inclusion of these values. Additionally, the fully characterised relationships between each parameter and the voxel size are presented in Figures 4.3c–4.3f.

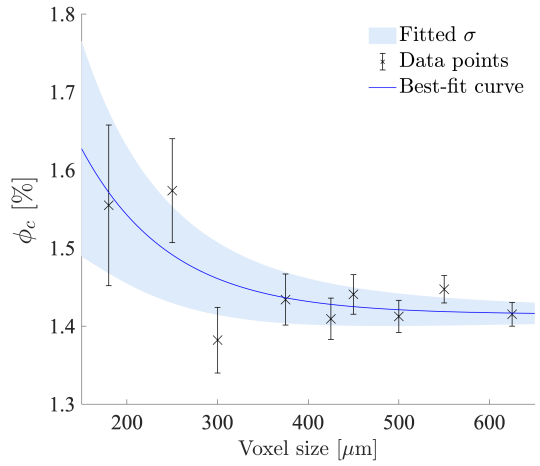
The geometric parameters extracted from statistically accurate capillary beds are now validated against the ones obtained from physiologically accurate networks (Table 4.5). Note that the values provided by Cassot *et al.* [49] and Lauwers *et al.* [51] were acquired from sections of human brain; whereas, Risser *et al.* [54] and Weber *et al.* [55] quantified these values using monkeys. Only the study by Weber *et al.* [55] provided capillary statistics for all three parameters. For the other studies, only ϕ



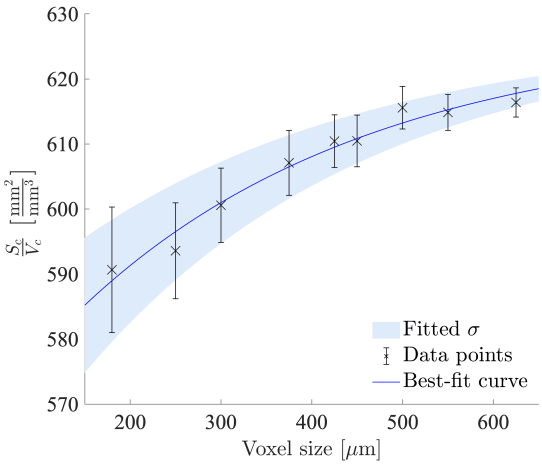
(a) Power law fit



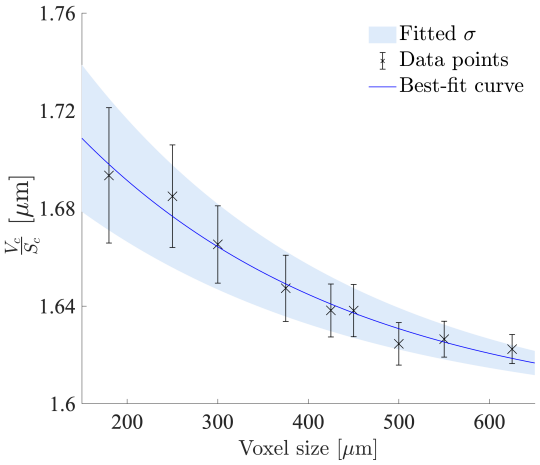
(b) Exponential fit



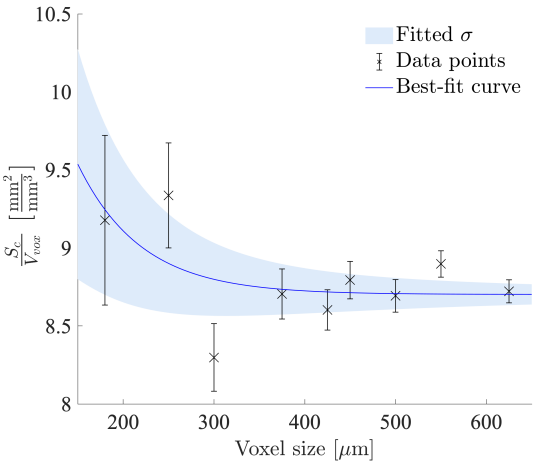
(c)



(d)



(e)



(f)

Figure 4.3: Capillary standard deviations and their best-fit lines with (a) log-log scaling and (b) log-linear scaling; best-fit curves (blue line) and fitted standard deviations (light blue shadow) of the parameters against voxel size (c–f).

was quantified for the capillary vessels alone. As shown in Table 4.5, the statistically obtained ϕ_c agrees well with most of the physiological values. Although V_c/S_c and S_c/V_{vox} are higher than the corresponding capillary-only measurements, they are within the overall range of physiological values. It is worth noting that there is a rather large variation between the values of S/V_{vox} across the literature even when the samples used are obtained from the same region [49, 51]. As the validation statistics match the literature values, the statistically obtained ϕ_c and S_c/V_c can be used with confidence.

	ϕ [%]	$\frac{V}{S}$ [μm]	$\frac{S}{V_{vox}}\left[\frac{\text{mm}^2}{\text{mm}^3}\right]$
Cassot *et al.* [49]	1.27	4.55*	5.37*
Lauwers *et al.* [51]	1.35	2.30*	11.74*
Risser *et al.* [54]	1.53	3.51*	7.87*
Weber *et al.* [55]	0.88	1.44	6.12
Capillary	1.42	1.59	8.70

Table 4.5: Comparison between the statistically computed capillary oxygen parameters and the physiological values in the literature. The cut-off diameters for capillaries are 9 [μm], 10 [μm], 11.2 [μm] and 8 [μm] for Cassot *et al.* [49], Lauwers *et al.* [51], Risser *et al.* [54] and Weber *et al.* [55], respectively. * includes non-capillaries vessels.

In addition to the REV identified base on the permeabilities of the capillary networks [68], an REV can also be decided now based on the oxygen parameters by calculating the differences between the voxel means and the effective values. Figure 4.4 shows the percentage errors of each parameter for all 9 voxel sizes. In general, the error of all parameters reduces with increased voxel size as expected. In accordance with [68], error tolerance is chosen to be 4.5% and the 375 μm cube can thus be identified as the REV for this network based on the oxygen parameters.

4.3.2 Arteriole parameters

The same method used for calculating the capillary parameters is next employed for computing the parameters in the arteriole compartment. However, unlike the capillary bed where the network was generated over a range of voxel sizes, the pen-

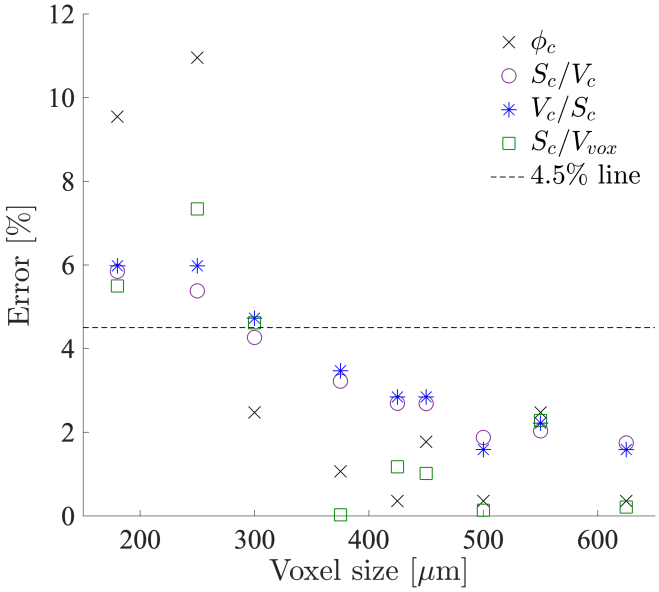


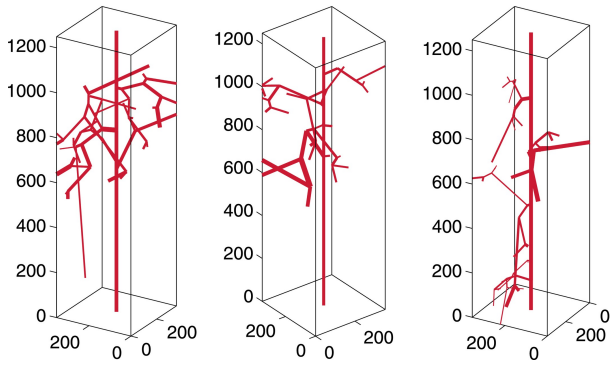
Figure 4.4: Percentage errors of the capillary voxel parameter means.

etrating arteriolar trees were generated individually with a fixed cuboid voxel size of 0.35×0.35×1.25 [mm^3] [123] (Figure 4.5a). In order to find the effective arteriolar parameters, larger voxel sizes were achieved by assembling randomly selected individual trees. This process is shown in Figures 4.5b–4.5d for voxels (tree units) containing two to four trees. Note that the same tree is repeated in the figure here purely for illustrative purpose. The smallest tree unit chosen contains two penetrating arteriolar trees and the largest one contains 80 trees; for any given tree unit, 500 unique combinations were generated.

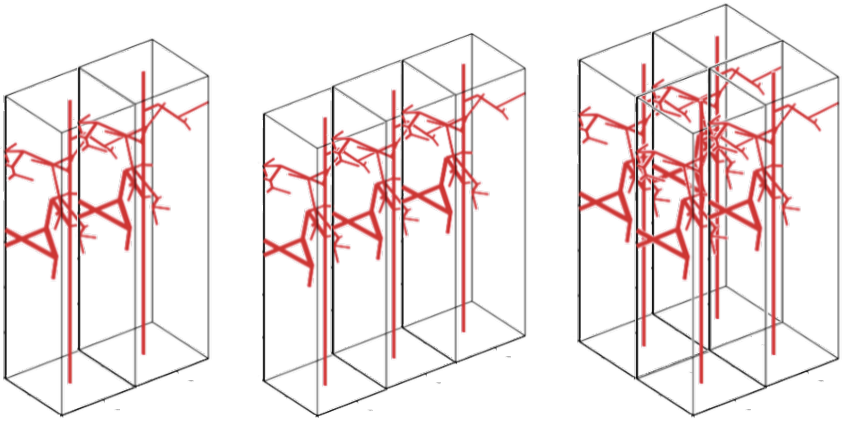
The diameters of the arterioles have a very wide range, most of which are between 15 to 40 [μm] with larger vessels reaching a value of 240 [μm] [45]. As the volume fraction has the most consistent value across the literature and it is the only value that has been reported separately for capillaries and large vessels[5], it is used to determine the desired arteriolar main trunk diameter and its potential variations.

As a starting point, previously simulated arteriolar models were firstly used as test cases to compute the oxygen parameters. This set of arteriolar trees was generated

[5] Large vessels include both the penetrating arterioles and venules. The blood volume ratio between these two type of vessels is still an area of open research; a value of ∼1 was estimated by Barrett *et al.* [59]



(a) Individual trees



(b) Two-tree unit (c) Three-tree unit (d) Four-tree unit

Figure 4.5: Examples of randomly generated morphologically accurate individual arteriolar trees (a) and larger voxels formed by individual trees (b–d). Adapted with permission from El-Bouri and Payne [123] © 2016 John Wiley & Sons, Ltd.

by El-Bouri and Payne using an order-based density-filling algorithm [123], which contains 3000 individual arteriolar trees divided equally for two trunk diameters — 25 ± 0 [μm] and 40 ± 0 [μm]. The effective values of $\phi_a(25\mu\text{m})$ and $\phi_a(40\mu\text{m})$ calculated according to the process above are 1.50% and 6.40%, respectively. This means that the sum (ϕ) of the effective volume fraction of the capillaries (ϕ_c) and the arterioles (ϕ_a) alone are 2.92% for $\phi(25\mu\text{m})$ and 7.82% for $\phi(40\mu\text{m})$. However, the physiological value of the total volume fraction[6] has an average value of 2.63% with the highest value reaching 4.30% [49, 51, 54]. The large volume fraction associated with the 40 μm trees can be explained by the fixed voxel volume of individual trees. As the trunk diameter increases, an arteriolar tree is expected to feed a larger tissue volume; however, the 40 μm trees here share the same total volume as the 25 μm

[6] The total volume fraction reported in the literature includes both the capillaries and the large vessels.

trees.

Assuming that the blood volume ratio of the arterioles and venules is 1 [59], the overall effective volume fraction calculated with the 25 μm trees (4.42%) is slightly over the physiological range. More importantly, with no variation in the trunk diameter, the current set of penetrating arteriolar trees fails to accommodate the wide range of arteriole vessel size. To address these shortcomings, new arteriolar trees were generated using the same data-driven algorithm [123]. In order to reduce the unrealistic volume fractions associated with larger trunk diameters, the voxel volume of each tree was adjusted according to a reference combination. As the 25 μm penetrating tree achieved a reasonable volume fraction with a individual voxel size of 0.35×0.35×1.25 [mm^3], this combination was used as the scaling standard.

Now, let s_0, L_0 and r_0 (s_a, L_a and r_a) be the voxel width, voxel/trunk length and the trunk radius of the reference (scaled) combination. Three linear scaling criteria are explored here due to the lack of quantitative information on such relationships and for simplicity. These criteria are listed below:

1. the voxel volume changes linearly with the **radius** of the trunk vessel;
2. the voxel volume changes linearly with the **surface area** of the trunk vessel;
3. the voxel volume changes linearly with the **volume flow rate** of the trunk vessel.

Although these criteria are linear, they could be thought of as first, second and third power scalings, respectively. Additionally, there are two cases for each criterion with the assumptions that the new vessel length either remains the same as the reference length, i.e., $L_a = L_0$ or it changes linearly with the vessel radius, i.e., $L_a = L_0 r_a / r_0$. Taking criterion 1 as an example, we have the following relationship between the reference voxel volume (V_0) and the trunk radius

$$V_0 = s_0^2 L_0 = f_1 r_0, \tag{4.5}$$

where s_0^2 is the voxel base area and f_1 is the scaling factor for criterion 1. Rearranging Equation (4.5), we can express f_1 in terms of the reference variables as

$$f_1 = \frac{s_0^2 L_0}{r_0}. \tag{4.6}$$

Then the scaled voxel volume (V_{vox}^s) can be related to the reference variables through the scaling factor as

$$V_{vox}^s = s_a^2 L_a = f_1 r_a = s_0^2 L_0 \frac{r_a}{r_0}. \tag{4.7}$$

When $L_a = L_0$, the base area of the scaled voxel becomes $s_a^2 = s_0^2 r_a / r_0$ (Case 1); when $L_a = L_0 r_a / r_0$, the base area of the scaled voxel stays the same as the reference area, i.e., $s_a^2 = s_0^2$ (Case 2). These two cases give different statistics for the arteriolar trees because the number of branches along an arteriolar trunk depends on its length.

Moving on to criterion 2, the scaling factor and the scaled voxel volume of this criterion are

$$f_2 = \frac{s_0^2 L_0}{2\pi r_0} \qquad \text{and} \qquad V_{vox}^s = s_0^2 L_a \frac{r_a}{r_0}, \tag{4.8}$$

respectively. For $L_a = L_0$, the scaled voxel volume returns to the same expression as Equation (4.7), which means that this scaling reaches the exact same result as in Case 1. With $L_a = L_0 r_a / r_0$, the scaled voxel volume becomes $V_{vox}^s = s_0^2 L_0 r_a^2 / r_0^2$ and the scaled base area is $s_a^2 = s_0^2 r_a / r_0$ (Case 3). Regarding the last criterion, the scaling factor is calculated as

$$f_3 = \frac{s_0^2 L_0}{Q_0} = \frac{8\,\eta\, L_0^2\, s_0^2}{\pi\, \Delta p_0\, r_0^4}, \tag{4.9}$$

where Q_0 is the volume flow rate inside the reference trunk vessel, η is blood viscosity and Δp_0 is the pressure drop between the two ends of the trunk vessel. Although the Fåhræus–Lindqvist effect [151] is present in the arterioles, the blood flow is assumed to follow the Hagen-Poiseuille equation for simplicity. This allows η to be eliminated

from the scaled voxel volume, which can be found from

$$V_{vox}^{s} = s_0^2 \frac{\Delta p_a \, r_a^4 \, L_0^2}{\Delta p_0 \, r_0^4 \, L_a}. \tag{4.10}$$

An additional assumption is made here regarding Δp_a; as the variation in trunk length is in the order of micrometers, the change in pressure due to length change is negligible, i.e., $\Delta p_a = \Delta p_0$. Therefore, substituting L_0 or $L_0 r_a / r_0$ as L_a in Equation (4.10) leads to two further cases (Case 4 or 5). Table 4.6 summarises the simplified expressions of the scaled voxel volume, trunk vessel length and the voxel base area.

Case	1	2	3	4	5
V_{vox}^{s} [mm^3]	$s_0^2 \, L_0 \, \frac{r_a}{r_0}$	$s_0^2 \, L_0 \, \frac{r_a}{r_0}$	$s_0^2 \, L_0 \, \frac{r_a^2}{r_0^2}$	$s_0^2 \, L_0 \, \frac{r_a^4}{r_0^4}$	$s_0^2 \, L_0 \, \frac{r_a^3}{r_0^3}$
L_a [mm]	L_0	$L_0 \, \frac{r_a}{r_0}$	$L_0 \, \frac{r_a}{r_0}$	L_0	$L_0 \, \frac{r_a}{r_0}$
s_a^2 [mm^2]	$s_0^2 \, \frac{r_a}{r_0}$	s_0^2	$s_0^2 \, \frac{r_a}{r_0}$	$s_0^2 \, \frac{r_a^4}{r_0^4}$	$s_0^2 \, \frac{r_a^2}{r_0^2}$

Table 4.6: Simplified expression of the scaled voxel volume (V_{vox}^{s}), trunk vessel length (L_a) and the voxel base area (s_a^2).

To include variation in the trunk diameter, standard deviations of 5 [μm] and 10 [μm] were introduced to a mean diameter of 25 [μm]. This choice was made because it would cover the range of arteriole diameters that has the highest occurrence (15–40 [μm] [45]). 1250 arteriolar trees were generated for each case and the segment densities of all cases were found to be within 1% of the physiological mean [123]. The total arteriolar blood volume (V_a) and the surface area (S_a) of each individual voxel are calculated in the same way as that of capillaries according to Equation (4.1), and the voxel volume of each tree is calculated using V_{vox}^{s} in Table 4.6 depending on the case it belongs to. For a tree unit, the value of its V_a, S_a and unit voxel volume V_{vox} are simply the sum of the corresponding values of the individual trees in that unit. The converged volume fraction of each case was obtained by finding

the best-fit curve of the means. Similar to Equation (4.2), the following form of the best-fit curve is employed:

$$\mu^a = ae^{-\frac{V_{vox}}{V_{ch}}} + \mu^a_{eff}, \tag{4.11}$$

where μ^a is the arteriolar parameters' mean at each V_{vox}, a is the stretch coefficient, V_{ch} represents the characteristic volume and μ^a_{eff} is the effective parameter value. MATLAB's Curve Fitting Tool was used to determine the coefficients of Equation (4.11).

The effective volume fractions of the 25 ± 5 μm models are approximately 2% and that of the 25 ± 10 μm models are around 3% (Table 4.7). Upon a closer examination, the maximum volume fraction of an individual 25 ± 5 μm tree is around 36% for all 5 cases except for that of Case 4 which is 17.61%. The maximum volume fraction of an individual 25 ± 10 μm tree ranges from 35.53 to 95.96%. Additionally, there are about 0.8% of the trees that have a value of $\phi_a > 10\,\%$ in the 25 ± 5 μm models, and about 7% in the 25 ± 10 μm models apart from Case 4 (11.28%). To eliminate the effect of these unrealistically dense trees on the calculation of effective parameters, only individual trees with a value of ϕ_a within two standard deviations of the mean are used to compute the modified ϕ_a. This resulted in an averaged reduction of 13% on the effective values of all cases (Table 4.7).

Case	25 ± 5 μm		25 ± 10 μm	
	ϕ_a [%]	modified ϕ_a [%]	ϕ_a [%]	modified ϕ_a [%]
1	2.08	1.76	2.79	2.33
2	2.12	1.83	2.98	2.55
3	2.23	1.96	3.34	2.76
4	1.92	1.75	2.71	2.60
5	2.17	1.93	3.30	2.81

Table 4.7: Effective volume fraction of all 5 cases for both the 25 ± 5 μm model and the 25 ± 10 μm model.

It can be seen from Table 4.7 that the smallest arteriolar volume faction obtained by the aforementioned methods is 1.75%, which is larger than the value of ϕ_a obtained from the test case by 0.2% and would still take the total volume fraction over the

physiological range. The main reason for this is that the generation algorithm is density-filling, which means that it is developed to match the morphological segment density instead of volume fraction. With an increase in voxel volume for increased trunk diameter, there were more vessel segments generated to fulfil the segment density requirement. It was also found that a reduction in density (number of vessel segments) did not necessarily lead to a decrease in the modified volume fraction (Table 4.8), as the latter changes with the segment length and has a square dependence on the radius of the vessels. However, as penetrating venules are considered as sinks in the multi-compartment oxygen model, the arteriolar volume fraction can be considered as an overall representation of the large-vessel volume fraction. Consequently, the total volume fraction of the microvasculature computed with any of the modified values listed in Table 4.7 is smaller than the largest physiological value reported in the literature. Therefore, these newly generated trees are employed here to compute the arteriolar oxygen parameters.

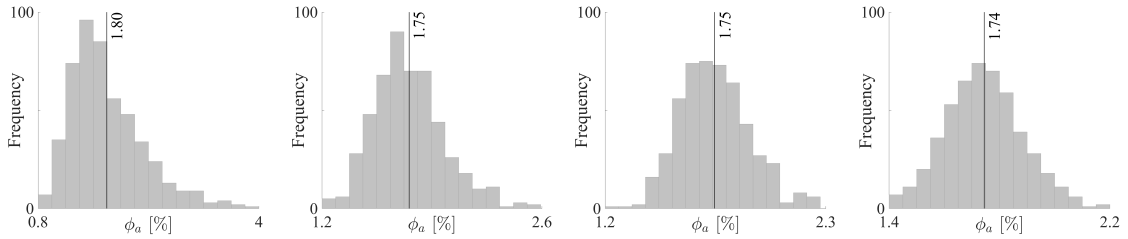
Case	Segment density [/mm^3]	ϕ_a [%]	Modified ϕ_a [%]
1	373.14	2.07	1.78
1	385.44	2.08	1.76
4	377.49	1.91	1.73
4	383.73	1.92	1.75

Table 4.8: Values of the segment density, original volume fraction and modified volume fraction obtained by the 25 $\pm$ 5 μm model for Case 1 and 4.

Similar to the characterisation of the capillary parameters, all arteriolar parameters underwent the Anderson-Darling test [150] for normal distribution with a significant level of 1%. Although the overall volume fraction computed with Case 4 (3.17%) is the closest to the physiological mean (2.63%), one of the parameters obtained from this case (V_a/S_a) rejected the null hypothesis, i.e., $p < 0.01$[7]. Unlike the capillary network which has only two parameters of the smallest voxel size not fitting the normal distribution, distribution of the arteriolar parameters was slightly skewed at smaller voxels and gradually became normal as the voxel size increases. For

[7] The p-value is the probability of observing a test statistic as extreme as, or more extreme than, the observed value under the null hypothesis.

example, Figure 4.6 shows the distribution of ϕ_a of selected tree units from Case 4. As the voxel size increases, the p-value of the distribution increases indicating a trend towards normal distribution, which firstly passes the 1% significant level with 62-tree units ($p = 0.03$). However, V_a/S_a of Case 4 did not reach the 1% significant level within the simulated voxel sizes.



(a) 5-tree unit, p =N/A (b) 30-tree unit, p =N/A (c) 50-tree unit, $p = 0.0016$ (d) 80-tree unit, $p = 0.23$

Figure 4.6: ϕ_a distribution of selected tree units from Case 4.

Consequently, Case 1, which is the second best choice by a 0.01% difference, is selected here to characterise the oxygen parameters of the penetrating arteriolar trees. All four parameters can be represented by the normal distribution within each voxel size for at least 34% of all voxel sizes. Best-fit curves for each parameter were found using Equation (4.11) and the coefficient values are presented in Table 4.9. Note that due to the very small variation in S_a/V_{vox} with respect to voxel size (see Figure 4.7d), an immediate convergence can be assumed and the mean of all voxel sizes was thus taken to be the effective value.

	a	V_{ch} [mm^3]	μ^a_{eff}	RMSE
ϕ_a	-0.033 %	0.88	1.76 %	0.0026
$\frac{S_a}{V_a}$	16.8 $\frac{\text{mm}^2}{\text{mm}^3}$	0.91	191.7 $\frac{\text{mm}^2}{\text{mm}^3}$	0.39
$\frac{V_a}{S_a}$	-0.24 μm	0.96	5.23 μm	0.0058
$\frac{S_a}{V_{vox}}$	-	-	3.36 $\frac{\text{mm}^2}{\text{mm}^3}$	-

Table 4.9: Best-fit curve coefficients of the arteriolar parameter means.

The best-fit curves are shown as blue lines in Figures 4.7a–4.7d with a reduced

number of data points for a better visualisation. The standard deviations of all parameters reduce linearly as the voxel size increases on a log-log scale (Figure 4.7e); therefore, Equation (4.3) is used to fit the standard deviation data. Again, the coefficients of Equation (4.3) were found using MATLAB's Curve Fitting Tool and their values are recorded in Table 4.10. The fitted standard deviation of each parameter is illustrated as light blue shade in Figures 4.7a–4.7d, and the linear representations of the best-fit lines are plotted in Figure 4.7e. It can be observed that there are no outliers in the standard deviation fitting despite the fact that parameters obtained from some of the smaller tree units cannot be characterised by normal distributions with a significance level of 1%.

	ϕ_a	$\frac{S_a}{V_a}$	$\frac{V_a}{S_a}$	$\frac{S_a}{V_{vox}}$
b	0.3897	21.27	0.5790	0.4433
k	-0.5090	-0.4732	-0.4760	-0.5077
RMSE	0.0060	0.44	0.010	0.0068

Table 4.10: Best-fit line coefficients of the standard deviation of arteriolar parameters.

Oxygen parameters of the microvasculature, including both arterioles and capillaries, are computed and then compared with the physiological data from the literature (Table 4.11). Although both the overall values of ϕ and S/V_{vox} are higher than the reported means, they are below their respective upper bounds (4.30% and 12.85 [mm^2/mm^3]) from [54]. With the value of V/S falling within the morphological range, the result of the overall parameter values also validates the capillary parameter findings. Now, with both ϕ_a and S_a/V_a determined, the only unknown parameter in the governing equations is the volume fraction of tissue (ϕ_t). As the venules are considered to be sinks, tissue is assumed to be the sole occupant of the remaining volume, which gives $\phi_t = 96.82\%$.

Finally, the REV of the arteriolar trees was found by calculating the errors between the effective values and the means of each tree unit. A truncated error versus voxel size (up to 7 [mm^3] for better visualisation) plot is shown in Figure 4.7f; all variables

	ϕ [%]	$\frac{V}{S}$ [μm]	$\frac{S}{V_{vox}}\left[\frac{\text{mm}^2}{\text{mm}^3}\right]$
Cassot *et al.* [49]	2.44	4.55	5.37
Lauwers *et al.* [51]	2.70	2.30	11.74
Risser *et al.* [54]	2.75	3.51	7.87
Weber *et al.* [55]	2.14	1.95	10.97
Arteriole	1.76	5.23	3.36
Overall	3.18	2.63	12.06

Table 4.11: Comparison between the statistically computed oxygen parameters and the physiological values in the literature.

converged rapidly with respect to voxel size. By adopting the same 4.5% tolerance, an REV of 0.61 [mm^3] (3 tree units) is obtained for the penetrating arteriolar trees. The arteriolar REV is slightly over ten times more than the previously found capillary REV (0.052 [mm^3]), but still smaller than the volume of a typical imaging voxel (1–5 [mm^3]).

4.4 Chapter review

Following the development of the coupled flow-oxygen model in the previous chapter, this chapter identified the effective values of the parameters that are required in the governing equations. The majority of the oxygen-related parameters were found in the literature and are summarised in Section 4.2. The geometric parameters including the volume fraction and the vessel surface area to volume ratio were calculated using statistically accurate microvascular networks. The values of these parameters as well as the REV for both the capillary network and arteriolar trees are listed for ease of access in Table 4.12. The coupled flow-oxygen model will be implemented using the finite element method in the next chapter.

Compartment	ϕ [%]	$\frac{S}{V}\left[\frac{\text{mm}^2}{\text{mm}^3}\right]$	REV [mm^3]
Capillary	1.42	627.31	0.052
Arteriole	1.76	191.70	0.61

Table 4.12: Values of the geometric oxygen parameters and the REV computed based on the statistically accurate microvasculature.

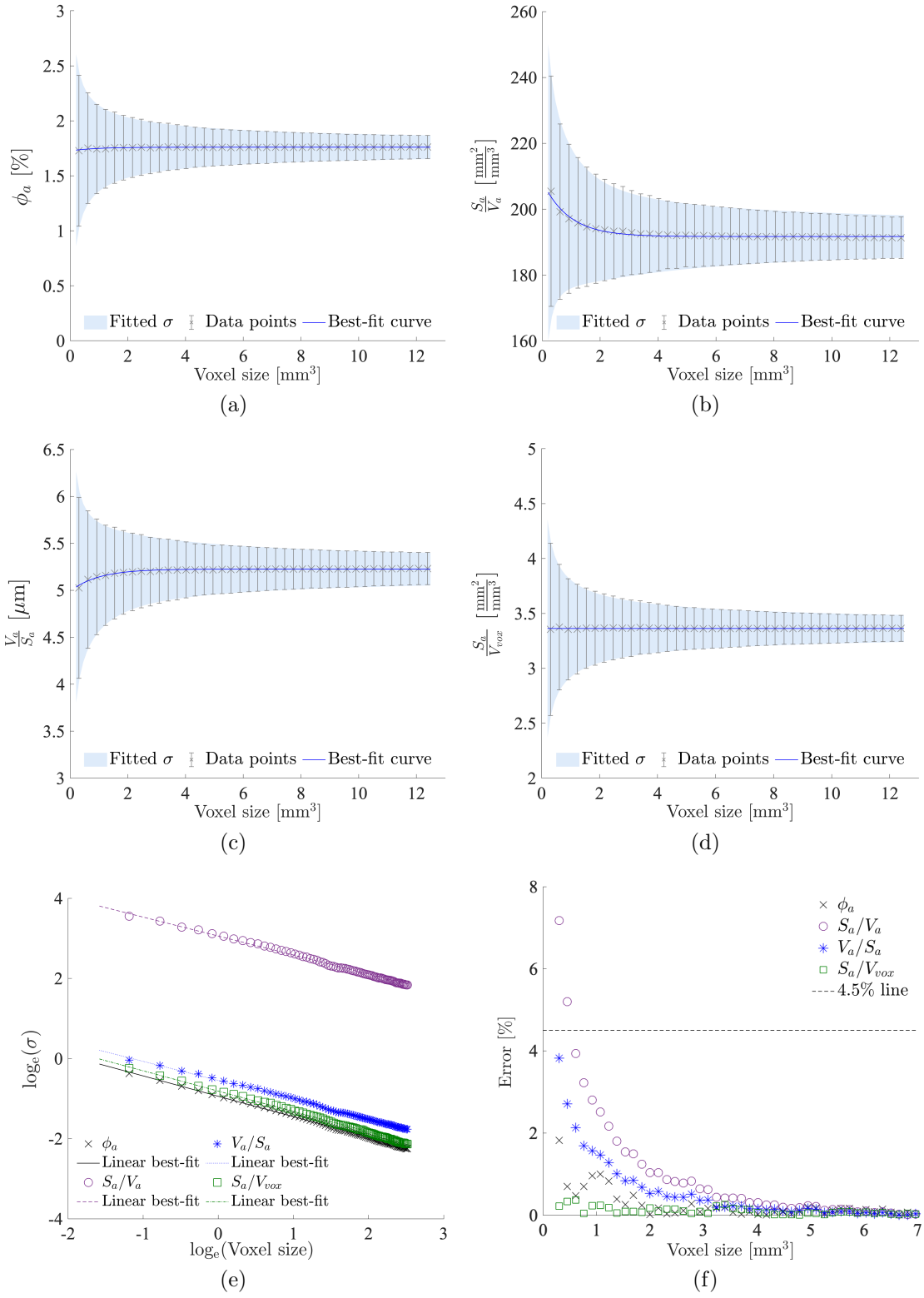


Figure 4.7: Best-fit curves (blue line) and fitted standard deviations (light blue shadow) of the parameters against voxel size (a–d); logarithm standard deviations and their linear best-fit lines (e); percentage errors of the arteriolar voxel parameter means (f).

Chapter 5

Numerical implementation

5.1 Finite element method

The finite element method (FEM) is a popular numerical method for solving partial differential equations (PDEs). It approximates the problem's solution by discretising the computational domain into a mesh consisting of finite number of elements with regular shapes, such as triangles in 2D and tetrahedra in 3D. Within each element, the solution is approximated by a function. Combining these functions together leads to a set of algebraic equations that describe the whole system. The solutions of this algebraic equation set are the unknown coefficients of the approximate solution function of the PDE.

The primary reason for choosing the FEM to implement the coupled flow-oxygen model is because there is software available that allows the approximate solutions of arbitrary PDEs to be obtained automatically. One such open-source software is FEniCS [152] which will be employed in this thesis. Additionally, the FEM is capable of handling complex geometries. A tetrahedral mesh can be automatically generated and refined both locally and globally to capture the shape of gyri, sulci, and ventricles. In addition to mesh refinement, the FEM also makes it easy to increase the order of the elements, which plays an important role in improving the approximation accuracy. Another key factor for modelling transport equations

that describe mass conservation is to have a numerical method that is conservative. Although the FEM is not conservative by default, choosing certain function spaces allows the FEM to become conservative. Convergence tests can also be performed to help deciding the combination of element size and order that minimise the error while maintaining a relatively low computational cost.

To solve the partial differential equations (given in their strong form) governing the oxygen model through the FEM, a variational form (or weak form) needs to be derived. Recall the strong form of the governing equations in a domain Ω under steady state conditions:

$$\vec{u}_a \cdot \nabla C_a = \phi_a D_a \nabla^2 C_a - \beta_{ac}(p_a - p_c)C_a - \frac{\kappa_a}{h_a}\frac{S_a}{V_a}\phi_a \left(\frac{\tau C_a}{\alpha_b} - \frac{C_t}{\alpha_t}\right); \tag{5.1a}$$

$$\vec{u}_c \cdot \nabla C_c = \phi_c D_c \nabla^2 C_c + \beta_{ac}(p_a - p_c)C_a - \beta_{cv}(p_c - p_v)C_c - \frac{\kappa_c}{h_c}\frac{S_c}{V_c}\phi_c \left(\frac{\tau C_c}{\alpha_b} - \frac{C_t}{\alpha_t}\right); \tag{5.1b}$$

$$0 = \phi_t D_t \nabla^2 C_t + \frac{\kappa_a}{h_a}\frac{S_a}{V_a}\phi_a \left(\frac{\tau C_a}{\alpha_b} - \frac{C_t}{\alpha_t}\right) + \frac{\kappa_c}{h_c}\frac{S_c}{V_c}\phi_c \left(\frac{\tau C_c}{\alpha_b} - \frac{C_t}{\alpha_t}\right) - \phi_t \frac{G_{\max} C_t}{C_t + C_{50}}, \tag{5.1c}$$

with the following boundary conditions (BCs):

$$C_i = C_i^0 \qquad \text{on } \Gamma_{\mathrm{D},i} \subset \partial\Omega; \tag{5.2a}$$

$$\nabla C_i \cdot \vec{n} = 0 \qquad \text{on } \Gamma_{\mathrm{N},i} \subset \partial\Omega. \tag{5.2b}$$

Here, i indicates a, c and t, $\partial\Omega$ is the boundary surface of Ω and $\vec{n}$ is the outward-pointing unit vector perpendicular to $\partial\Omega$. The Dirichlet boundary condition (DBC), Equation (5.2a), indicates that a value of C_i^0 is prescribed to C_i on the boundary $\Gamma_{\mathrm{D},i}$. The homogenous Neumann boundary condition (NBC), Equation (5.2b), ensures that no oxygen crosses the boundary $\Gamma_{\mathrm{N}} = \partial\Omega \setminus \Gamma_{\mathrm{D}}$.

Taking the arteriolar compartment as an example, the unknown C_a is the trial function and Equation (5.1a) is firstly multiplied by a test function v_a and integrated

over Ω, i.e.,

$$\int_\Omega \vec{u}_a \cdot \nabla C_a v_a dV = \int_\Omega \phi_a D_a \nabla^2 C_a v_a dV - \int_\Omega \beta_{ac}(p_a - p_c) C_a v_a dV - \int_\Omega \frac{\kappa_a}{h_a}\frac{S_a}{V_a}\phi_a \left(\frac{\tau C_a}{\alpha_b} - \frac{C_t}{\alpha_t}\right) v_a dV. \quad (5.3)$$

The order of the diffusion term is then reduced by applying the product rule and Gauss's theorem, resulting in the following expression

$$\int_\Omega \phi_a D_a \nabla^2 C_a v_a dV = \int_{\partial\Omega} \phi_a D_a \nabla C_a \cdot \vec{n} v_a dS - \int_\Omega \phi_a D_a \nabla C_a \cdot \nabla v_a dV. \quad (5.4)$$

The surface integral (first term on the right hand side) vanishes when DBCs or homogenous NBCs are enforced. The imposition of DBCs sets $v_a = 0$ because the solution at $\Gamma_{\mathrm{D},a}$ is now known; whereas, homogenous NBCs force $\nabla C_a \cdot \vec{n} = 0$ at $\Gamma_{\mathrm{N},a}$. Substituting the simplified Equation (5.4) into Equation (5.3) leads to the weak form of the equation for the arteriolar compartment:

$$\int_\Omega \vec{u}_a \cdot \nabla C_a v_a dV = -\int_\Omega \phi_a D_a \nabla C_a \cdot \nabla v_a dV - \int_\Omega \beta_{ac}(p_a - p_c) C_a v_a dV - \int_\Omega \frac{\kappa_a}{h_a}\frac{S_a}{V_a}\phi_a \left(\frac{\tau C_a}{\alpha_b} - \frac{C_t}{\alpha_t}\right) v_a dV. \quad (5.5)$$

The weak form of the capillary and tissue compartment equations can be derived in the same fashion and the results read as follows

$$\int_\Omega \vec{u}_c \cdot \nabla C_c v_c dV = -\int_\Omega \phi_c D_c \nabla C_c \cdot \nabla v_c dV + \int_\Omega \beta_{ac}(p_a - p_c) C_a v_c dV - \int_\Omega \beta_{cv}(p_c - p_v) C_c v_c dV - \int_\Omega \frac{\kappa_c}{h_c}\frac{S_c}{V_c}\phi_c \left(\frac{\tau C_c}{\alpha_b} - \frac{C_t}{\alpha_t}\right) v_c dV; \quad (5.6)$$

$$0 = \int_\Omega \frac{\kappa_a}{h_a}\frac{S_a}{V_a}\phi_a \left(\frac{\tau C_a}{\alpha_b} - \frac{C_t}{\alpha_t}\right) v_t dV + \int_\Omega \frac{\kappa_c}{h_c}\frac{S_c}{V_c}\phi_c \left(\frac{\tau C_c}{\alpha_b} - \frac{C_t}{\alpha_t}\right) v_t dV - \int_\Omega \phi_t \frac{G_{\max} C_t}{C_t + C_{50}} v_t dV. \quad (5.7)$$

Equations (5.5)–(5.7) are discretised by the continuous Bubnov-Galerkin method [153]. Both the test and trial functions belong to the H^1 Sobolev space, i.e., $v_i \in H^1(\Omega) : v_i = 0$ on $\Gamma_{\mathrm{D},i}$ and $C_i \in H^1(\Omega) : C_i = C_i^0$ on $\Gamma_{\mathrm{D},i}$. FEniCS [152] is employed here to obtain the numerical solutions of C_i with the standard Lagrange family of elements and the element order is specified prior to each simulation. Zeroth-order discontinuous Galerkin elements are used to capture the coupling coefficients. First-order continuous and zeroth-order discontinuous Galerkin elements are used to represent the pressure and the velocity, respectively, unless stated otherwise. The implementation of the oxygen model is verified through the method of manufactured solution in the next section.

5.2 Manufactured solution

To ensure that the numerical implementation is free from coding errors and is capable of approaching the exact solution, a mesh convergence test should be performed to evaluate the discretisation errors. As an exact solution could not be obtained due to the nonlinearity of the oxygen model, the method of manufactured solution (MS) [154, 155] is employed.

Benchmark solutions of the unknowns — in this case, the oxygen concentration of each compartment (C_a^{MS}, C_c^{MS} and C_t^{MS}) — are firstly constructed. Such solutions should be smooth analytical functions, complex enough to preserve all the terms in the governing equations, have sufficient number of non-trivial derivatives, and satisfy the boundary conditions; however, they do not need to be physically realistic [154, 155]. The solutions are then substituted into the strong form to compute the source terms which are added to their corresponding weak form equation. Solving Equations (5.5)–(5.7) now should produce the numerical solution $C_i^h = C_i^{\mathrm{MS}}$ for compartment i.

A unit cube (Figure 5.1), resembling a tissue column, is used to verify the code implementation. The top ($z = 1$) and bottom ($z = 0$) surface of the cube represent

the pial surface and the ventricles, respectively. In the arteriolar compartment, C_a^{MS} is applied as DBC to the cube's top surface and homogeneous NBC is applied to the bottom surface. For capillary and tissue compartments, homogeneous NBCs are applied to both the top and bottom surface of the cube. Additionally, periodic boundary conditions (PBCs) are imposed on the lateral faces of the cube for all compartments.

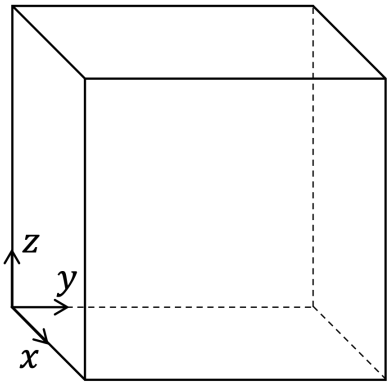


Figure 5.1: An illustration of the unit cube.

The manufactured solutions for the arteriolar, capillary, and tissue compartment are chosen to be

$$C_a^{\mathrm{MS}} = f(x) + f(y) + z^2\,; \tag{5.8a}$$

$$C_c^{\mathrm{MS}} = 2f(x) \times f(y) \times f(z)\,; \tag{5.8b}$$

$$C_t^{\mathrm{MS}} = f(x) \times f(y) \times f(z), \tag{5.8c}$$

where $f(\cdot)$ is a polynomial function. In the direction of x, for example, $f(\cdot)$ reads as

$$f(x) = 16x^4 - 32x^3 + 16x^2. \tag{5.9}$$

The use of polynomial functions in constructing the benchmark solutions minimises the approximation error as they are also used as the basis functions in the employed FEM. Figure 5.2a to 5.2c visualise the manufactured solutions in a unit cube for the arteriolar, capillary and tissue compartments. A sampling line, shown in white, is indicated for each compartment at (0.5, 0.5, z). Figure 5.2d to 5.2f illustrate the

values of C_a^{MS}, C_c^{MS} and C_t^{MS} along the sampling line.

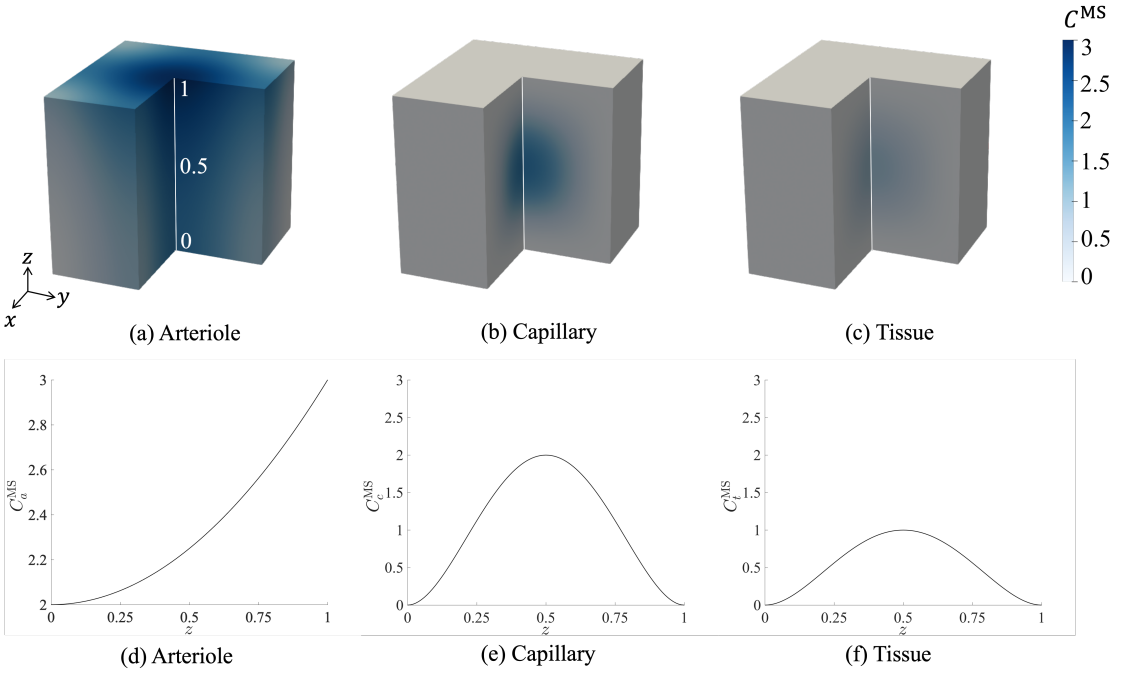


Figure 5.2: Visualisation of the manufactured solutions in a unit cube for (a) arteriole, (b) capillary and (c) tissue compartments with a sampling line at (0.5, 0.5, z). (d), (e) and (f) show the values of C_a^{MS}, C_c^{MS} and C_t^{MS}, respectively, along the sampling line.

Apart from the unknowns of the system, smooth functions are also assigned to inputs that vary over the domain. Expressions of the Darcy pressures (p_a^{MS}, p_c^{MS} and p_v^{MS}), permeability tensors ($\overline{\overline{K}}_a^{\mathrm{MS}}$ and $\overline{\overline{K}}_c^{\mathrm{MS}}$) and coupling coefficients (β_{ac}^{MS} and β_{cv}^{MS}) are taken from [29], and the Darcy velocities ($\vec{u}_a^{\mathrm{MS}}$ and $\vec{u}_c^{\mathrm{MS}}$) are calculated according to Equation (3.2). The same expression as used for β_{ac}^{MS} ($= 1.5 + 0.5\tanh(10z - 5)$) is chosen to represent the maximum consumption rate ($G_{\max}^{\mathrm{MS}}$) as shown in Figure 5.3. This hyperbolic tangent function is well suited for capturing the sudden change in material properties of grey and white matter [29]. Lastly, the rest of the parameters are assigned a value of 1 for simplicity.

The analytical expressions of the source terms (R_a, R_c and R_t) are then found by substituting the manufactured expressions into the strong form of the governing equations (Equation (5.1)); they are computed by using Mathematica 12.0 [156] and their expressions can be found in Appendix B.

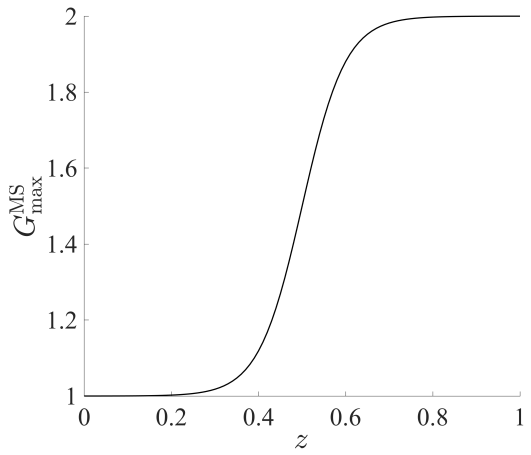
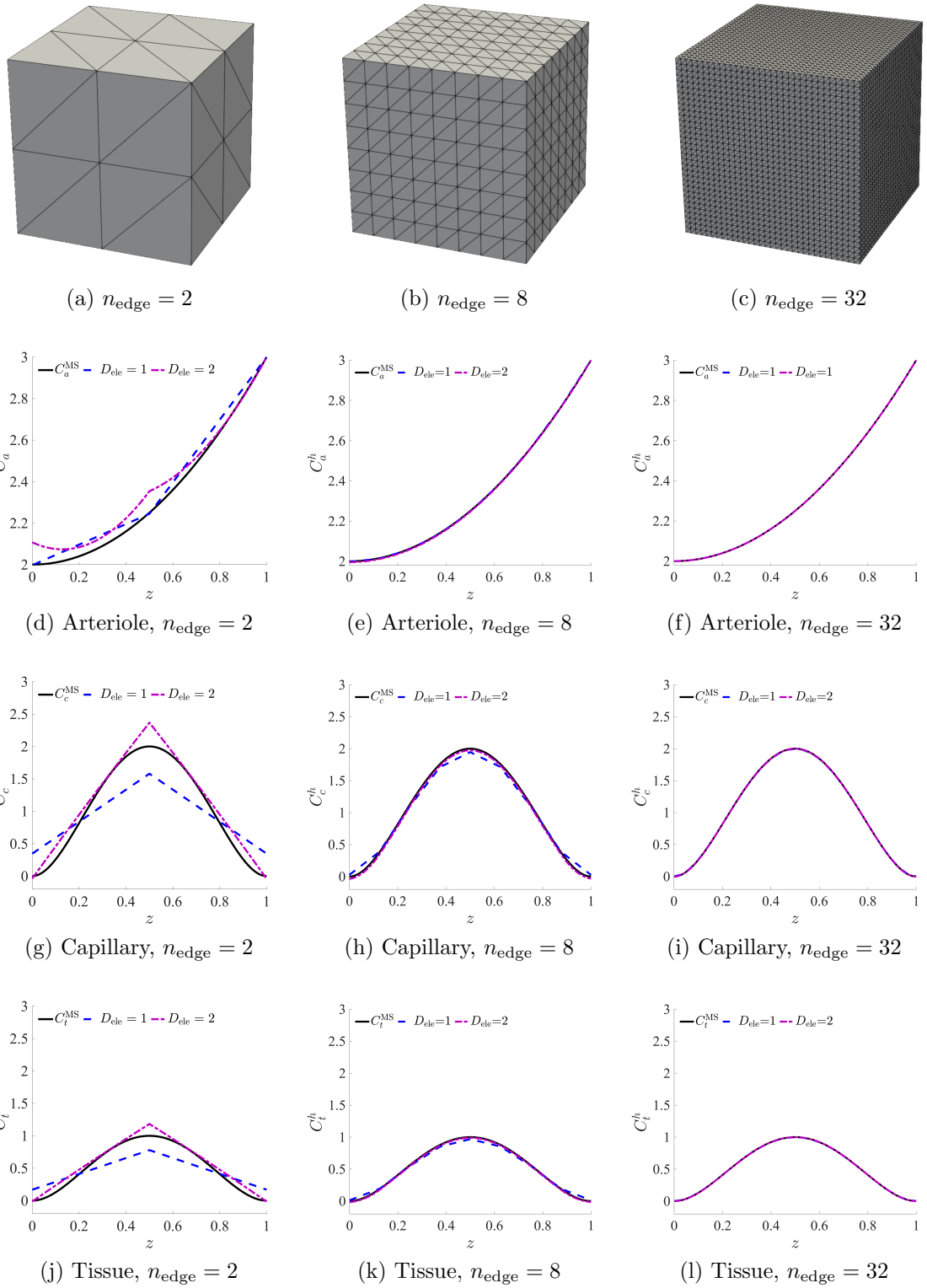


Figure 5.3: Plot of $G_{\max}^{\mathrm{MS}}$ along the sampling line.

To obtain the numerical solutions and perform the convergence test, the unit cube is uniformly meshed with tetrahedrons. The coarsest mesh has two elements along each edge of the cube ($n_{\mathrm{edge}} = 2$) with an element size ($h = 1/n_{\mathrm{edge}}$) of 0.5. The mesh is then uniformly refined four times with the finest mesh having $n_{\mathrm{edge}} = 32$ and $h = 0.03125$. Figures 5.4a–5.4c show the mesh at three refinement levels. Additionally, the effect of element degree/order (D_{ele}) on FE approximations of oxygen concentration is studied using linear ($D_{\mathrm{ele}} = 1$) and quadratic ($D_{\mathrm{ele}} = 2$) continuous Galerkin elements; the latter introduces an extra degree of freedom (DoF) at middle of each element edge. All the manufactured solutions and expressions are interpolated to the mesh with fourth-order polynomials which provide a sufficiently accurate approximation of the analytical functions.

The numerical solutions (C_i^h) along the sampling line of selected mesh sizes are plotted against the benchmark solutions (C_i^{MS}) for each compartment (see Figures 5.4d–5.4l). It can be seen from the figures that the FE approximation for all compartments improves as the mesh size reduces. The second-order FE scheme converges faster towards analytical solutions because of its quadratic basis functions' ability to capture curves; this is highlighted in Figures 5.4d, 5.4h and 5.4k. Nonetheless, given sufficient spatial resolution (i.e., $n_{\mathrm{edge}} = 32$), the first-order FE scheme is also able to reach a very good agreement with the manufactured solutions (see Figures 5.4f, 5.4i and 5.4l).



(a) $n_{\text{edge}} = 2$ (b) $n_{\text{edge}} = 8$ (c) $n_{\text{edge}} = 32$

(d) Arteriole, $n_{\text{edge}} = 2$ (e) Arteriole, $n_{\text{edge}} = 8$ (f) Arteriole, $n_{\text{edge}} = 32$

(g) Capillary, $n_{\text{edge}} = 2$ (h) Capillary, $n_{\text{edge}} = 8$ (i) Capillary, $n_{\text{edge}} = 32$

(j) Tissue, $n_{\text{edge}} = 2$ (k) Tissue, $n_{\text{edge}} = 8$ (l) Tissue, $n_{\text{edge}} = 32$

Figure 5.4: Illustrations of the unit cube mesh at different refinement levels: (a) $n_{\text{edge}} = 2$, (b) $n_{\text{edge}} = 8$ and (c) $n_{\text{edge}} = 32$; plots of numerical solutions against benchmark solutions along the sampling line for each compartment: (d)–(f) arteriole, (g)–(i) capillary and (j)–(l) tissue.

The discretisation errors can be quantified by the L2 norm over the entire computational domain which is calculated as

$$E_i = \sqrt{\int_\Omega (C_i^{\mathrm{MS}} - C_i^h)^2 \, dV} \tag{5.10}$$

with i indicating either arteriolar, capillary or tissue compartment. Additionally, averaged relative errors (E_{rel}) are calculated as

$$E_{\mathrm{rel}} = \frac{1}{3} \sum_i \left(\frac{E_i}{\sqrt{\int_\Omega (C_i^{\mathrm{MS}})^2 \, dV}} \right) \times 100\%, \tag{5.11}$$

which demonstrates the size of the L2 norm compared to the exact solutions. Results of the errors and computation time are summarised in Table 5.1 along with their corresponding mesh properties.

n_{edge}	h	n_{ele}	n_{DoF}	E_a	E_c	E_t	E_{rel} [%]	time*[s]
$D_{\mathrm{ele}} = 1$								
2	0.5	48	81	0.1077	0.1971	0.0998	27.81	0.058
4	0.25	384	375	0.0975	0.1498	0.0754	21.49	0.395
8	0.125	3,072	2,187	0.0282	0.0515	0.0261	7.291	2.972
16	0.0625	24,576	14,739	0.0073	0.0141	0.0071	1.989	23.87
32	0.03125	196,608	107,811	0.0018	0.0036	0.0018	0.509	221.5
$D_{\mathrm{ele}} = 2$								
2	0.5	48	375	0.0986	0.0963	0.0505	10.15	0.182
4	0.25	384	2,187	0.0135	0.0213	0.0106	3.053	1.231
8	0.125	3,072	14,739	0.0017	0.0028	0.0014	0.404	10.10
16	0.0625	24,576	107,811	0.0002	0.0004	0.0002	0.051	114.8
32	0.03125	196,608	823,875	0.00003	0.00006	0.00009	0.016	2,586

Table 5.1: Mesh convergence study result: discretisation errors and computation time with corresponding mesh properties. *These simulations were run using 1 core of an Intel Xeon Platinum 8268 processor with 8GB RAM apart from the simulation with $D_{\mathrm{ele}} = 2$ and $n_{\mathrm{edge}} = 32$ which required 64GB RAM.

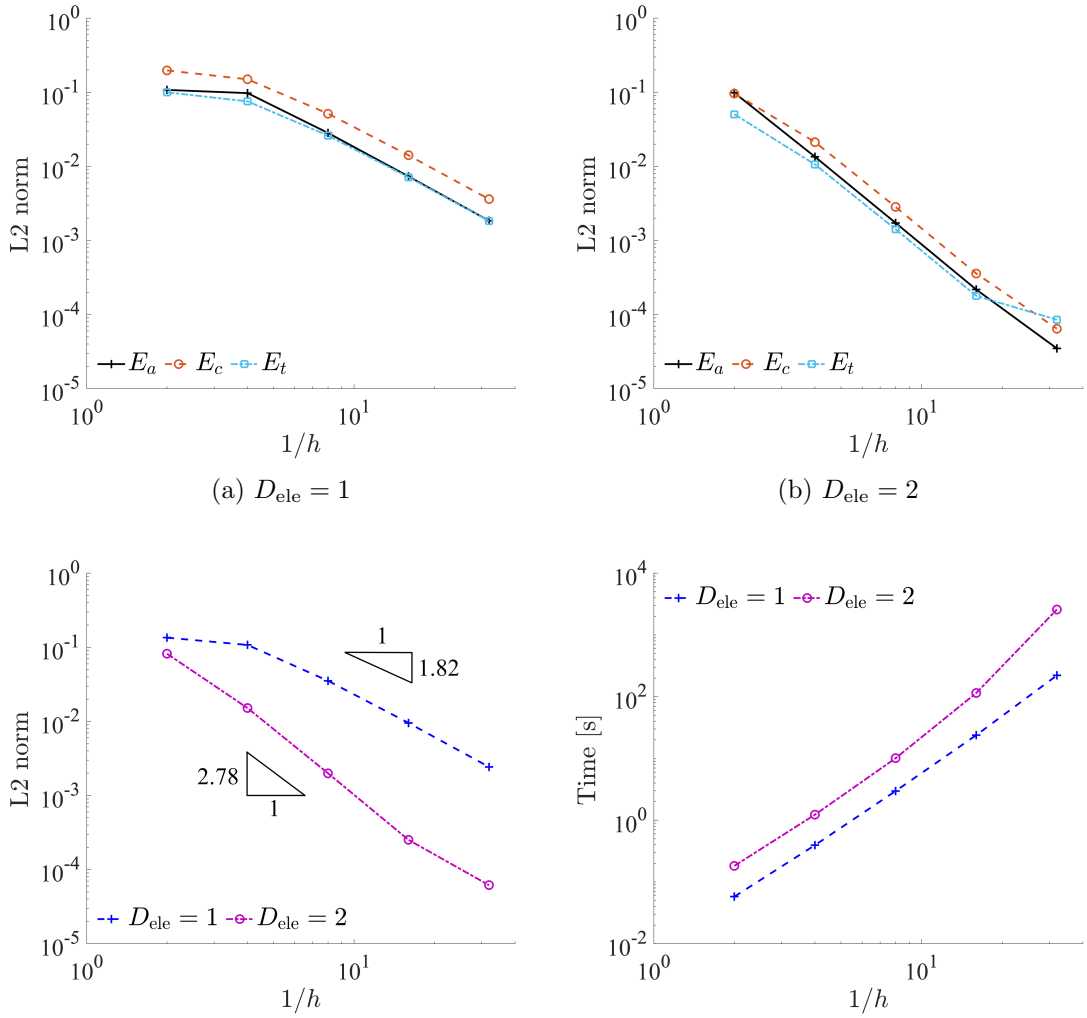
Agreeing with the previous observations, discretisation errors decrease as the mesh becomes finer. The averaged relative errors of the finest mesh are 0.51% and 0.016%

for the first and second-order scheme, respectively. This further highlights that the numerical implementation is suitable to handle the governing equations and that the FE approximation is capable of reaching sufficiently accurate solutions.

To better analyse the results, L2 norms are plotted against the reciprocal of the mesh size (which is equal to n_{edge} in the case of the unit cube) on logarithmic scales. Figures 5.5a and 5.5b show the convergence of discretisation errors for each individual compartment. As shown in the figures, numerical solutions of all compartments of a given FE scheme converge at a similar rate as the mesh size decreases. In particular, error reduction in the arteriolar compartment has the steepest slope, which agrees with the sampling line plots in Figure 5.4; this is because the manufactured solution of the arteriolar compartment has a polynomial of lower order compared to those of capillary and tissue compartments.

Between the two FE schemes, a better approximation is achieved by using second-order elements for all mesh sizes. This is highlighted by Figure 5.5c where discretisation errors averaged across all compartments are plotted against $1/h$. Both the linear and quadratic scheme achieved convergence rates (1.82 and 2.78, respectively) that are close to their respective theoretical values (order + 1). In terms of computational costs, using second-order elements is always more expensive as shown in Figure 5.5d; the simulation time of the quadratic scheme increases significantly as the mesh becomes finer.

Through this convergence study, it has been demonstrated that the oxygen model is correctly implemented and that the chosen numerical method is capable of reaching sufficiently accurate solutions; both linear and quadratic FE schemes achieved a relative error of $<1\%$ with the finest mesh. Although the second-order elements are better at capturing curvature and producing more accurate solutions for a given mesh, it comes at a greater cost in terms of both computational time and resources. Therefore, the linear FE scheme with a finer mesh will be employed to solve for the oxygen concentration.



(a) $D_{ele} = 1$ (b) $D_{ele} = 2$

(c) Average error (d) Computation time

Figure 5.5: Plots of mesh convergence with (a) first-order elements, (b) second-order elements and (c) errors averaged across all compartments; (d) shows the trend of computation time as the mesh size reduces.

5.3 One-dimensional brain tissue column

After evaluating the suitability of the FEM and performing the mesh convergence study in the previous section, the coupled flow-oxygen model is firstly solved on a one-dimensional (1D) brain tissue column. The main reason of adapting this 1D model for the initial investigation of oxygen transport is its low computational cost. It is shown with the perfusion model that the 1D simulations are about 3000 times faster compared to the 3D brain simulations [29], and that the computational time of the oxygen model is about one magnitude longer than that of the perfusion model

(see Table 5.1 and [29]).

The 1D equivalent model contains both grey and white matter, and all the model parameters are identical to those used for the 3D brain model. The length of this tissue column was determined through optimisation using the perfusion model by Józsa *et al.* [29], which has a value of 21.54 [mm]. The equivalent lengths of the grey and white matter are 13.55 [mm] and 7.99 [mm], respectively, which ensure that the volume-averaged perfusion values of the 1D model are the same as that of the 3D model.

Interval meshes with 1000 first-order elements are used for the simulations. A single value of each parameter is selected from the range summarised earlier in Table 4.1. These values together with the geometric parameters obtained in the previous chapter are listed in Table 5.2. Values of $G_{\max}$ for both grey (GM) and white matter (WM) will be optimised later in Section 5.4, and a sensitivity analysis on the parameters will be performed in Section 5.5.

Parameter	Value	Unit	Reference
D_a	1.6×10^{-3}	mm^2/s	[144]
D_c	1.6×10^{-3}	mm^2/s	[144]
D_t	1.8×10^{-3}	mm^2/s	[98, 99]
κ_a	5×10^{-8}	$\mathrm{mm}^3\,\mathrm{O}_2/(\mathrm{mmHg}\cdot\mathrm{mm}\cdot\mathrm{s})$	[33, 72, 93]
κ_c	5×10^{-8}	$\mathrm{mm}^3\,\mathrm{O}_2/(\mathrm{mmHg}\cdot\mathrm{mm}\cdot\mathrm{s})$	[33, 72, 93]
h_a	3.32×10^{-3}	mm	[72]
h_c	3.09×10^{-4}	mm	[72]
α_b	3.11×10^{-5}	$\mathrm{mm}^3\,\mathrm{O}_2/(\mathrm{mm}^3\,\mathrm{blood}\cdot\mathrm{mmHg})$	[67, 146]
α_t	2.60×10^{-5}	$\mathrm{mm}^3\,\mathrm{O}_2/(\mathrm{mm}^3\,\mathrm{tissue}\cdot\mathrm{mmHg})$	[99]
τ	0.01	-	[139]
$G_{\max}^{\mathrm{GM}}$	8.2×10^{-4}	$\mathrm{mm}^3\,\mathrm{O}_2/(\mathrm{mm}^3\,\mathrm{tissue}\cdot\mathrm{s})$	[99]
$G_{\max}^{\mathrm{WM}}$	2.05×10^{-4}	$\mathrm{mm}^3\,\mathrm{O}_2/(\mathrm{mm}^3\,\mathrm{tissue}\cdot\mathrm{s})$	[99]
C_{50}	2.6×10^{-5}	$\mathrm{mm}^3\,\mathrm{O}_2/(\mathrm{mm}^3\,\mathrm{tissue})$	-
ϕ_a	1.76	%	Chapter 4
ϕ_c	1.42	%	Chapter 4
S_a/V_a	191.70	$\mathrm{mm}^2/\mathrm{mm}^3\,\mathrm{blood}$	Chapter 4
S_c/V_c	627.31	$\mathrm{mm}^2/\mathrm{mm}^3\,\mathrm{blood}$	Chapter 4

Table 5.2: Selected parameter values for the oxygen model.

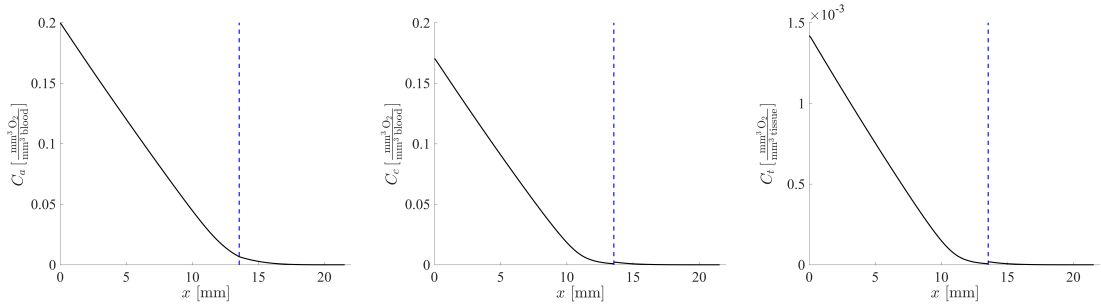
5.3.1 Three-compartment model

The last value that needs to be determined before the simulation of the 3-compartment model is the DBC at the arteriole inlet. The value of oxygen partial pressure in arterioles, just before their intra-cortical penetrating points, has been found to be 80–85 [mmHg] in rats and cats [84, 85, 87, 157]. A P_{O_2} of 83 [mmHg] is thus chosen to be the inlet partial pressure for this model. By using the Hill equation (Equation (2.1)) with $P_{50} = 26.2$ [mmHg] and $n = 2.5$ [80], oxygen saturation at the arteriole inlet is calculated to be 94.70%. Finally oxygen concentration on the pial surface is calculated as

$$C_a^{\text{pial}} = B_{O_2} C_{\text{Hb}} S_{O_2} + \alpha_b P_{O_2}^{\text{pial}}, \tag{5.12}$$

where B_{O_2} is the Hüfner constant with a value of 1.39 [mm^3 O_2/g Hb] [90] and C_{Hb} is the haemoglobin concentration in normal blood with a value of 0.15 [g Hb/mm^3 blood] [79]. This gives a DBC value of $C_a^{\text{pial}} = 0.20$ [mm^3 O_2/mm^3 blood].

The simulation results for each compartment are plotted in Figure 5.6; $x = 0$ [mm] indicates the pial surface and the dotted blue lines mark the grey matter and white matter interface. As shown in the figure, oxygen concentration decreases as the vessels penetrate deeper into the brain for all compartments. Although this behaviour is expected, there is little oxygen left by the time blood reaches the white matter.



(a) Arteriole (b) Capillary (c) Tissue

Figure 5.6: Simulation results of the 3-compartment oxygen model in a 1D tissue column with the G_{max} values listed in Table 5.2. $x = 0$ [mm] indicates the pial surface and the blue dash lines mark the grey matter and white matter interface.

To examine the results quantitatively, volume averaged values of oxygen concentration, partial pressure and saturation are calculated for each compartment as well as for each subdomain, i.e., grey matter and white matter. To be consistent with the model, volume averaged partial pressure of oxygen is calculated as

$$\langle P^i_{O_2} \rangle = \frac{1}{V_{\text{mesh}}} \int_\Omega \frac{\tau C_i}{\alpha_b} dV \quad \text{and} \quad \langle P^t_{O_2} \rangle = \frac{1}{V_{\text{mesh}}} \int_\Omega \frac{C_t}{\alpha_t} dV, \tag{5.13}$$

where V_{mesh} is the total volume of the domain and $i \in [a, c]$. S_{O_2} is then calculated according to the Hill equation. Note that with $\tau = 0.01$, the linearised approximation overestimates the value of $P^b_{O_2}$ when $0.052 < C_b < 0.187$ [mm^3 O$_2$/mm^3 blood] and underestimates the value of $P^b_{O_2}$ otherwise; the averaged difference between the two is 6.62 [mmHg]. This limitation will be further explored in Section 7.2.2. Additionally, volume averaged cerebral metabolic rate of oxygen ($\langle \text{CMRO}_2 \rangle$) of the model is computed as

$$\langle \text{CMRO}_2 \rangle = \frac{1}{V_{\text{mesh}}} \int_\Omega \phi_t \frac{G_{\max} C_t}{C_t + C_{50}} dV. \tag{5.14}$$

As shown in Table 5.3, the averaged oxygen level is significantly below the physiological range for each compartment. Although the tissue oxygenation in the grey matter is at an acceptable level, this is not the case in the white matter. The near zero P_{O_2} in the white matter across all compartment suggests that not enough oxygen is being delivered to the subcortical regions.

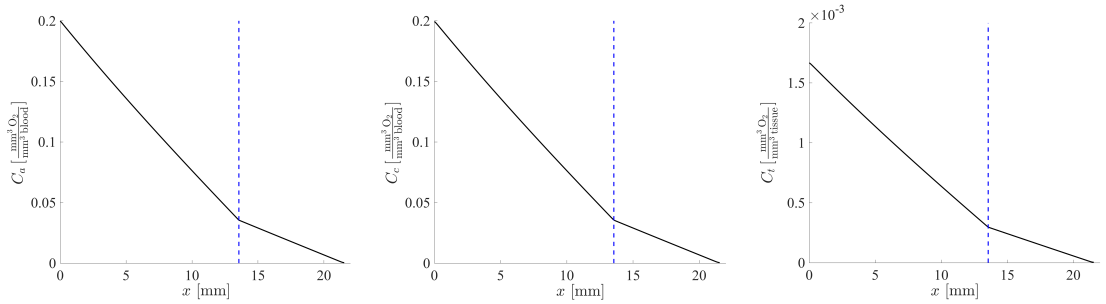
There are a few factors that may explain this behaviour. The most intuitive one is that the consumption rate in the grey matter is much higher than that in the white matter. This is likely to have been a driving factor behind the steep reduction of oxygen in the cortex. To examine the impact of the consumption rate on oxygen delivery, the model was run without the metabolic term and the results are shown in Table 5.4 and Figure 5.7.

	$\langle C \rangle$ $\left[\frac{\text{mm}^3\,\text{O}_2}{\text{mm}^3\,\text{blood(/tissue)}}\right]$	$\langle P_{O_2} \rangle$ [mmHg]	$\langle S_{O_2} \rangle$ [%]	$\langle \text{CMRO}_2 \rangle$ $\left[\frac{\text{mm}^3\,\text{O}_2}{\text{mm}^3\,\text{tissue}\cdot\text{s}}\right]$
Whole				
Arteriole	6.04×10^{-2}	19.14	31.51	-
Capillary	4.38×10^{-2}	14.10	23.62	-
Tissue	3.64×10^{-4}	13.99	-	4.30×10^{-4}
Grey matter				
Arteriole	9.51×10^{-2}	30.58	50.01	-
Capillary	6.97×10^{-2}	22.31	37.50	-
Tissue	5.76×10^{-4}	22.14	-	6.72×10^{-4}
White matter				
Arteriole	1.23×10^{-3}	0.39	0.016	-
Capillary	3.68×10^{-4}	0.12	0.00092	-
Tissue	3.03×10^{-6}	0.12	-	1.70×10^{-5}

Table 5.3: Volume averaged values of oxygen concentration, partial pressure, saturation, and CMRO_2 of the 3-compartment oxygen model in a 1D tissue column with the $G_{\max}$ values listed in Table 5.2.

	$\langle C \rangle$ $\left[\frac{\text{mm}^3\,\text{O}_2}{\text{mm}^3\,\text{blood(/tissue)}}\right]$	$\langle P_{O_2} \rangle$ [mmHg]	$\langle S_{O_2} \rangle$ [%]	$\langle \text{CMRO}_2 \rangle$ $\left[\frac{\text{mm}^3\,\text{O}_2}{\text{mm}^3\,\text{tissue}\cdot\text{s}}\right]$
Whole				
Arteriole	7.93×10^{-2}	25.48	40.65	
Capillary	7.93×10^{-2}	25.48	40.65	-
Tissue	6.63×10^{-4}	25.48	-	
Grey matter				
Arteriole	1.15×10^{-1}	37.11	62.58	
Capillary	1.15×10^{-1}	37.11	62.58	-
Tissue	9.65×10^{-4}	37.11	-	
White matter				
Arteriole	1.77×10^{-2}	5.68	5.68	
Capillary	1.77×10^{-2}	5.68	5.68	-
Tissue	1.48×10^{-4}	5.68	-	

Table 5.4: Volume averaged values of oxygen concentration, partial pressure, saturation, and CMRO_2 of the 3-compartment oxygen model in a 1D tissue column with no metabolism.



(a) (b) (c)

Figure 5.7: Simulation results of the 3-compartment oxygen model in a 1D tissue column with no metabolism. $x = 0$ [mm] indicates the pial surface and the blue dash lines mark the grey matter and white matter interface.

When there is no oxygen consumption, all compartments have the same P_{O_2} values under steady state as expected. Although this condition slightly increases the oxygen level in the system, it is still below the physiological range especially in the white matter. It can be seen from Figure 5.7 that oxygen decreases rapidly in the cortex and then at a slower rate in the white matter until reaching almost zero at the ventricles. This simulation has shown that oxygen consumption is not the main sink of this model. However, the different rate at which oxygen concentration reduces in the grey and white matter indicates that the coupling coefficients, being the other parameters that differ in the grey and white matter, play a crucial role in maintaining oxygen delivery.

Values of the grey matter coupling coefficients (β^{GM}) after optimisation are about 2.54 times larger than the white matter values (β^{WM}) [28] (also see Table 3.1). Perfusion (F_{blood}) value along the 1D domain obtained from the flow model is plotted in Figure 5.8, which acts as the inter-compartment advection coefficient for oxygen transport, i.e.,

$$F_{\mathrm{blood}} \approx \beta_{ac}(p_a - p_c) \approx \beta_{cv}(p_c - p_v). \tag{5.15}$$

When there is no metabolism, the intra-compartment advection term ($\vec{u} \cdot \nabla C$) advects oxygen, within the arteriolar compartment, at a volume-averaged rate of 0.0011 [mm^3 $O_2/(\mathrm{mm}^3$ blood $\cdot$ s)] from the pial surface towards the grey-white matter in-

terface; the inter-compartment advection coefficient plotted in Figure 5.8 transports oxygen at the same rate from the arterioles to the capillaries. This indicates that only less than half of the oxygen at any given depth is being delivered towards the deeper layer of the arteriolar compartment as the only source of oxygen is from the pial surface. Although the capillary compartment receives a volume source of oxygen from the arteriolar compartment at a rate of 0.0011 [mm^3 O_2/(mm^3 blood $\cdot$ s)] in the grey matter, it is also the inter-compartment advection rate for oxygen from capillaries to venules. With relatively small intra-compartment advection and diffusion rates, oxygen is predominantly transported into the venules before it is able to distribute within the capillary compartment.

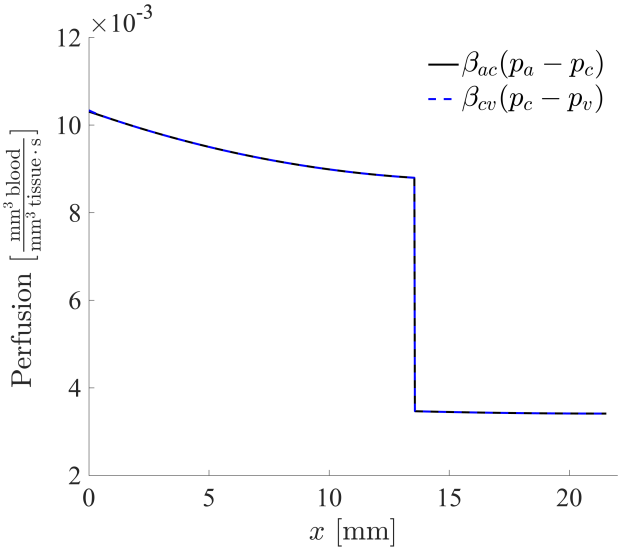


Figure 5.8: Inter-compartment advection coefficients plotted along the sampling line.

Altering the coupling coefficient values could reduce the inter-compartment transport rate in the grey matter and prevent a large amount of oxygen from leaving the system too close to the pial surface; however, this would not guarantee the perfusion values to be within the physiological range. As oxygen is advected around the brain through blood, a good perfusion level should, in theory, provide a good oxygen level. A factor that may explain this behaviour is the lack of information on the white matter vasculature, especially the Group 6 arterioles which are not included in the current model. This group of arterioles originates at the pial surface and exclusively

vascularises the white matter [45]. If included, it would allow the white matter to be better oxygenated through a more direct pathway.

Therefore, one way to improve the oxygen level in the white matter is to have an additional compartment for the Group 6 arterioles. However, the only statistical information available regarding these vessels is their diameter range, which is not enough for model construction. Another way is to consider a fresh assumption.

Assumption 4: No O_2 transport from arteriolar to tissue compartment. Recent research has shown that arterioles directly contribute to tissue oxygenation [63,64] and may be the sole source of oxygen in the Pfeifer space [62]. However, from the modelling perspective, capillaries are still the main source of oxygen for tissue; the inter-compartment diffusion coefficients are 5.08×10^{-5} and $1.44\ \times10^{-3}$ [mm^3 $O_2/(\mathrm{mmHg}\cdot\mathrm{mm}^3$ blood $\cdot\,\mathrm{s})$] for arterioles and capillaries, respectively. Although the oxygen partial pressure gradient between arterioles and tissue is larger than that between capillaries and tissue when metabolism is present, capillaries transport oxygen to the tissue at a rate that is about 30 times faster than arterioles in the grey matter.

Enforcing the above assumption reduces the arteriolar compartment into a volume source that supplies the grey and white matter in the capillary compartment with the same level of oxygen. This may result in an overestimation of the oxygen level in the white matter; however, further simplification is necessary due to the lack of statistics on the physiological values of oxygen level in the white matter vessels.

5.3.2 Two-compartment model

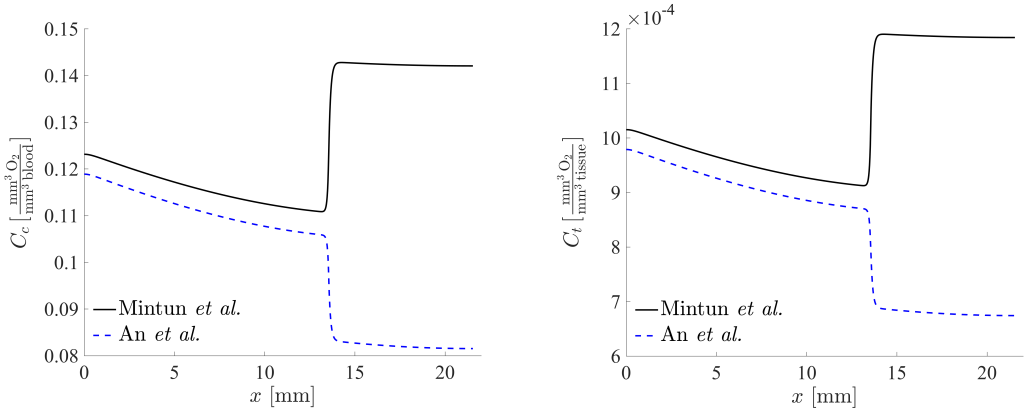
Adopting Assumption 4 reduces the oxygen model into a 2-compartment model consisting of just capillary and tissue:

$$\vec{u}_c\cdot\nabla C_c=\phi_c D_c\nabla^2 C_c+\beta_{ac}(p_a-p_c)C_a-\beta_{cv}(p_c-p_v)C_c-\frac{\kappa_c}{h_c}\frac{S_c}{V_c}\phi_c\left(\frac{\tau C_c}{\alpha_b}-\frac{C_t}{\alpha_t}\right); \tag{5.16a}$$

$$0 = \phi_t D_t \nabla^2 C_t + \frac{\kappa_c}{h_c}\frac{S_c}{V_c}\phi_c \left(\frac{\tau C_c}{\alpha_b} - \frac{C_t}{\alpha_t}\right) - \phi_t \frac{G_{\max} C_t}{C_t + C_{50}}, \tag{5.16b}$$

where C_a is now a constant with a value of 0.2 [mm^3 O_2/mm^3 blood].

Figure 5.9 shows the simulation results of the 2-compartment model with two sets of metabolic rates. The solid black lines denote results using the $G_{\max}$ values listed in Table 5.2 and the blue dash lines represent results using the mean metabolic rates taken from An *et al.* [147] as $G_{\max}$. The latter has a comparable $G_{\max}^{\mathrm{GM}}$ value (8.67×10^{-4} [mm^3 O_2/(mm^3 tissue $\cdot$ s)]) as the former while having a $G_{\max}^{\mathrm{WM}}$ value (4.26×10^{-4} [mm^3 O_2/(mm^3 tissue $\cdot$ s)]) twice as large as the Mintun *et al.* [99] rates.



(a) Capillary (b) Tissue

Figure 5.9: Simulation results of the 2-compartment oxygen model in a 1D tissue column with metabolic rate from Mintun *et al.* [99] (black solid line) and An *et al.* [147] (blue dash line). $x = 0$ [mm] indicates the pial surface.

It can be seen from the figure that choosing different oxygen consumption rates leads to qualitatively different distributions of oxygen concentration in the grey and white matter. The source of oxygen for the capillary compartment is now constant throughout the entire domain; perfusion in the white matter thus drops to about a third of that in the grey matter. However, $G_{\max}^{\mathrm{WM}}$ from Mintun *et al.* is only one quarter that of $G_{\max}^{\mathrm{GM}}$, resulting in a higher oxygen level in the white matter. In contrast, An *et al.*'s oxygen consumption rate in the white matter is about a half of

that in the grey matter, leaving a lower oxygen level in the former.

Nonetheless, oxygen levels in both grey and white matter are within the physiological range with either consumption rates as shown in Tables 5.5 and 5.6. As summarised in Table 4.1, the reported $CMRO_2$ appears to have a large range; values for the grey and white matter range between $5.05–10.33\times10^{-4}$ and $2.05–4.73\times10^{-4}$ $[mm^3\,O_2/(mm^3\,tissue\cdot s)]$, respectively. Since the choice of metabolic rate significantly affects the distribution of oxygen along the depth of the brain, the best way to find the most suitable value of G_{max} in this context thus appears to be through optimisation.

	$\langle C\rangle$ $\left[\frac{mm^3\,O_2}{mm^3\,blood(/tissue)}\right]$	$\langle P_{O_2}\rangle$ [mmHg]	$\langle S_{O_2}\rangle$ [%]	$\langle CMRO_2\rangle$ $\left[\frac{mm^3\,O_2}{mm^3\,tissue\cdot s}\right]$
Whole				
Capillary	1.26×10^{-1}	40.41	74.16	-
Tissue	1.04×10^{-3}	40.02	-	5.68×10^{-4}
Grey matter				
Capillary	1.16×10^{-1}	37.30	70.69	-
Tissue	9.55×10^{-4}	36.75	-	7.86×10^{-4}
White matter				
Capillary	1.42×10^{-1}	45.71	80.08	-
Tissue	1.18×10^{-3}	45.58	-	1.98×10^{-4}

Table 5.5: Volume averaged values of oxygen concentration, partial pressure, saturation, and $CMRO_2$ of the 2-compartment oxygen model in a 1D tissue column with metabolic rate taken from Mintun *et al.* [99].

5.4 Parameter optimisation

Parameter optimisation requires solving the full governing equation set over the entire computational domain multiple times, which is time-communing and needs a lot of computational resources. Volume averaging the equations could help speed up the optimisation process; therefore, the oxygen model is simplified into a set of algebraic equations. We derive the grey and white matter equations separately

	$\langle C \rangle$ $\left[\frac{\text{mm}^3\,\text{O}_2}{\text{mm}^3\,\text{blood(/tissue)}}\right]$	$\langle P_{O_2} \rangle$ [mmHg]	$\langle S_{O_2} \rangle$ [%]	$\langle \text{CMRO}_2 \rangle$ $\left[\frac{\text{mm}^3\,\text{O}_2}{\text{mm}^3\,\text{tissue}\cdot\text{s}}\right]$
Whole				
Capillary	1.00×10^{-1}	32.21	61.83	-
Tissue	8.28×10^{-4}	31.84	-	6.73×10^{-4}
Grey matter				
Capillary	1.11×10^{-1}	35.75	68.43	-
Tissue	9.15×10^{-4}	35.17	-	8.30×10^{-4}
White matter				
Capillary	8.23×10^{-2}	26.45	50.58	-
Tissue	6.80×10^{-4}	26.17	-	4.05×10^{-4}

Table 5.6: Volume averaged values of oxygen concentration, partial pressure, saturation, and CMRO_2 of the 2-compartment oxygen model in a 1D tissue column with metabolic rate taken from An *et al.* [147].

because of the volume-averaged nature of the algebraic equations and the fact that $G_{\max}$ is different between the grey and white matters. Before starting, the algebraic equation set of the flow model and the assumptions used are briefly introduced as these are closely coupled with the oxygen model. Taken from [28], the governing equations of the flow model averaged over the grey matter volume reads as

$$-\frac{Q_a^{\text{GM}}}{V_{\text{GM}}} - \beta_{ac}^{\text{GM}}\left(\langle p_a\rangle^{\text{GM}} - \langle p_c\rangle^{\text{GM}}\right) = 0; \tag{5.17a}$$

$$-\frac{Q_c^{\text{GM}}}{V_{\text{GM}}} + \beta_{ac}^{\text{GM}}\left(\langle p_a\rangle^{\text{GM}} - \langle p_c\rangle^{\text{GM}}\right) - \beta_{cv}^{\text{GM}}\left(\langle p_c\rangle^{\text{GM}} - \langle p_v\rangle^{\text{GM}}\right) = 0; \tag{5.17b}$$

$$-\frac{Q_v^{\text{GM}}}{V_{\text{GM}}} + \beta_{cv}^{\text{GM}}\left(\langle p_c\rangle^{\text{GM}} - \langle p_v\rangle^{\text{GM}}\right) = 0. \tag{5.17c}$$

Consistent with previous notations, the angle brackets indicates volume-averaged quantities. V_{GM} is the grey matter volume and Q_i^{GM} is the volumetric flow rate through the grey matter surface ($\partial\Omega_{\text{GM}}$) in compartment i:

$$Q_i^{\text{GM}} = -\int_{\partial\Omega_{\text{GM}}} \overline{\overline{K}}_i \nabla p_i \cdot \vec{n}\, dS. \tag{5.18}$$

Given that blood flow through the boundary surfaces in the capillary compartment

is zero [28] and that both k_a and k_v are several orders of magnitude larger than k_c, it can be assumed that $Q_c^{\mathrm{GM}}/V_{\mathrm{GM}} \approx 0$. This suggests that blood flowing through the interface of grey and white matter in the capillary compartment is negligible, leading to the following relationship:

$$F_{\mathrm{blood}}^{\mathrm{GM}} = -\frac{Q_a^{\mathrm{GM}}}{V_{\mathrm{GM}}} = \beta_{ac}^{\mathrm{GM}} \left(\langle p_a \rangle^{\mathrm{GM}} - \langle p_c \rangle^{\mathrm{GM}} \right) = \beta_{cv}^{\mathrm{GM}} \left(\langle p_c \rangle^{\mathrm{GM}} - \langle p_v \rangle^{\mathrm{GM}} \right), \tag{5.19}$$

which is also the basis for Equation (5.15).

Now for the oxygen model, starting with the capillary compartment, we first integrate Equation (5.16a) over the grey matter domain (Ω_{GM}) which leads to

$$\begin{aligned} \int_{\Omega_{\mathrm{GM}}} \vec{u}_c \cdot \nabla C_c \, dV = \phi_c D_c \int_{\Omega_{\mathrm{GM}}} \nabla^2 C_c \, dV \\ + \beta_{ac}^{\mathrm{GM}} C_a \int_{\Omega_{\mathrm{GM}}} p_a^{\mathrm{GM}} - p_c^{\mathrm{GM}} \, dV \\ - \beta_{cv}^{\mathrm{GM}} \int_{\Omega_{\mathrm{GM}}} \left(p_c^{\mathrm{GM}} - p_v^{\mathrm{GM}} \right) C_c \, dV \\ - \frac{\kappa_c}{h_c} \frac{S_c}{V_c} \phi_c \int_{\Omega_{\mathrm{GM}}} \frac{\tau C_c}{\alpha_b} - \frac{C_t}{\alpha_t} \, dV. \end{aligned} \tag{5.20}$$

According to [28], the majority of the the pressure drop occurs between the compartments. Therefore, we assume the pressure within each compartment is constant which is shown to be well-approximated by their volume-averaged values [28]. Equation (5.20) then becomes

$$\begin{aligned} \int_{\Omega_{\mathrm{GM}}} \vec{u}_c \cdot \nabla C_c \, dV = \phi_c D_c \int_{\Omega_{\mathrm{GM}}} \nabla^2 C_c \, dV \\ + \beta_{ac}^{\mathrm{GM}} \left(\langle p_a \rangle^{\mathrm{GM}} - \langle p_c \rangle^{\mathrm{GM}} \right) C_a \int_{\Omega_{\mathrm{GM}}} 1 \, dV \\ - \beta_{cv}^{\mathrm{GM}} \left(\langle p_c \rangle^{\mathrm{GM}} - \langle p_v \rangle^{\mathrm{GM}} \right) \int_{\Omega_{\mathrm{GM}}} C_c \, dV \\ - \frac{\kappa_c}{h_c} \frac{S_c}{V_c} \phi_c \int_{\Omega_{\mathrm{GM}}} \frac{\tau C_c}{\alpha_b} - \frac{C_t}{\alpha_t} \, dV. \end{aligned} \tag{5.21}$$

As k_c in the term $\vec{u}_c = k_c \nabla p_c$ is very small, the value of the left hand term is of the order of 10^{-8} and is thus considered negligible for the rest of the derivation. Applying Gauss's theorem to the first term on the right hand side converts the volume integral into a surface integral, i.e.,

$$\phi_c D_c \int_{\Omega_{\mathrm{GM}}} \nabla^2 C_c \, dV = \phi_c D_c \int_{\partial\Omega_{\mathrm{GM}}} \nabla C_c \cdot \vec{n} \, dS. \tag{5.22}$$

In conjunction with the homogenous NBC prescribed to all surfaces of the capillary compartment, assuming $\nabla C_c = \vec{0}$ at the interface of grey and white matter for this derivation results in the elimination of Equation (5.22). This reduces Equation (5.21) to

$$\begin{aligned} 0 = {} & \beta_{ac}^{\mathrm{GM}} \left(\langle p_a \rangle^{\mathrm{GM}} - \langle p_c \rangle^{\mathrm{GM}} \right) C_a \int_{\Omega_{\mathrm{GM}}} 1 dV \\ & - \beta_{cv}^{\mathrm{GM}} \left(\langle p_c \rangle^{\mathrm{GM}} - \langle p_v \rangle^{\mathrm{GM}} \right) \int_{\Omega_{\mathrm{GM}}} C_c \, dV - \frac{\kappa_c}{h_c} \frac{S_c}{V_c} \phi_c \int_{\Omega_{\mathrm{GM}}} \frac{\tau C_c}{\alpha_b} - \frac{C_t}{\alpha_t} \, dV. \end{aligned} \tag{5.23}$$

Dividing by the grey matter volume gives the algebraic equation for the capillary compartment as

$$\begin{aligned} 0 = {} & \beta_{ac}^{\mathrm{GM}} \left(\langle p_a \rangle^{\mathrm{GM}} - \langle p_c \rangle^{\mathrm{GM}} \right) C_a - \beta_{cv}^{\mathrm{GM}} \left(\langle p_c \rangle^{\mathrm{GM}} - \langle p_v \rangle^{\mathrm{GM}} \right) \langle C_c \rangle^{\mathrm{GM}} \\ & - \frac{\kappa_c}{h_c} \frac{S_c}{V_c} \phi_c \left(\frac{\tau \langle C_c \rangle^{\mathrm{GM}}}{\alpha_b} - \frac{\langle C_t \rangle^{\mathrm{GM}}}{\alpha_t} \right). \end{aligned} \tag{5.24}$$

Similarly for the tissue compartment, integrating Equation (5.16b) over the grey matter domain, applying Gauss's theorem, and dividing V_{GM} results in the algebraic equation for the tissue compartment:

$$0 = \frac{\kappa_c}{h_c} \frac{S_c}{V_c} \phi_c \left(\frac{\tau \langle C_c \rangle^{\mathrm{GM}}}{\alpha_b} - \frac{\langle C_t \rangle^{\mathrm{GM}}}{\alpha_t} \right) - \phi_t G_{\max}^{\mathrm{GM}} \left\langle \frac{C_t}{C_{50} - C_t} \right\rangle^{\mathrm{GM}}. \tag{5.25}$$

The diffusion term disappears because of the homogenous NBC and the assumption that $\nabla C_t = \vec{0}$ at the interface of grey and white matter. Equations (5.24) and (5.25)

together form the algebraic equation set for the grey matter of the 2-compartment oxygen model. The equation set for the white matter can be derived in exactly the same way and the result reads

$$0 = \beta_{ac}^{\mathrm{WM}} \left(\langle p_a \rangle^{\mathrm{WM}} - \langle p_c \rangle^{\mathrm{WM}} \right) C_a - \beta_{cv}^{\mathrm{WM}} \left(\langle p_c \rangle^{\mathrm{WM}} - \langle p_v \rangle^{\mathrm{WM}} \right) \langle C_c \rangle^{\mathrm{WM}} - \frac{\kappa_c}{h_c} \frac{S_c}{V_c} \phi_c \left(\frac{\tau \langle C_c \rangle^{\mathrm{WM}}}{\alpha_b} - \frac{\langle C_t \rangle^{\mathrm{WM}}}{\alpha_t} \right); \tag{5.26a}$$

$$0 = \frac{\kappa_c}{h_c} \frac{S_c}{V_c} \phi_c \left(\frac{\tau \langle C_c \rangle^{\mathrm{WM}}}{\alpha_b} - \frac{\langle C_t \rangle^{\mathrm{WM}}}{\alpha_t} \right) - \phi_t G_{\max}^{\mathrm{WM}} \left\langle \frac{C_t}{C_{50} - C_t} \right\rangle^{\mathrm{WM}}. \tag{5.26b}$$

Given that the algebraic equations are the same for grey and white matter, the superscripts (GM and WM) are omitted in the rest of this section unless necessary.

The goal of the optimisation is to find the best $G_{\max}$ values for the grey and white matter while maintaining physiologically accurate oxygen level throughout the domain. The challenge of this optimisation lies in finding a suitable criterion to construct the cost function. Although physiological values of cerebral partial pressure of oxygen have been reported, they vary among literature and few values have been reported specifically for the white matter. Oxygen extraction fraction (OEF), on the other hand, not only is relatively consistent across literature (OEF$\in$[0.3, 0.48]) but is almost identical between the grey and white matter [77]. Experimentally, OEF is measured via PET [77, 107, 158, 159] or, in recent years, via MRI [108, 160, 161] and is defined as

$$\mathrm{OEF} = \frac{S_{O_2}^a - S_{O_2}^v}{S_{O_2}^a} \approx \frac{C_a - C_v}{C_a}, \tag{5.27}$$

where $S_{O_2}^v$ is oxygen saturation at the venule's outlet. However, the current oxygen model does not allow for the determination of the pial surface oxygen concentration of the venules due to the lack of venular compartment. To relate the algebraic equations of the oxygen model to the chosen optimisation criterion, we consider the relationship between OEF and $\mathrm{CMRO_2}$, i.e.,

$$\mathrm{CMRO_2} = \mathrm{OEF} \cdot F_{\mathrm{blood}} \cdot C_a. \tag{5.28}$$

Substituting the capillary equation into the tissue equation and rearranging the resultant equation lead to the following relationship

$$\phi_t G_{\max} \left\langle \frac{C_t}{C_{50} - C_t} \right\rangle = \beta_{ac} \left(\langle p_a \rangle - \langle p_c \rangle \right) C_a - \beta_{cv} \left(\langle p_c \rangle - \langle p_v \rangle \right) \langle C_c \rangle. \tag{5.29}$$

According to Equation (5.19), the volume-averaged inter-compartment advection coefficients can be replaced by $-Q_a/V$, which leads to

$$\underbrace{\phi_t G_{\max} \left\langle \frac{C_t}{C_{50} - C_t} \right\rangle}_{\mathrm{CMRO_2}} = \underbrace{-\frac{Q_a}{V}}_{F_{\mathrm{blood}}} \underbrace{\left(C_a - \langle C_c \rangle \right)}_{\mathrm{OEF} \cdot C_a}. \tag{5.30}$$

As indicated by the curly bracket under each term, the left hand side represents $\mathrm{CMRO_2}$ of the system and the first term on the right hand side is perfusion. As the venules are consider purely to be a sink in the oxygen model, we can assume that $\langle C_v \rangle = \langle C_c \rangle$. This means that the second term on the right hand side is equivalent to $\mathrm{OEF} \cdot C_a$ from a volume-averaged perspective. Equation (5.30) is then used to perform the optimisation.

A value of 0.4 [77] is chosen as the value of OEF for both the grey and the white matter. The optimisation problem hence becomes to find the best $G_{\max}$ values so that $\langle C_c \rangle = 0.6 C_a$ as inferred by Equation (5.30). Therefore, the cost function (J) to be minimised is

$$J = \left(\langle C_c \rangle - 0.6 C_a \right)^2 + J_{\mathrm{penalty}}, \tag{5.31}$$

where J_{penalty} is a step function and follows

$$J_{\mathrm{penalty}} = \begin{cases} \left(\langle \mathrm{CMRO_2} \rangle^{\mathrm{num}} - \min(\mathrm{CMRO_2^{lit}}) \right)^2, & \text{if } \langle \mathrm{CMRO_2} \rangle^{\mathrm{num}} < \min(\mathrm{CMRO_2^{lit}}); \\ \left(\langle \mathrm{CMRO_2} \rangle^{\mathrm{num}} - \max(\mathrm{CMRO_2^{lit}}) \right)^2, & \text{if } \langle \mathrm{CMRO_2} \rangle^{\mathrm{num}} > \max(\mathrm{CMRO_2^{lit}}); \\ 0, & \text{otherwise.} \end{cases} \tag{5.32}$$

$\langle \mathrm{CMRO_2} \rangle^{\mathrm{num}}$ is the volume averaged $\mathrm{CMRO_2}$ value computed by the oxygen model; $\mathrm{CMRO_2^{lit}}$ is the physiological values from the literature which is in the range of 5.04–

10.33×10^{-4} [$\mathrm{mm^3\,O_2/(mm^3\,tissue\cdot s)}$] [77, 99, 107, 147, 148, 158] and 2.05–4.73×10^{-4} [$\mathrm{mm^3\,O_2/(mm^3\,tissue\cdot s)}$] [77,99,107,147,148,158] for the grey and the white matter, respectively. The addition of the penalty term aims to restrict the metabolism of the numerical solution to be within the physiological range. Additionally, the bounding values of $G_{\max}$ are chosen to be the same as those for $\mathrm{CMRO_2}$. As mentioned in the previous chapter, this provides a very good approximation of $G_{\max}$ when $C_t \gg C_{50}$ which is the case under all healthy conditions.

The optimisation problem can now be phrased as

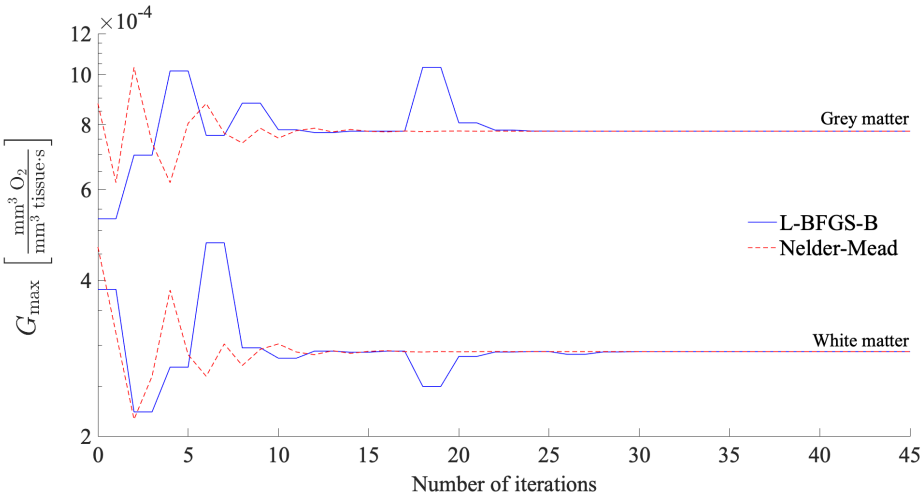
$$\min\left[J(G_{\max})\right] \quad \text{in} \quad G_{\max} \in [5.04 \times 10^{-4}, 10.33 \times 10^{-4}] \tag{5.33}$$

for grey matter and as

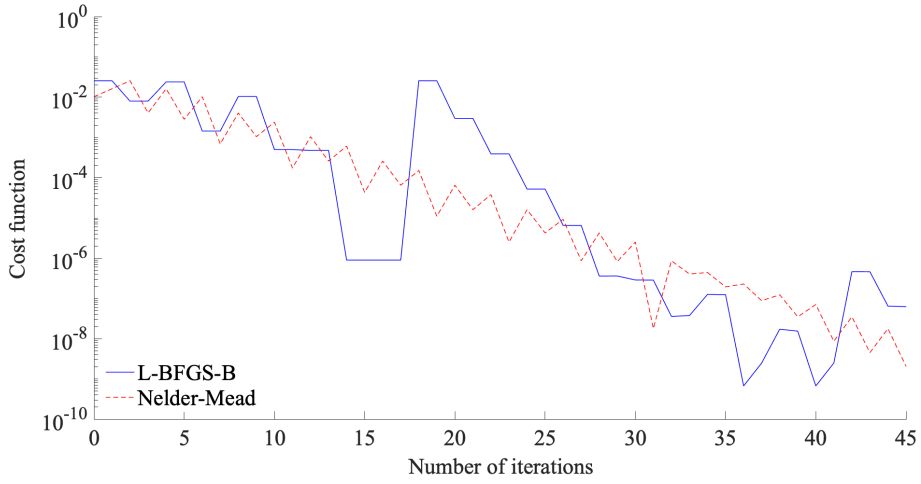
$$\min\left[J(G_{\max})\right] \quad \text{in} \quad G_{\max} \in [2.05 \times 10^{-4}, 4.73 \times 10^{-4}] \tag{5.34}$$

for white matter. Note that optimisation of $G_{\max}$ for grey and white matter can be performed independently because C_a does not vary spatially and no-flow is assumed at the grey-white matter interface. To find the global minimum of J, two optimisation methods (BFGS [162] and the Nelder-Mead [163]) are employed with the utilisation of Mathematica [156]. Both optimisation algorithms work with bounded optimisation; while BFGS is gradient based, Nelder-Mead does not require the computation of the cost function's gradient.

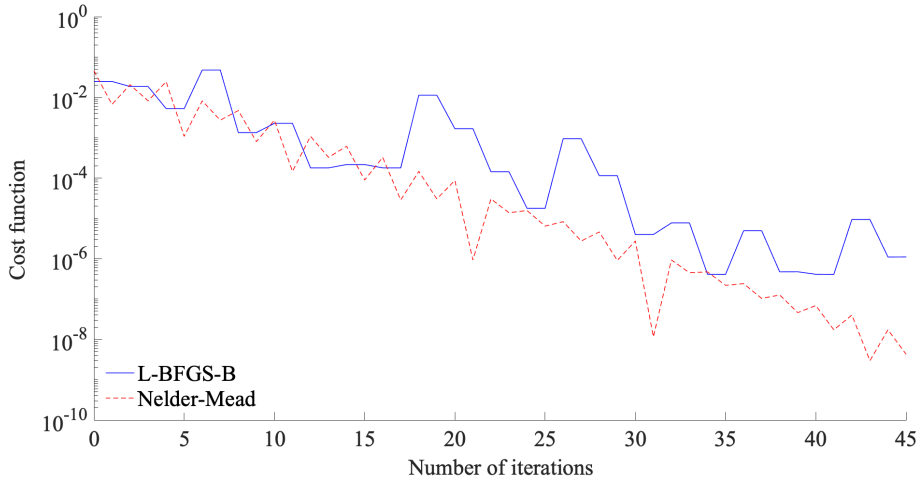
Both algorithms are run three times and each with an initial guess generated randomly within the bounds, which ensures that the optimised $G_{\max}$ is independent from the choice of algorithms and the initial values. All runs converge rapidly towards the same $G_{\max}$ values reaching $J < 10^{-4}$ in 30 iterations; convergence plots of $G_{\max}$ and J of the grey and white matter from a typical run are shown in Figure 5.10. The optimised parameter values are found to be $G_{\max}^{\mathrm{GM}} = 7.77 \times 10^{-4}$ and $G_{\max}^{\mathrm{WM}} = 2.91 \times 10^{-4}$ [$\mathrm{mm^3\,O_2/(mm^3\,tissue\cdot s)}$].



(a) $G_{\max}$



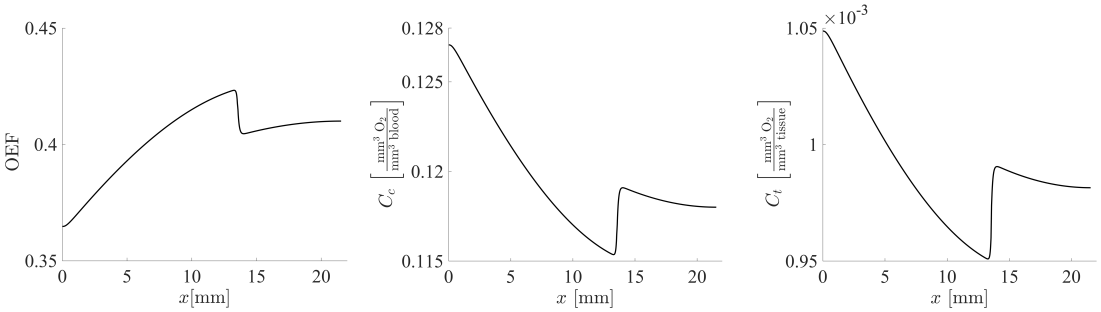
(b) Cost function for grey matter



(c) Cost function for white matter

Figure 5.10: Convergence plots of $G_{\max}$ and cost function (J) of the grey and white matter from a typical optimisation.

Figure 5.11 and Table 5.7 show the results of the 2-compartment oxygen model in a 1D tissue column with the optimised $G_{\max}$. Calculation of the OEF follows Equation (5.27) with the assumption that $C_c = C_v$ under steady state. It can be seen from Figure 5.11a that value of the OEF is maintained around the optimisation target with a less than 9% variation throughout the depth. The volume-averaged oxygen level agrees well with the physiological values. Additionally, volume-averaged values of $CMRO_2$ for both the entire domain and the subdomains sit within the physiological range.



(a) OEF (b) Capillary (c) Tissue

Figure 5.11: Simulation results of the 2-compartment oxygen model in a 1D tissue column with optimised metabolic rates.

	$\langle C \rangle$ $\left[\frac{\text{mm}^3\,\text{O}_2}{\text{mm}^3\,\text{blood(/tissue)}}\right]$	$\langle P_{O_2} \rangle$ [mmHg]	$\langle S_{O_2} \rangle$ [%]	$\langle \text{CMRO}_2 \rangle$ $\left[\frac{\text{mm}^3\,\text{O}_2}{\text{mm}^3\,\text{tissue}\cdot\text{s}}\right]$
Whole				
Capillary	1.20×10^{-1}	38.44	72.75	-
Tissue	9.89×10^{-4}	38.04	-	5.74×10^{-4}
Grey matter				
Capillary	1.20×10^{-1}	38.65	73.03	-
Tissue	9.91×10^{-4}	38.13	-	7.46×10^{-4}
White matter				
Capillary	1.18×10^{-1}	38.07	72.27	-
Tissue	9.85×10^{-4}	37.88	-	2.80×10^{-4}

Table 5.7: Volume averaged values of oxygen concentration, partial pressure, saturation, and $CMRO_2$ of the 2-compartment oxygen model in a 1D tissue column with optimised metabolic rates.

Although the increase in oxygen concentration at the grey-white matter interface seems counter-intuitive, an explanation from a numerical perspective is discussed in Section 5.3.2. Physiologically speaking, measurements regarding oxygen partial pressure versus depth of the brain are very scarce. As part of a study on assessing the reliability of catheter probes on monitoring brain tissue P_{O_2} [97], Dings *et al.* performed a stepwise removal of the probes from 27 patients (10 with subarachnoid haemorrhage and 17 with severe head injury). The probes were placed in normal-appearing tissue, as identified on CT images, and removed in 3 steps from a depth of 22–27 [mm] (white matter) to 7–12 [mm] with an increment of 5 [mm]. Over half (59%) of the measurements showed a higher $P^t_{O_2}$ at a position comparatively closer to the pial surface; however, 25.6% of all readings showed the opposite. It was not clear where the grey-white matter interface was and the lowest $P^t_{O_2}$ was measured not only in the 22–27 [mm] depth range.

On the other hand, animal experiments conducted by Feng *et al.* [164] showed that $P^t_{O_2}$ decreased with depth in the cortex and increased around the region of white matter. Differences of $P^t_{O_2}$ at 1000 [μm], 2000 [μm] and 3000 [μm] underwent statistical evaluation; meanwhile, histological test confirmed that these depths were located within grey matter, white matter and hippocampal grey matter. It was found that $P^t_{O_2}$ measured at 1000 [μm] was significantly lower than that at 2000 [μm]. Figure 5.12 shows the mean values of $P^t_{O_2}$ plotted against depth for closed and opened skull rats from the work of Feng *et al.* [164]. It can be seen that oxygen level obtained by the oxygen model with the optimised metabolic rate (Figure 5.11c) show a resemblance to the trend of $P^t_{O_2}$ from the rat experiment.

In addition to the studies above, Smith *et al.* measured $P^t_{O_2}$ in the cortex of rabbits [165]. They found that the mean $P^t_{O_2}$ only decreased slightly from the surface to a depth of 1000 [μm]. Fluctuation of the mean tissue oxygen level was 8 [mmHg] and neither the surface $P^t_{O_2}$ was the highest value nor was the deepest one the lowest. In another study with rats, Metzger and Heuber [166] showed a decrease in mean $P^t_{O_2}$ over four layers from the surface to a depth of 1500 [μm]; however, there was a

large overlap between the $P^t_{O_2}$ range of each layer.

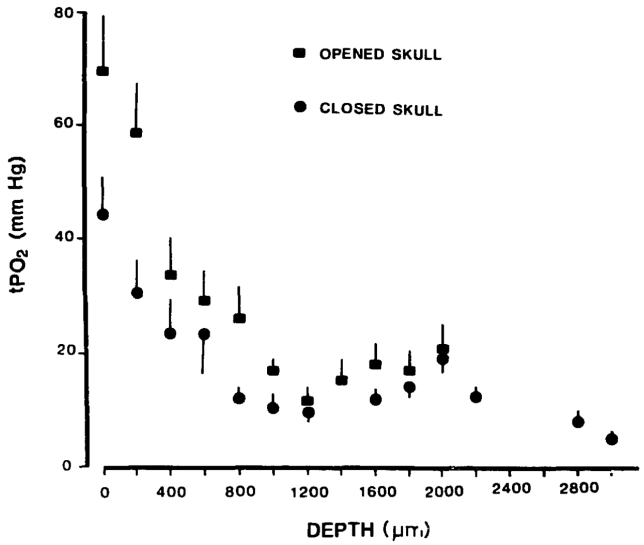


Figure 5.12: Mean values of $P^t_{O_2}$ vs depth for closed and opened skull rats. Reproduced without change from Feng *et al.* [164] under license CC BY-NC-ND 4.0 (https://creativecommons.org/licenses/by-nc-nd/4.0/).

Unfortunately, it is therefore not experimentally conclusive quite how oxygen is distributed through the depth of the brain. The optimisation result is proposed in the current work for the following reasons: the work of Feng *et al.* [164] supports the 1D numerical result; the chosen optimisation criterion, OEF, is consistent across literature and linked nicely to the algebraic equations of the model. Additionally, the change in oxygen concentration at the grey-white matter interface is best modelled as a sharp jump at this stage due to the lack of data. The optimisation result can be further improved once more data on the oxygen distribution in the brain becomes available.

5.5 Sensitivity analysis

A sensitivity analysis is next performed on the parameters that were obtained from literature to quantify the uncertainties of the values employed by the model. These parameters and their value range are listed in Table 5.8 and references for these values can be found in Table 4.1. Note that the choice of τ and its impact, as

mentioned before, will be discussed later in Section 7.2.2.

Parameter	Range	Unit
D_c	$1.57 - 1.65\times10^{-3}$	mm^2/s
D_t	$1.20 - 2.00\times10^{-3}$	mm^2/s
κ_c	$4.20 - 6.80\ \times10^{-8}$	$\mathrm{mm}^3\,\mathrm{O}_2/(\mathrm{mmHg}\cdot\mathrm{mm}\cdot\mathrm{s})$
h_c	$0.30 - 1\times10^{-3}$	mm
α_b	$2.86 - 3.11\times10^{-5}$	$\mathrm{mm}^3\,\mathrm{O}_2/(\mathrm{mm}^3\,\mathrm{blood}\cdot\mathrm{mmHg})$
α_t	$1.97 - 3.95\times10^{-5}$	$\mathrm{mm}^3\,\mathrm{O}_2/(\mathrm{mm}^3\,\mathrm{tissue}\cdot\mathrm{mmHg})$
$P_{C_{50}}$	$0.03 - 4$	mmHg

Table 5.8: Range of selected parameters for sensitivity analysis.

The sensitivity analysis is carried out on the 1D model and only one parameter is changed per simulation. Relative percentage change of oxygen concentration over the whole domain is used for the quantification, which is calculated as

$$\Delta C_i^{\mathrm{rel}} = \sqrt{\frac{\int_\Omega (C_i^{\mathrm{SA}} - C_i)^2\, dV}{\int_\Omega C_i^2\, dV}} \times 100\% \tag{5.35}$$

and C_i^{SA} represents the oxygen concentration of compartment i acquired with either the upper or lower bound of a chosen parameter; C_i is the oxygen concentration obtained with values listed in Table 5.2 and the optimised $G_{\max}$.

Result of $\Delta C_i^{\mathrm{rel}}$ for each parameter is summarised in Table 5.9. It can be seen that all parameters apart from $P_{C_{50}}$ have little effect on the capillary compartment, neither do D and κ_c on the tissue compartment. As shown in Table 5.8, the value of $P_{C_{50}}$ reported in the literature has a rather large range. Given that the upper bound of $P_{C_{50}}$ is four times the model value and the relative change between the oxygen concentration is less than 5%, the model is considered to be not sensitive to this parameter. Similarly for h_c, the model value is closer to the lower bound and less than 3% change in C_t is caused by a 2 times increase in its value.

Although $\alpha_b = 3 \times 10^{-5}$ $[\mathrm{O}_2/(\mathrm{mm}^3\,\mathrm{blood}\cdot\mathrm{mmHg})]$ is a common value found in textbooks [78, 167], $\Delta C_c^{\mathrm{rel}}$ and $\Delta C_t^{\mathrm{rel}}$ have values of 0.06% and 3.64%, respectively, which are considered small. Nonetheless, the tissue compartment is very sensitive

	ΔC_c^{rel} [%]		ΔC_t^{rel} [%]	
	Lower	Upper	Lower	Upper
D_c	4.17×10^{-4}	6.88×10^{-4}	4.20×10^{-4}	6.93×10^{-4}
D_t	7.85×10^{-3}	2.41×10^{-3}	8.12×10^{-3}	2.49×10^{-3}
κ_c	4.05×10^{-3}	5.61×10^{-3}	0.21	0.29
h_c	6.18×10^{-4}	4.81×10^{-2}	3.23×10^{-2}	2.47
α_b	0.14	-	8.68	-
α_t	5.60×10^{-3}	1.06×10^{-2}	24.23	51.92
$P_{C_{50}}$	1.72	4.55	1.76	4.67

Table 5.9: Relative percentage change of capillary and tissue concentration.

to the value of oxygen solubility; for every 1% relative change in the model value, there is about 1% relative change in the steady-state value of C_t. This is because that oxygen transport from the capillary to the tissue compartment is based on the P_{O_2} gradient and $P_{O_2}^t = C_t/\alpha_t$. However, Clark *et al.* [98] found that more than 50% of their measurements of α_t fell in the range of 2.37–2.89×10^{-5} [mm^3 $O_2/(\text{mm}^3\,\text{tissue}\cdot\text{mmHg})$], which reduces the upper and lower ΔC_t^{rel} to 11.15% and 8.84%, respectively. Since the current parameter value has also been employed in other simulation works involving oxygen transport [72, 99], it is kept unchanged while acknowledging its potential impact on the results.

5.6 Chapter review

The coupled flow-oxygen model developed in Chapter 3 was implemented using the FEM and the implementation was verified through the method of manufactured solutions. It was shown that linear FE scheme with a relatively fine mesh provided a good approximation with an acceptable computational cost. The 3-compartment model was solved first on a 1D tissue column. It was found that not enough oxygen was being delivered to the deeper layer of the brain, especially to the white matter, due to the comparatively large inter-compartment advection coefficients.

The model was thus reduced to 2 compartments with the assumption that there is no oxygen transport from arterioles to tissue. The maximum oxygen consumption

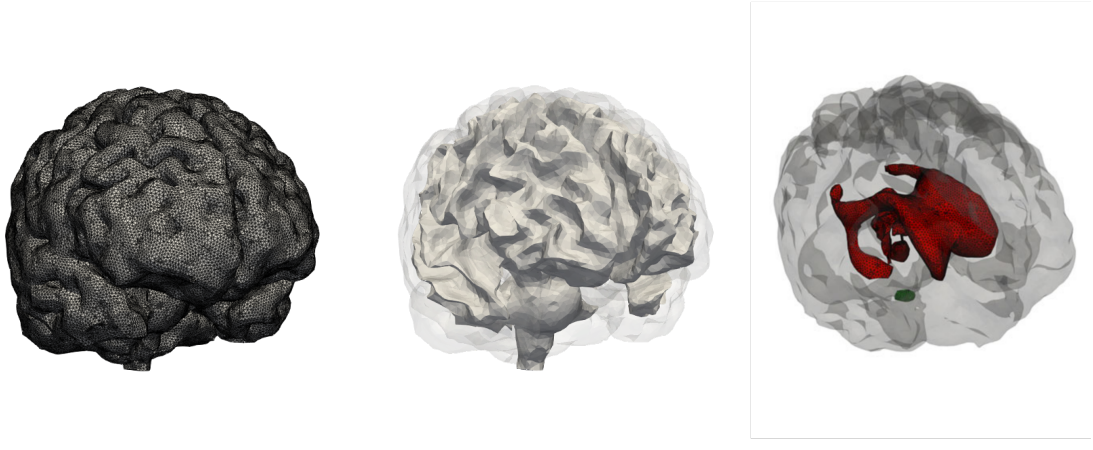
rate was then optimised for both the grey and white matters using volume-averaged governing equations. Finally a sensitivity analysis was performed. The model was found to be not sensitive to majority of the parameters; however, special attention should be paid to the values of oxygen solubility in tissue which have a bigger impact on the tissue compartment oxygenation. In the next chapter, the 2-compartment model (Equation (5.16)) will be implemented within a patient-specific brain mesh and oxygen transport under both healthy and stroke conditions will be investigated.

Chapter 6

Brain model

6.1 Introduction

In this chapter, the 2-compartment flow-oxygen model presented in Chapter 5 is implemented within a patient-specific human brain which has been used in several recent studies [28, 29, 168–170]. As illustrated in Figure 6.1, this brain geometry consists of the cerebrum, cerebellum and the brainstem. There are two volume regions — grey matter and white matter — bounded by an external surface and an internal surface that corresponds to the ventricles.



(a) (b) (c)

Figure 6.1: The brain mesh: (a) external boundary with mesh outline, (b) white matter and (c) ventricle surface (reproduced with permission from Józsa *et al.* [28]).

The mesh of the brain geometry adopted in the current work is the same as the

circulation model [28, 29], which has two physical subdomains ($\Omega = \Omega_{\mathrm{GM}} \cup \Omega_{\mathrm{WM}}$) and three bounding surfaces ($\partial\Omega$). One of the physical domain is the grey matter (Ω_{GM}) which includes the cerebral and cerebellum grey matters; the other one is the white matter (Ω_{WM}) which includes the cerebral and cerebellum white matters as well as the brainstem. The outer bounding surfaces are the pial surface[1] (Γ_P) and a transverse cut of the brainstem (Γ_{BS}) and the inner bounding surface that outlines the ventricles (Γ_V), i.e., $\partial\Omega = \Gamma_P \cup \Gamma_{\mathrm{BS}} \cup \Gamma_V$.

The baseline mesh contains 1,042,301 tetrahedral elements and this mesh will be used throughout this chapter. Section 6.2 reports results on healthy simulations of the oxygen model and a convergence study of the brain mesh. Section 6.3 introduces tissue level collateral into the model followed by simulation results on right middle cerebral artery (R-MCA) occlusion.

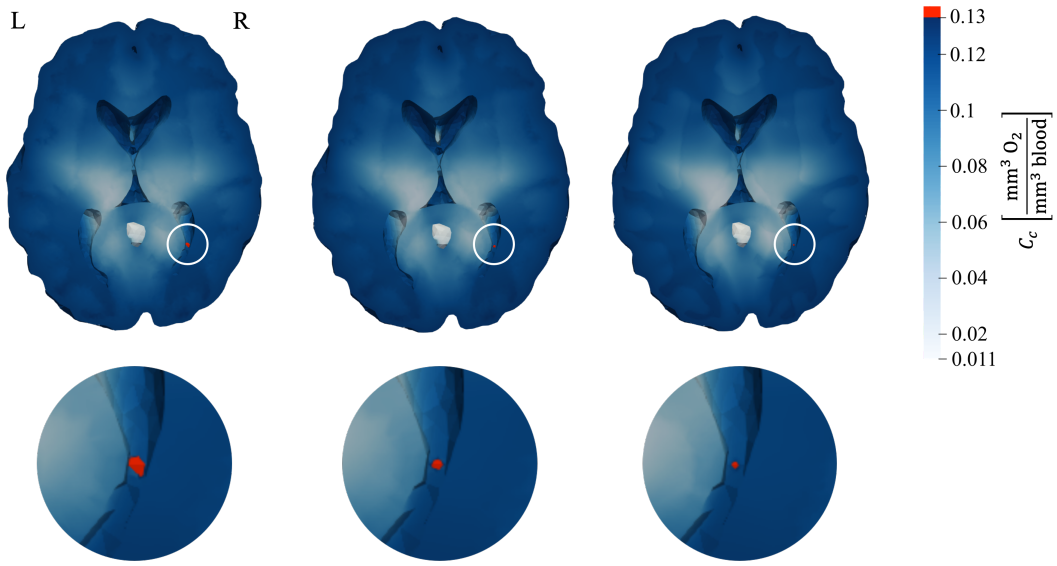
6.2 Simulations of the healthy case

Similar to the 1D model presented in the previous chapter, homogenous Neumann boundary condition (NBC) is imposed on the pial surface and the ventricles in both the capillary and the tissue compartments. Additionally, the same BC is imposed on the transverse cut of the brainstem. C_a is assigned a constant value of 0.2 [mm^3 O_2/mm^3 blood] for both the grey and white matter. Healthy simulations were performed on the baseline and refined meshes with first-order continuous Galerkin elements (c^1) for computing oxygen concentration. Both first- (p^1) and second-order (p^2) continuous Galerkin elements are used to calculate the Darcy pressure; zeroth-order discontinuous Galerkin elements (v^0) and first-order continuous Galerkin elements (v^1) are employed to evaluate the Darcy velocity.

Distributions of capillary oxygen concentration from the simulations using p^1 and v^0 with baseline, locally refined (loc. ref.), and uniformly refined (uni. ref.) meshes are presented in Figure 6.2. Note that the figures are displayed with an axial view from

[1]Pial surface here refers to the outer surface of the brain that is in contact with the CSF.

above; the left and right hemispheres are indicated as L and R, respectively. It can be seen in Figure 6.2a that there is instability at the right lateral ventricle (highlighted in red). The maximum value of C_c is 0.99 [mm^3 O_2/mm^3 blood] which is over 7 times larger than the highest C_c predicted by the 1D model. The distribution of C_t is similar to that of C_c with a value ranging between 8.11×10^{-5} and 1.11×10^{-3} [mm^3 O_2/mm^3 tissue] excluding the instability which is at the same location as that in the capillary compartment. As the FEM with the chosen element degrees is capable of giving sufficiently accurate approximations (see Section 5.2), the instability is likely caused by the poorly-shaped elements in the mesh.



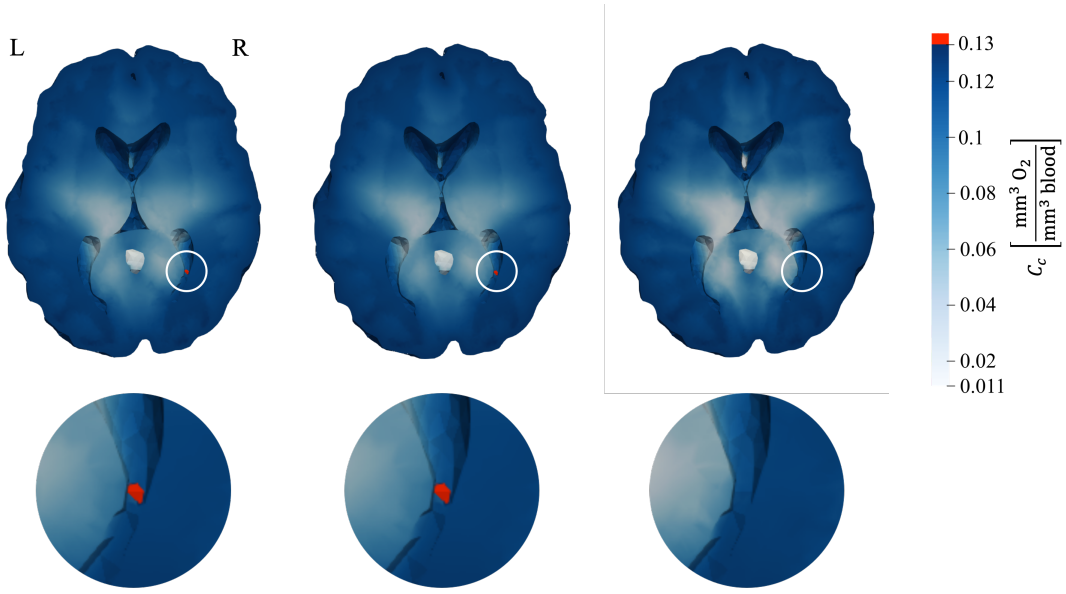
(a) Capillary, baseline (b) Capillary, loc. ref. (c) Capillary, uni. ref.

Figure 6.2: Healthy simulation results using first-order elements for pressure and discontinuous Galerkin elements for velocity with (a) baseline mesh, (b) locally refined mesh and (c) uniformly refined mesh.

The first strategy employed to resolve this instability was mesh refinement, both locally at the bounding surfaces and globally by doubling the element numbers uniformly. Although both the volume (V^c_{ins}) and magnitude (max C_c) of the instability are reduced (see Figures 6.2b and 6.2c and Table 6.1), it is not fully eliminated. It is possible that a finer mesh may remove the instability; however, this would not be computationally efficient given that the computation time using the uniformly

refined mesh is over 100 times longer than that of the baseline mesh.

The second strategy is to increase the element order for both the pressure and the velocity while maintaining the number of elements at baseline. Figure 6.3 and Table 6.1 show the simulation results. It can be seen that increasing the element order of velocity alone does not improve the simulation result; however, using second-order elements for pressure and first-order elements for velocity resolves the issue of instability. Józsa *et al.* [29] also showed that increasing the element orders of both the pressure and the velocity reduced the mass conservation error in the circulation model.



(a) Capillary, p^1v^0 (b) Capillary, p^1v^1 (c) Capillary, p^2v^1

Figure 6.3: Healthy simulation results using the baseline mesh with (a) p^1v^0 elements, (b) p^1v^1 elements and (c) p^2v^1 elements.

The healthy 3D model gives a volume-averaged oxygen concentration of 1.17×10^{-1} [mm^3 O_2/mm^3 blood] for the capillary compartment and 9.68×10^{-4} [mm^3 O_2/mm^3 tissue] for the tissue compartment. The volume-averaged oxygen concentration in both compartments are slightly lower than that of the 1D model with a <3% difference. This leads to a slightly higher volume-averaged oxygen extraction fraction with a value of 0.41. Similar to the flow model, this is because the chosen finite

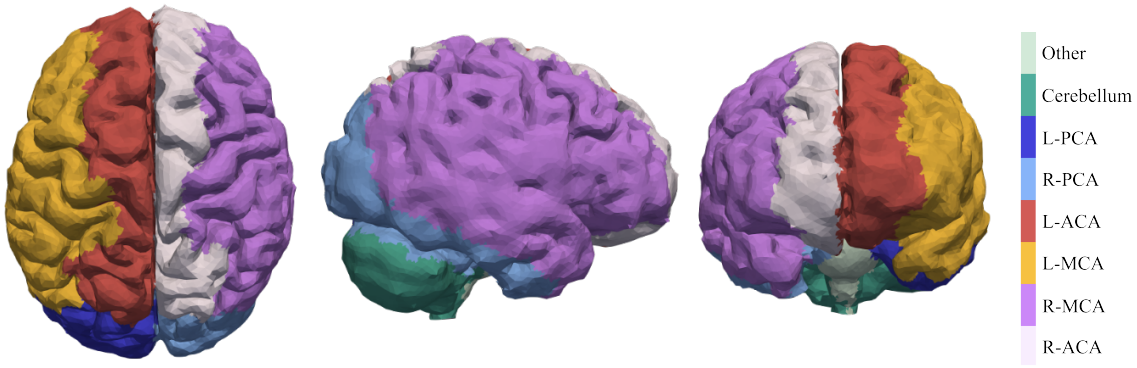
Mesh	n_{ele}	D^p_{ele}	D^v_{ele}	max C_c $\left[\frac{\text{mm}^3\,\text{O}_2}{\text{mm}^3\,\text{blood}}\right]$	V^c_{ins} [mL]	time* [min]
Baseline	1,042,301	1	0	0.9892	2.57×10^{-3}	1.773
Loc. ref.	3,400,579	1	0	0.3503	7.85×10^{-4}	114.4
Uni. ref.	8,338,408	1	0	0.1871	3.21×10^{-4}	238.6
Baseline	1,042,301	1	1	1.0150	2.57×10^{-3}	1.892
Baseline	1,042,301	2	1	0.1330	0	34.79

Table 6.1: Results for brain mesh convergence analysis. *These simulations were run on a high performance computer using 10 cores of an Intel Xeon Platinum 8268 processor with 80 GB RAM.

element method is not conservative. Reducing the element size will improve the result; however, it will also significantly increase the computational cost. Additionally, the smallest oxygen concentration is located around the ventricles and is much lower than that of the 1D model; this observation will be discussed in Section 7.2.2. Given the small difference between the volume-averaged results, the combination of p^2, v^1, and c^1 elements on a baseline mesh is thus used in the remainder of the chapter.

6.3 Stroke simulations

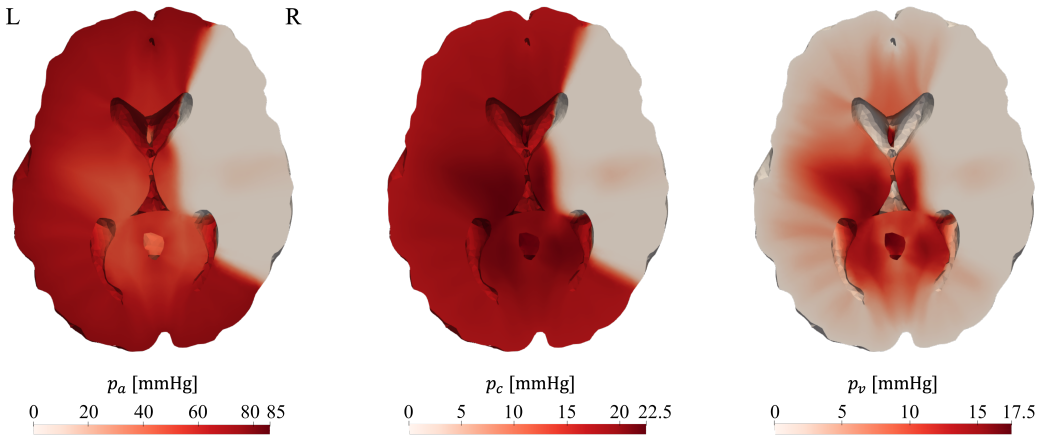
Middle cerebral artery occlusions constitutes over 70% of ischaemic strokes, of which the M1-segment accounts for over 60% [8, 171]. To use as a case study, a complete occlusion of the right middle cerebral artery (R-MCA) is simulated here using the 3D coupled flow-oxygen model. The final infarct volume estimates provided by the absolute and relative thresholds are then analysed. To achieve this, the pial surface (Γ_P) was divided into subdomains corresponding to the perfusion territories of the major feeding arteries, i.e., the left (L) and the right (R) anterior cerebral arteries (ACA), middle cerebral arteries (MCA) and posterior cerebral arteries (PCA) [28]. Figure 6.4 visualises the perfusion territories on the pial surface.



(a) (b) (c)

Figure 6.4: Projection of the perfusion territories of the large arteries on the pial surface: (a) axial view, (b) sagittal view and (c) coronal view. Regenerated based on Józsa *et al.* [28].

Mixed boundary conditions were enforced on Γ_P in the flow model — zero blood flow through the R-MCA territory and constant surface pressure elsewhere [28]. As oxygen is advected by blood flow, restricted flow leads to a limited transport of oxygen in the affected region. Therefore, no alteration is needed to the oxygen model. Although the FEM successfully solved the complete R-MCA occlusion for blood flow, the steep pressure gradient between the R-MCA territory and its surrounding non-affected regions (see Figure 6.5) made it challenging for the oxygen model to converge.



(a) Arteriole (b) Capillary (c) Venule

Figure 6.5: Pressure distribution post R-MCA occlusion: (a) arteriole, (b) capillary and (c) venule compartment.

The solution adopted to solve this issue is to enable blood flow rerouting through micro-scale vessels in the event of a major arterial occlusion. This would lead to an improved perfusion in the affected region. As these small vessel collaterals are embedded in the tissue, it is termed here tissue level collateral (TLC). The first option to consider was increasing the permeability of the capillary compartment (k_c); however, it was shown by Józsa *et al.* that perturbations in k_c have a weak impact on the perfusion result due to its high resistance to flow [29]. Instead, two additional values are added to the leading diagonal of the arteriole permeability tensors giving the following expression:

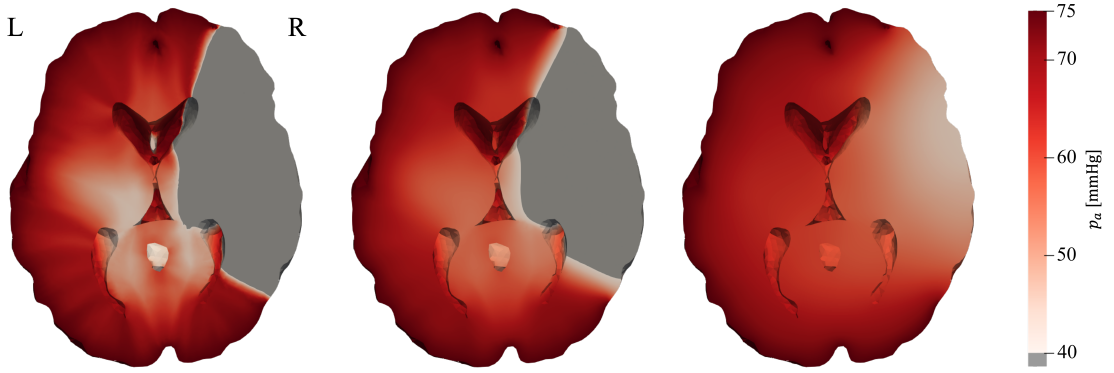
$$\overline{\overline{K}}_a^{ref} = \begin{bmatrix} k_{\mathrm{TLC}} & 0 & 0 \\ 0 & k_{\mathrm{TLC}} & 0 \\ 0 & 0 & k_a \end{bmatrix}, \tag{6.1}$$

where k_a is the permeability of the penetrating arterioles and k_{TLC} represents the macro-scale permeability of the arteriole-arteriole anastomosis bundles.

Information on anastomoses between arterioles is scarce. Through studies of Indian ink injected vascular corrosion casts, Duvernoy *et al.* observed that arterial anastomoses were always present and numerous in human brains [45]. Small diameter anastomoses joining two arterioles together were seen near the point of their penetration [45]. Reina-De La Rorre *et al.* also observed occasional connections between arterioles at their initial course after penetrating into the cortex [46]. In addition, Anderson and Anderson found anastomoses between adjacent arterioles at the pre-capillary level as well as along the arterioles of the horse and ox [172].

However, the aforementioned studies are only qualitative and arteriole-arteriole anastomoses were not part of the more recent quantitative analyses of the cerebral microvasculature. Due to the lack of statistics, a TLC index ($\gamma \in (0, 1]$) is introduced setting k_{TLC} to be a fraction of k_a, i.e., $k_{\mathrm{TLC}} = \gamma k_a$. Figure 6.6 shows the effect of γ on the arteriolar pressure. Note that the range of the colour map is

set to be the healthy arteriolar pressure result with no tissue level collateral effect. This range is chosen for a better visualisation of the results with different γ values. Regions where $p_a < 40$ [mmHg] are highlighted in grey[2]; the highest arteriolar pressure is above 75 [mmHg] for $\gamma = 0$.



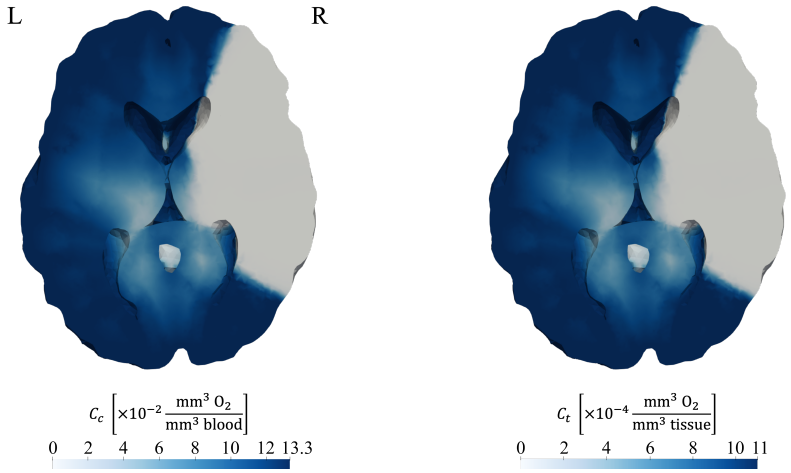
(a) $\gamma = 0$ (b) $\gamma = 0.1$ (c) $\gamma = 1$

Figure 6.6: Pressure distribution of the arteriole compartment post R-MCA occlusion with various TLC index.

It can be seen that as the tissue level collateral increases, the pressure field becomes more homogenous and the territory with high infarction risk is significantly reduced. More importantly, the pressure gradient between the R-MCA territory and the other regions has become less steep. Thirty one TLC indices, uniformly spaced on a logarithmic scale, are tested and the smallest possible γ for the oxygen model to converge is identified to be 0.004. Figure 6.7 shows the oxygen concentration distribution in the capillary and tissue compartment post R-MCA occlusion. Again, the upper limit on the colour map is set to be the corresponding healthy values (with tissue level collateral) for a better visualisation.

The maximum oxygen concentration of the capillary and tissue compartments are 0.1766 [mm^3 O_2/mm^3 blood] and 0.001472 [mm^3 O_2/mm^3 tissue], respectively. These are about 32% higher than their respective healthy maxima. However, for both compartments, less than 0.02% of the brain volume has a concentration value higher than 105% of their healthy maxima and these values are located around the

[2]Note that the grey areas here do not represent the actual infarct regions which are calculated based on the relative change in perfusion.



(a) Capillary (b) Tissue

Figure 6.7: Oxygen concentration distribution post R-MCA occlusion with $\gamma = 0.004$: (a) capillary and (b) tissue compartment.

infarct boundary. It is observed in Figure 6.7 that numerical instability is present at the interface of R-MCA territory and its surrounding regions, which is thought to be the reason behind the resultant high concentration. Additionally, this instability also caused a few elements in the infarct region to have a concentration value slightly smaller than 0 [mm^3 O_2/mm^3 blood (/tissue)] in both compartments. As the analysis of the results will be focused on infarct volume, the overestimation of oxygen concentration at the infarct boundary and the pial surface does not have a big impact on the results.

Because the inclusion of tissue level collateral alters the simulation result, its effect under healthy condition is first examined here. Adding tissue level collateral leads to an increase in oxygen concentration; however, such increases are found to be very small. With $\gamma = 0.004$, both volume-averaged C_c and C_t only increased by less than 0.1%, and with $\gamma = 1$, the increase in volume-averaged concentrations is under 2%. Although the addition of tissue level collateral alters the results of the oxygen model, re-optimisation of the maximum consumption rate of oxygen ($G_{\max}$) is not necessary given the small difference in the volume-averaged oxygen concentrations.

The extend of tissue damage caused by ischaemic stroke depends on the location,

severity and duration [5]. Tissue at the ischaemic core experiences irreversible damage within minutes of stroke onset, and the penumbra will progress to infarction if no reperfusion is provided. The simulation here represent the worst-case scenarios for virtual patients without treatment; therefore, the infarct lesion resulting from the complete R-MCA occlusion simulation includes both the initial ischaemic core and the penumbra turned infarction. Two thresholds of $P^t_{O_2}$ are used here to distinguish healthy and infracted tissue.

The first one is an absolute threshold. However, the exact level of $P^t_{O_2}$ below which cerebral tissue becomes hypoxic is unknown [173], and a wide range of values from 1 to 20 [mmHg] are used in the literature [31,119,174–179]. For this study, the smallest $P^t_{O_2}$ under healthy condition is chosen as the absolute threshold. It is worth noting that the value of the threshold varies as the TLC index changes with the lowest being 3.70 [mmHg] at $\gamma = 0.004$ and the highest being 17.18 [mmHg] at $\gamma = 1$. This is because tissue level collateral assists in blood flow distribution which leads to a more homogenous distribution of oxygen in the tissue, resulting in a higher minimum $P^t_{O_2}$ level with a larger TLC index.

The second threshold is the relative change of tissue oxygenation ($\Delta_r P^t_{O_2}$), which is defined as

$$\Delta_r P^t_{O_2} = 100\% \left(\frac{P^t_{O_2}(\text{occluded}) - P^t_{O_2}(\text{healthy})}{P^t_{O_2}(\text{healthy})} \right). \tag{6.2}$$

A value of 0% indicates no change in tissue oxygenation; whereas -100% means a complete depletion of oxygen in a region. A decrease in $P^t_{O_2}$ of more than 70% is chosen as the relative threshold. This is in line with the perfusion change threshold [180, 181] used by Józsa *et al.* [28] and allows a direct comparison of the infarct volume predicted by the oxygen model and the flow model.

Qualitative comparison between the oxygen results with $\gamma = 0.004$ (Figures 6.8d–6.8i) and non-contrast computed tomography (CT) scan images of a 76-year-old patient [28] (Figures 6.8a–6.8c) is presented first. This patient suffered from a proximal occlusion of the right MCA (M1-segment) and poor collaterals in the affected

hemisphere. Thrombectomy was carried out about 5 hours after stroke onset, which resulted in poor recanalisation and modified thrombolysis. Therefore, it is reasonable to assume that the lesion shown in the follow-up CT images correlate well with the initial infarct region and representing the worst-case scenario.

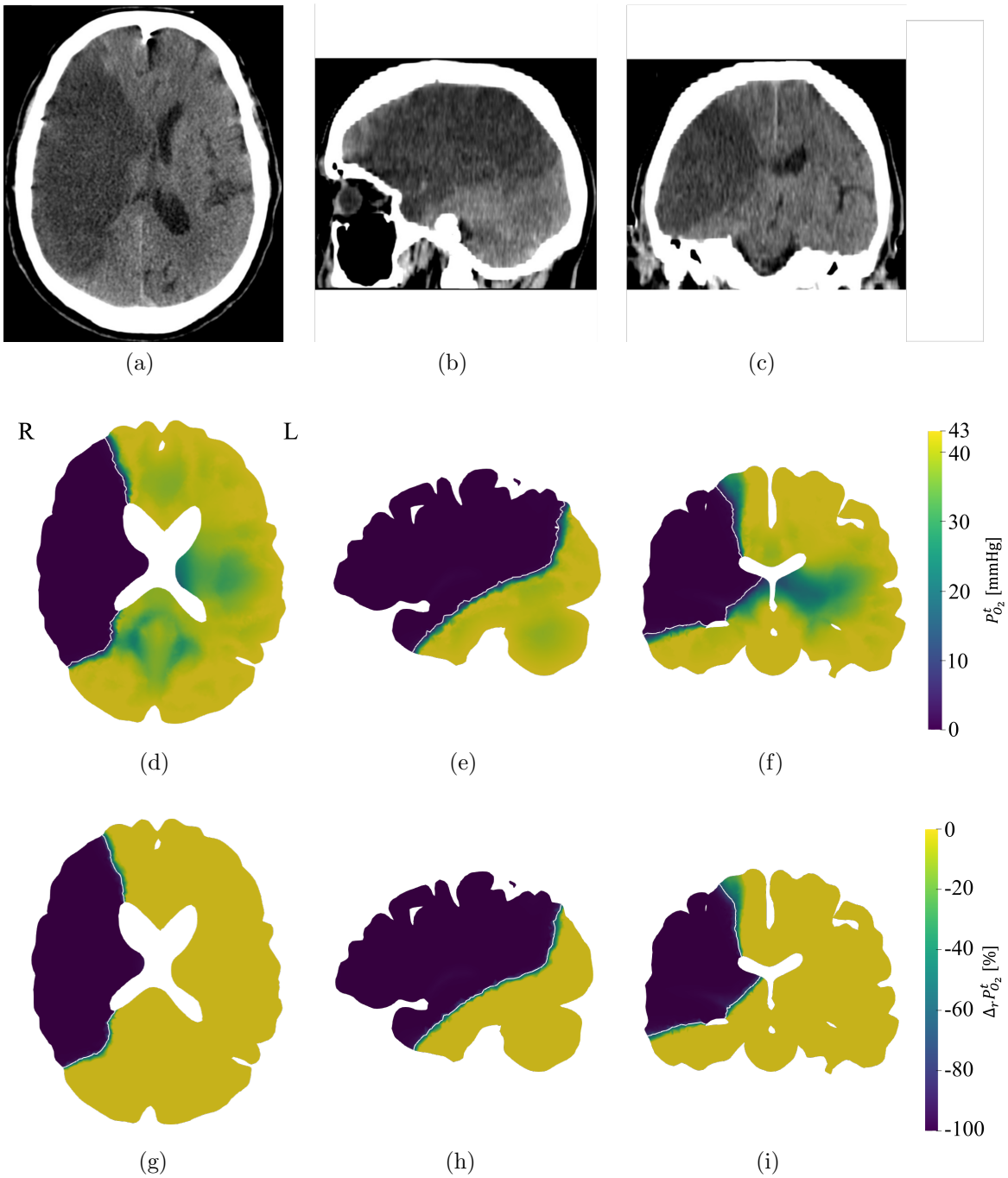


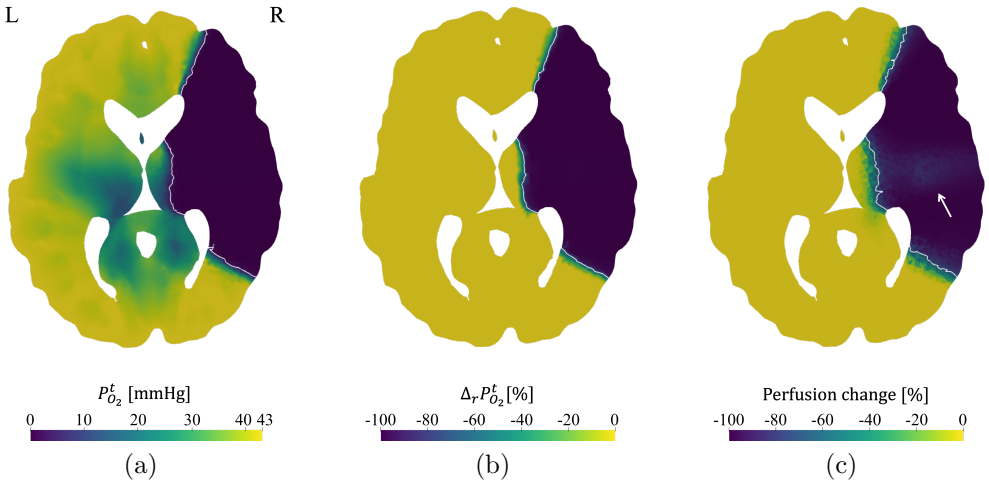
Figure 6.8: Qualitative comparison between (a–c) non-contrast CT images of a patient suffered from R-MCA occlusion (reproduced with permission from Józsa *et al.* [28]) and (d–i) the oxygen simulation results with $\gamma = 0.004$. The white isolines represent (d–f) an absolute threshold of $P^t_{O_2} = 3.70$ [mmHg] and (g–i) a relative threshold of -70% change in tissue oxygen.

Axial, sagittal, and coronal planes of the oxygen model are chosen at a similar location as the CT images. Figures 6.8d–6.8f show the simulated tissue oxygen partial pressure distribution post-stroke and the white isoline indicates the absolute threshold of $P^t_{O_2} = 3.70$ [mmHg]. Figures 6.8g–6.8i present the results post-processed according to Equation (6.2) and the relative threshold of -70% is highlighted by the white isoline. It can be seen that both thresholds predict a very similar infarct region with the absolute threshold giving a slightly smaller lesion. Both results compare well with the hypodense area on the CT images.

Figure 6.9 shows oxygen results alongside the flow result which is also simulated with $\gamma = 0.004$. As mentioned before, the flow model predicts the infarct volume based on a relative perfusion threshold of -70% [28] which is highlighted by the white isoline in Figure 6.9c. Within the predicted infarct region, the distributions of both $P^t_{O_2}$ and $\Delta_r P^t_{O_2}$ are relatively homogenous although it can be seen that a band of tissue (pointed by arrow) is not completely depleted of blood flow. A possible explanation for this difference could be that, unlike blood whose path is confined by the vessels, oxygen can diffuse relatively freely in tissue. It is likely that oxygen diffuses down the partial pressure gradient within the infarct region and is then metabolised, resulting in a more homogenised distribution. This behaviour can also be seen at the boundaries of the infarct region — each segment of the isoline in Figure 6.9b is smoother than that in Figure 6.9c.

Table 6.2 lists the infarct volume estimated according to each threshold. The predictions for all three are of the same magnitude and the absolute threshold gives the smallest infarct size. Comparing the results based on the relative threshold, relative change in tissue oxygenation predicts a higher infarct volume than perfusion change. This is also likely due to the effect of oxygen diffusion and metabolism near the infarct boundary. Additionally, the infarct volume computed by the oxygen model based on the relative oxygen threshold is relatively insensitive to the choice of the threshold value. Altering $\Delta_r P^t_{O_2}$ by $\pm 5\%$ gives to a change of $\pm 1\%$ in the infarct volume. On the other hand, the perfusion estimation is more sensitive to the choice

of relative threshold; the estimated infarct size changed by −2.6% and +2.2% with the relative perfusion threshold being −75% and −65%, respectively.



(a) (b) (c)

Figure 6.9: Side-by-side comparison between the oxygen lesion based on (a) absolute and (b) relative threshold and (c) the perfusion lesion post R-MCA occlusion with $\gamma = 0.004$.

	Absolute $P^t_{O_2}$	$\Delta_r P^t_{O_2}$	Perfusion change
Infarct volume [mL]	261.33	274.65	264.49

Table 6.2: Infarct volume estimated by the coupled flow-oxygen model and the perfusion model with $\gamma = 0.004$.

The infarct size estimated by both the oxygen and flow model are at the higher end of infarct volumes measured in acute ischaemic stroke patients. Pereira *et al.* identified an average (mean ± SD) infarct volume of 105 ± 112 [mL][3] and 134 ± 93 [mL] within 72 hours of MCA stroke onset in patients who had a poor outcome at 3 months [182]. Boers *et al.* measured 138 ± 106 [mL] in 34 patients of whom the majority had a MCA occlusion [183]. The larger-than-average infarct volume predicted by the model is partially due to the complete blockage of the right MCA in the simulations. Even though the results in Table 6.2 include some degree of tissue level collateral, this is relatively small and other compensatory mechanisms,

[3]Note that there is no negative values in the data set. The data set is, however, skewed resulting the standard deviation being larger than the mean.

such as collateral flow associated with the pial arteries [184, 185], are not included in the current model.

On the other hand, malignant MCA infarction[4] results in a much larger lesion. From the data Kamran *et al.* [187] used to perform infarct growth predictions, all patients had undergone at least 3 CT scans before decompressive hemicraniectomy. Patients with only MCA occlusions that had the 3rd CT scan within 72 hours had an infarct volume of 319 $\pm$ 93 [mL] [187]. The reason for the model's underestimation could be the lack of mechanical consequences due to cerebral oedema which can be seen in Figures 6.8a and 6.8c where the right ventricles are compressed. This patient had a infarct volume of 309 [mL].

Although the addition of tissue level collateral has little impact on the volume-averaged oxygen content under healthy conditions, the minimal tissue oxygen partial pressure increases as the TLC index becomes larger (Figures 6.10a–6.10d), improving the oxygenation around the ventricles. Similar to the arteriolar pressure field, the oxygen distribution becomes more homogenous as the index value increases. The effect of the TLC index on the oxygen predicted lesion is also shown in Figure 6.10 for selected values of γ. The white isolines represent the absolute and relative thresholds in Figures 6.10e–6.10h and Figures 6.10i–6.10l, respectively.

It can be seen that the lesion size estimated based on tissue oxygenation reduces significantly as γ gets closer to 1 at which, according to the chosen thresholds, no lesion is present. The larger index values, hence greater permeabilities, allow more blood to travel between the penetrating arterioles, so more oxygen is transported into the occluded MCA territory from its surrounding regions. This can be observed in Figures 6.10g and 6.10k as the gradual gradient between the infarct region and its neighbouring territories. Although the results predicts no infarct with $\gamma = 1$, it is not enough to fully recover the tissue within the R-MCA territory to its healthy state (Figures 6.10h and 6.10l). Despite $\gamma = 1$ being an extreme case where the

[4]Malignant MCA infarction is characterised by the rapid decline of neuronal function caused by the formation of space occupying oedema [186].

anastomoses between arterioles have the same permeability as the penetrating arteriolar bundles, the results from studying the full TLC range indicate that they could contribute significantly to the physiological variability seen in stroke patients.

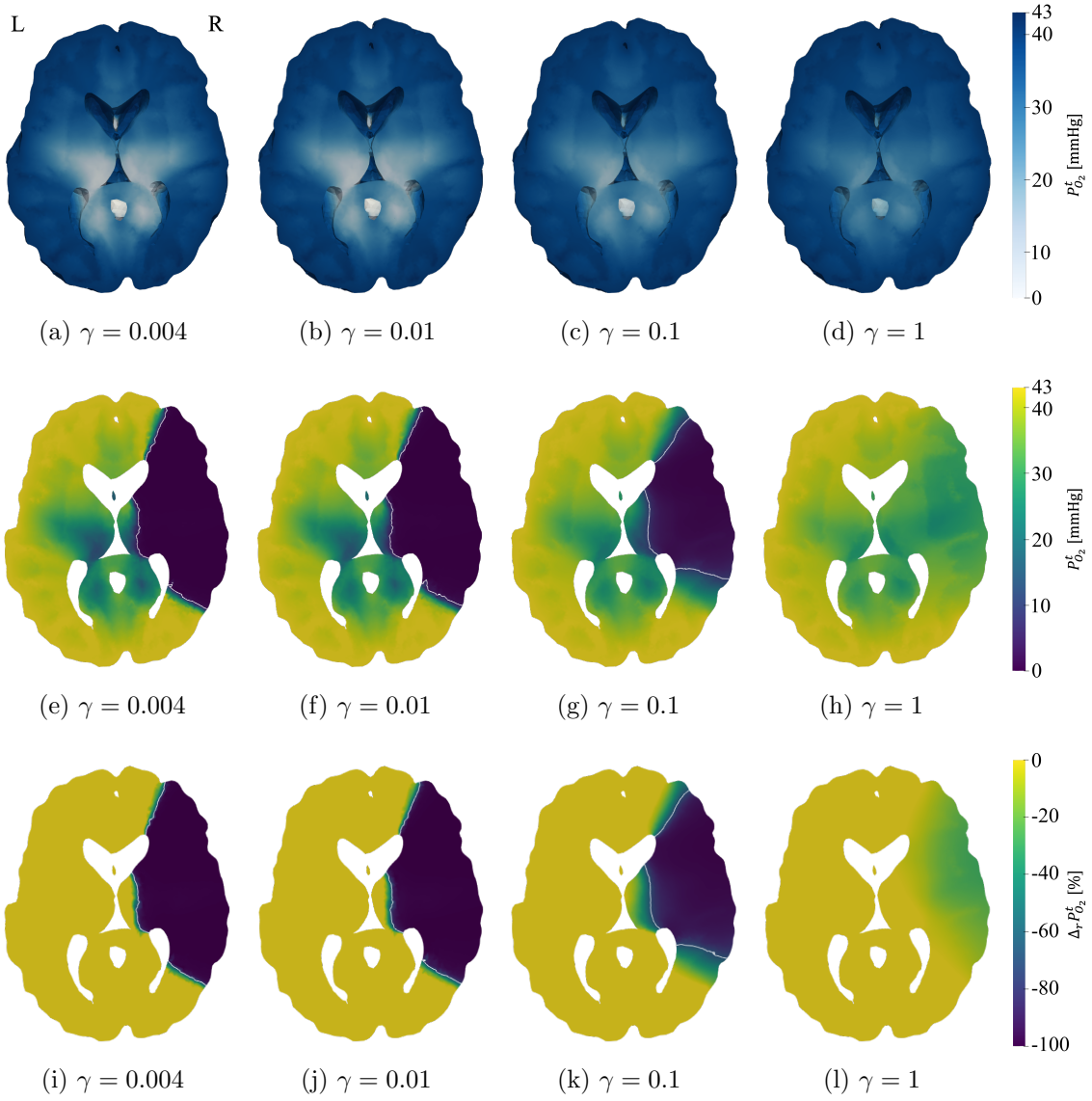
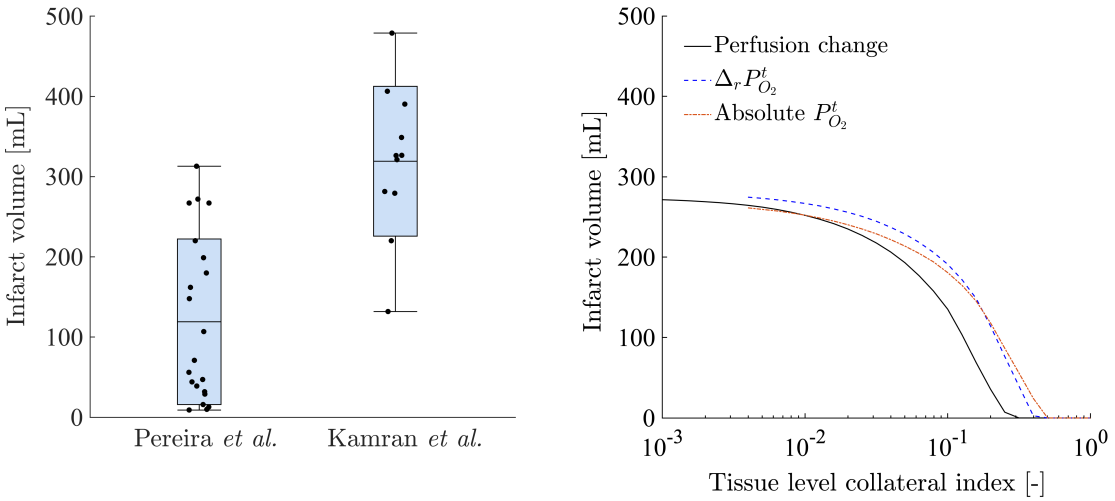


Figure 6.10: Distribution of partial pressure of tissue oxygen with various tissue level collateral under (a–d) healthy condition and (e–h) R-MCA occlusion. (i–l) show the change in tissue oxygenation post R-MCA occlusion with various tissue level collateral. The white iso-lines represent (e–h) absolute and (i–l) relative threshold.

The simulated infarct volumes are quantified and plotted against the TLC indices in Figure 6.11b along side two sets of reference data extracted from Pereira *et al.* [182] and Kamran *et al.* [187] (Figure 6.11a). Pereira *et al.* used T2-weighted MR images to identify the initial infarct size in patients with MCA occlusion [182]. Only patients

with poor outcomes (dependent or dead) at 3 months are included in this comparison which gives an averaged infarct volume of 119 ± 103 [mL]. As mentioned before, Karman *et al.* used data from CT scans [187] and patients who had only MCA occlusion with their 3rd CT scan within 72 hours are selected for this comparison. These patients had an averaged infarct volume of 319 ± 93 [mL].



(a) Reference data (b) Simulation results

Figure 6.11: Comparison between (a) two sets of reference infarct volumes extracted from Pereira *et al.* [182] and Kamran *et al.* [187] and (b) simulated infarct volumes with various tissue level collateral.

As shown in Figure 6.11a, the reference data has a high variability in infarct volume within each study as well as across the two studies. One of the reasons for the rather high inter-study variability could be due to the difference in stroke severity; all patients in the study of Kamran *et al.* were subjected to decompressive hemicraniectom indicating a high intracranial pressure as a result of space occupying oedema and mass effects. Additionally, the difference in imaging methods and lesion segmentation techniques could also leads to variabilities in the identified lesion size.

Although the current coupled flow-oxygen model could not estimate the very large lesions, the inclusion of tissue level collateral does cover the lower range. According to Figure 6.11b, infarct volumes predicted based on the change in tissue oxygena-

tion are consistently larger than those estimated by perfusion change. Lesion size calculated based on the absolute threshold is the smallest until $\gamma = 0.01$ and later becomes the largest when $\gamma = 0.2$. This variation is because the absolute threshold changes with γ.

Based on Figure 6.11b, all criteria predicted zero infarct volume with $\gamma = 0.5$ where macro-scale permeability of the arteriolar-arteriolar anastomosis is half of that of the penetrating arterioles. At $\gamma = 0.2$, the oxygen model predicts an infarct volume roughly the same as the mean value from the study of Pereira *et al.* [182]. As the cerebral collateral status is usually accessed clinically by comparing the leptomeningeal anastomoses in the ischaemic hemisphere to that on the contralateral side via CT angiography [184], it is hard to relate the simulation findings to clinical scores.

Recently, the term tissue level collaterals has been used to describe cerebral collaterals assessed by CT or MR perfusion imaging [188,189]. This clinical TLC is determined by the hypoperfusion intensity ratio (HIR)[5] [190, 191] which directly reflects the tissue perfusion status and has been associated with favourable outcomes regardless of collateral status assessed by the single-phase CT angiography [188, 192]. Although both the clinical TLC and the one employed in the model account for microvessel collaterals, the former also includes the contribution from the major collateral routes. A direct comparison, at this stage, is not possible; however, coupling the flow-oxygen model with a leptomeningeal collateral circulation model [27] could enable this.

6.4 Chapter review

The coupled flow-oxygen model was implemented within a patient-specific brain mesh and healthy simulations were carried out first. Numerical instability caused

[5]HIR is calculated as the ischaemic tissue volume with a T_{max} delay of >10s over the brain tissue volume with a T_{max} delay of >6s. A low HIR, therefore, indicates a good collateral, which has a threshold of ≤0.4 [190, 191].

by poorly-shaped elements was found at the ventricles, which was resolved by using second-order and first-order elements for calculating pressure and velocity, respectively. The volume-averaged oxygen concentration in both the capillary and tissue compartments were comparable to that found in the 1D tissue column.

A complete R-MCA occlusion was then simulated; however, the oxygen model could not converge due to the steep pressure gradient between the affected region and its surrounding territories. To solve this issue, the concept of tissue level collateral was introduced; this led to a more homogenous distribution of blood and oxygen in the brain. A range of TLC indices was tested and the smallest possible TLC index for the oxygen model to converge was identified.

Absolute and relative $P^t_{O_2}$ thresholds were chosen to identify the simulated infarct region and estimate the infarct volume. The oxygen predicted lesion appeared to be more homogenous and has a larger volume than the one estimated by perfusion alone, possibly due to the effect of oxygen diffusion and metabolism in the tissue. The simulation results showed good qualitative agreement with CT images of a patient who suffered from a R-MCA stroke. The effect of tissue level collateral on infarct size was then quantified. Although the oxygen model could not estimate the very large lesions as the results of malignant MCA infarction, it was able to cover the lower range of infarct volumes reported in the literature.

Chapter 7

Discussion and conclusion

7.1 Result summary and discussion

The aim of this thesis is to develop a multi-scale oxygen transport model of the human brain that captures the response of oxygen distribution to large vessel occlusions. The derivation of this model is presented in Chapter 3. The relevant oxygen transport compartments under the cortical surface were first identified to be arteriole, capillary, venule and tissue. Because of the coupled nature between the blood flow and oxygen transport, the oxygen model was coupled to an established perfusion model [28, 29]. Assumptions were introduced to restrict transport of oxygen from the arterioles to venules and from venules to tissue, which reduced the venule compartment to be an oxygen sink. This 3-compartment coupled flow-oxygen model was derived directly from mass conservation on the macro-scale with geometric parameters (volume fraction ϕ and vessels surface area to blood volume ratio S/V) that captures the micro-scale heterogeneities.

In Chapter 4, the effective values of the model parameters were identified. The representative elementary volume (REV) was employed to determine the effective geometric parameters. For the capillary compartment, statistically accurate capillary cubes generated in [68] were used. The size of the capillary beds ranged from 180 μm to 625 μm. While the best-fit curve of ϕ was found to converge to an effective

value, that of S/V did not reach convergence. However, 625 μm remained as the largest cube size due to high computational costs associated with larger networks. The effective values of ϕ and S/V both compared well with that obtained based on physiologically accurate networks. Choosing an error tolerance of 4.5%, a REV size of 375 μm was identified based on oxygen parameters, which is in agreement with the permeability based REV size [68].

For the arteriolar compartment, new penetrating arteriolar trees with a trunk diameter of 25 $\pm$ 5 μm were generated using the algorithms developed in [123]. The baseline voxel size of the penetration trees was allowed to vary linearly with the radius of the trunk diameter. As the penetrating trees were generated individually, larger voxel sizes were achieved by assembling randomly selected individual trees. Both ϕ and S/V of the arteriolar compartment converged rapidly to an effective value and compared well with values found in the literature. The size of the arteriolar REV was calculated to be 0.61 mm^3 which is slightly over 10 times larger than the capillary REV (0.052 mm^3) but smaller than a typical imaging voxel. Additionally, the rest of the parameters were either obtained from literature or computed from the perfusion model.

Chapter 5 deals with the numerical implementation of the coupled flow-oxygen model. The finite element method (FEM) was chosen to implement the model and a periodic cube was employed for verification using the method of manufactured solutions. First-order elements and discontinuous Galerkin elements were used for computing the Darcy pressure and velocity, respectively. Element order used for calculating the oxygen concentration was varied between 1 and 2. It was shown that linear FE scheme with a relatively fine mesh was able to provide a good approximation with an acceptable computational cost.

The 3-compartment oxygen model was then implemented on a one-dimensional (1D) tissue column. It was found that not enough oxygen was being delivered to the deeper layer of the brain, especially to the white matter, even when there was no oxy-

gen consumption. This was because of the comparatively large inter-compartment advection coefficients. With the only source of oxygen was at the pial surface, only less than half of the oxygen at any given depth was being transported deeper into the brain. This issue was resolved by assuming that there was no oxygen transport from arterioles to tissue, reducing the model to 2 compartments.

With the 2-compartment oxygen model, it was found that different maximum oxygen consumption rates led to different oxygen distributions over the depth of the brain. To uniquely define the oxygen distribution, the maximum consumption rate of oxygen was optimised using volume-averaged governing equations. Although the resultant oxygen distribution seemed counter-intuitive, showing an increase of oxygen level at the grey matter and white matter interface, it showed a resemblance to the trend of the partial pressure of oxygen measured in rats [164].

Finally, a sensitivity analysis was performed to quantify the parameter uncertainties. It was shown that the oxygen model was not sensitive to most of its parameters. However, the tissue compartment was very sensitive to the tissue oxygen solubility (α_t). It was found that every 1% relative change in α_t altered the tissue oxygen concentration by 1%. However, the original parameter value was kept unchanged as it had been used in other simulation works involving oxygen transport.

In Chapter 6, both healthy and stroke simulations were performed using a patient-specific brain mesh. Using a baseline mesh with the original set of element orders, numerical instabilities caused by poorly-shaped elements were found at the ventricles. A convergence test was then performed and using the baseline mesh with second-order elements for pressure and first-order elements for both velocity and oxygen concentration was able to eliminate the instabilities. The volume-averaged oxygen concentrations computed from 3D brain mesh were comparable to that of the 1D tissue column.

A complete right middle cerebral artery (R-MCA) occlusion was then simulated using the above setup. However, the coupled flow-oxygen model could not converge

because of the steep pressure gradient around the occluded region. The concept of tissue level collateral was introduced to aid the convergence. Two additional permeability values were added to the leading diagonal of the arteriolar permeability tensor representing arteriolar-arteriolar anastomoses. These values were set to be a fraction (TLC index) of the original arteriolar permeability and a range of TLC indices was tested. The smallest possible TLC index that allowed the oxygen model to converge was found to be 0.004.

The simulated infarct volume was then estimated based on absolute and relative oxygen partial pressure thresholds. The lesion estimated by the oxygen model appeared to be more homogenous and had a larger volume compared to the one estimated by perfusion alone. The effects of oxygen diffusion and metabolism in the tissue may explain this difference. The simulation results were then validated against CT images of a patient who suffered from a R-MCA stroke. The infarct region estimated by both thresholds showed good qualitative agreement with the imaging data. The influence of tissue level collateral on infarct size was then quantified. It was shown that the oxygen model could not estimate the very large lesions found in the literature due to the lack of considerations on mechanical consequences, such as oedema. With the addition of tissue level collateral, the model was able to estimate the lower range of the reported infarct volumes.

7.2 Limitation and future work

This section examines the limitations of the current work from three aspects, starting with the coupled flow-oxygen model itself in Section 7.2.1 followed by the model parameters in Section 7.2.2 and finally the brain mesh in Section 7.2.3. Continuation of the current work is presented in Section 7.2.4.

7.2.1 Model

In the previous chapter, a complete right middle cerebral artery occlusion, representing the worst case scenario, was simulated as a case study. Although it is unusual for ischaemic strokes to cause a complete blockage of a large vessel [5], constructing boundary condition for a partial occlusion is not straightforward. Blood pressure on the pial surface of the occluded territory is unknown as well as the velocity distribution prior to conducing the simulations [29]. Models describing the large vessels [26] and the leptomeningeal collateral circulation [27] can help determining the blood flow through the affected pial region.

The resultant pressure distribution of a partial occlusion simulation would likely have a smoother gradient between the occluded and its surrounding territories. This may allow the coupled flow-oxygen model to converge without the inclusion of tissue level collateral, providing a baseline measurement of the oxygen lesion. The influence of tissue level collateral on the infarct volume can then be studied independently.

Moreover, homogenisation underlies the foundation of the current multi-scale, multi-compartment model. It has been pointed out that the penetrating arteriolar trees are fractal in nature and it is questionable whether they should be homogenised [61,193]. However, it is unrealistic to model the arterioles explicitly at the organ level. From the results presented in the current study, the coupled flow-oxygen model is shown to be a promising first step; further evaluation against a cohort of imaging data is required to fully validate the model.

7.2.2 Parameters

As mentioned in Chapter 5, the parameter value chosen for the constant (τ) that results from linearising the oxygen disassociation curve may not be the best choice. Figure 7.1 shows the relationships between the blood oxygen concentration (C_b) and

the corresponding partial pressure of oxygen ($P^b_{O_2}$). Recall Equation (2.2) that

$$C_b = B_{O_2} C_{\mathrm{Hb}} S_{O_2} + \alpha_b P^b_{O_2}. \tag{7.1}$$

The solid black line illustrates the full relationship based on Hill equation approximated ODC. The blue dashed line and orange dotted dash line represent the linearised relationship ($P^b_{O_2} = \tau C_b/\alpha_b$) with $\tau = 0.01$ and $\tau = 0.008$, respectively.

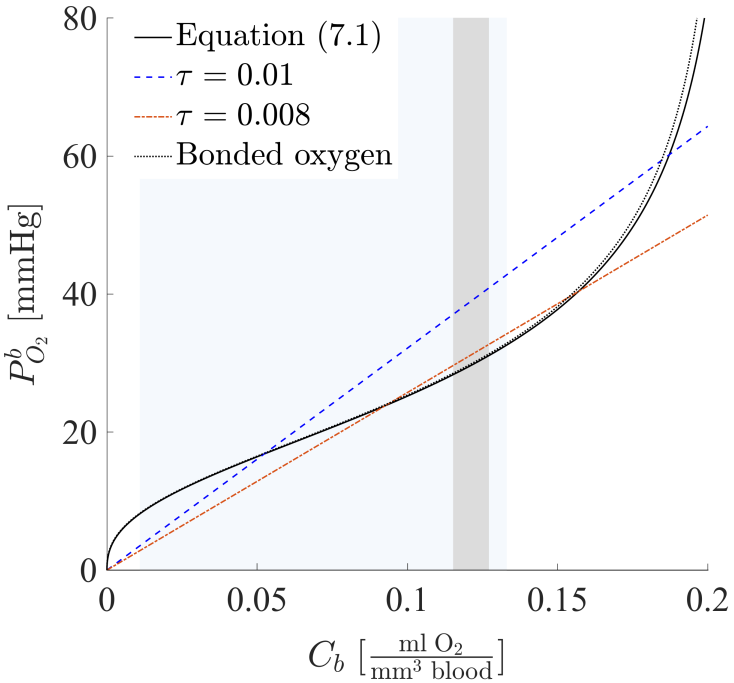


Figure 7.1: Relationship between $P^b_{O_2}$ and C_b.

The current model uses $\tau = 0.01$ and it can be seen that this appears to overestimate the value of $P^b_{O_2}$ when $0.052 < C_b < 0.187$ [mm^3 O$_2$/mm^3 blood] and to underestimate the value of $P^b_{O_2}$ otherwise. Although $\tau = 0.08$ — the lower bound found in the literature [139] — dose not give as good an estimation for the underestimated regions, it provides a much better approximation for the range of the optimised 1D capillary oxygen concentration (C_c) under healthy conditions which is indicated by the narrow (grey) band in Figure 7.1.

The capillary compartment is not sensitive to this parameter; there is only a 0.43% change in volume averaged oxygen concentration from a 20% change in parameter

value. However, the choice of τ has a large impact on the tissue compartment. Similar to the effect of oxygen solubility in tissue, the change in volume averaged tissue oxygen concentration (19.86%) is on the same scale as the change in the parameter value (20%). This is because τ alters the blood P_{O_2}, which affects the P_{O_2} gradient between the capillary and the tissue compartments.

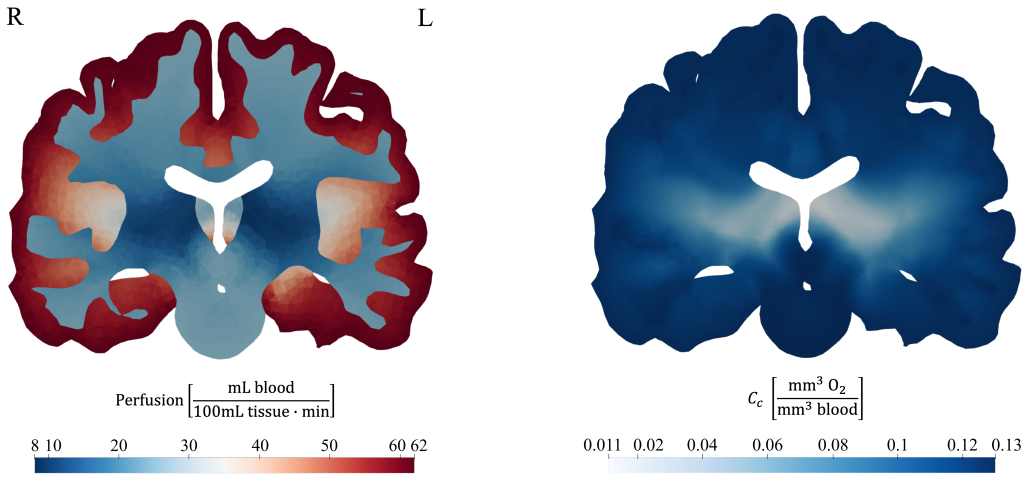
Therefore, it is important to accurately capture the value of $P^b_{O_2}$. Contrary to the approach in Chapter 3, only the term for oxygen bonded to haemoglobin ($B_{O_2}C_{\mathrm{Hb}}S_{O_2}$) is employed and the dissolved oxygen ($\alpha_b P_{O_2}$) is considered negligible. Rearranging and substituting Equation (7.1) into the Hill equation gives the following relationship

$$P^b_{O_2} = \left(\frac{C_b P_{50}}{B_{O_2} C_{\mathrm{Hb}} - C_b} \right)^{\frac{1}{n}}, \tag{7.2}$$

which is shown as the dotted black curve in Figure 7.1. Although Equation (7.2) is a very good approximation, its non-linearity makes the system too stiff to be solved.

Finding a best-fit value of τ for the linearised approximation may be enough for the 1D equivalent tissue column; however, more than one best-fit value may be required to improve the simulation results of the brain. The wide (pale blue) band in Figure 7.1 indicates the range of C_c from the healthy brain simulation, which spans across a large portion of the curve. This difference in oxygen concentration result between the 1D equivalent model and the 3D brain model is greater than the numerical errors.

The cause of this concentration difference is rooted in the difference between the 1D and 3D perfusion values. Despite the 1D and the 3D model having the same volume averaged perfusion, they do not have the same distribution throughout the depth of the brain. The minimum perfusion value of the 3D model is 2.5 times smaller than that of the 1D model. This under perfused region is found in the white matter, near the intersection of the lateral and the third ventricles (see Figure 7.2a), which is located the furthest away from the pial surface due to the missing sulci. The corresponding low oxygen region is highlighted in Figure 7.2b.



(a) Perfusion (b) Capillary oxygen concentration

Figure 7.2: Coronal view of (a) perfusion and (b) capillary oxygen concentration distribution under the healthy condition.

Additionally, it has been pointed out that there is a clear difference between the vascularisation in the grey matter and the white matter [45]. However, only the cortical vasculature has been quantitatively analysed. Therefore, the model's geometric parameter values are based solely on the morphology of the cortical vessels. Recently, Buch *et al.* [194] introduced a method that allowed vessels with a diameter around 50 μm be to imaged *in vivo*, which could help to gain further insights into the vessels in the white matter with possible quantification. This would also enable the construction of an additional compartment for arterioles that exclusively perfuse the white matter and the restoration of the original arteriolar compartment.

Another limitation of the parameters is that the same baseline (healthy) values are used in stroke simulations. As the brain undergoes hypoxia, the blood brain barrier starts to break down, which could affect the vessel wall's permeability to oxygen and vessel wall thickness. Within the cerebral tissue, oxygen diffusion coefficient and solubility could also change due to oedema formation. The metabolic process in the hypoperfused tissue would also be altered leading to different metabolic rates. Unfortunately, it is not trivial to estimate parameters for human physiological models, especially under pathological conditions, due to the lack of data and the gap between clinical measurements and mathematical representations. Experiments designed in

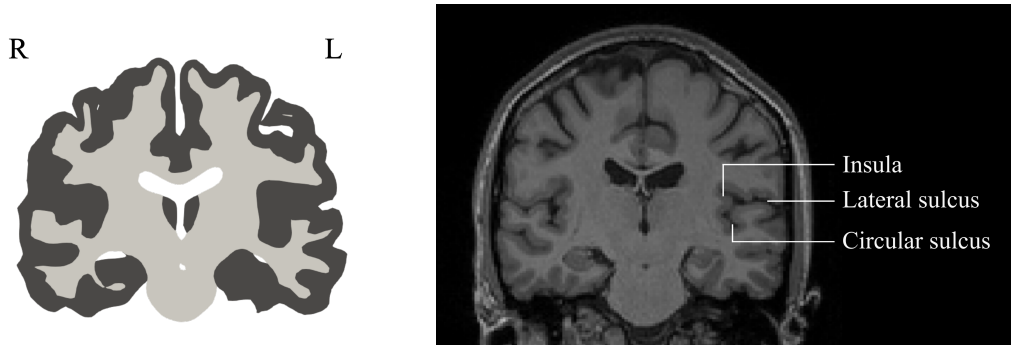
conjunction with computational model development would help bridging this gap. Based on the observation in this thesis, measurements on the coupling coefficients and the distributions of oxygen partial pressure would especially be useful.

7.2.3 Mesh

It is evident in Chapter 6 that much effort has been put in to reducing the numerical instabilities cased by the poorly shaped elements near the ventricle surface, including the use of second order elements for the Darcy pressure and first order elements for the Darcy velocity. Additionally, tissue level collateral was introduced to aid the convergence of the stroke simulations.

It is worth noting that, without tissue level collaterals, the perfusion lesion predicted by the second order pressure is 15% larger than the prediction made with the first order pressure. Given the results shown in the previous chapter, the oxygen lesions would have a similar difference if the model were to converge without tissue level collaterals and with first order pressure. A mesh with higher quality would allow a more comprehensive convergence analysis to be performed, which enables the determination of the near optimal settings.

Apart from mesh quality, the anatomical accuracy of the current patient-specific mesh also needs improvement. As illustrated in Figure 7.3, both the lateral and circular sulci are missing from the current mesh, especially in the right hemisphere. Although Figure 7.3b is not from the patient the mesh was constructed from, the lateral sulcus is the most prominent feature of the human brain. The space that should be filled with cerebrospinal fluid (CSF) is occupied by the grey matter instead and the insula is unidentifiable from the mesh. The lack of sulci not only contributes to the overestimation of the infarct volume followed by R-MCA occlusion, but is also responsible for the low oxygenation found near the ventricles as illustrated in the previous section.



(a) (b)

Figure 7.3: Coronal view of (a) the brain mesh and (b) the MRI image of a healthy subject (IXI025); adapted with annotation from [195] under license CC BY-SA 3.0 (https://creativecommons.org/licenses/by-sa/3.0/).

It is challenging to automatically obtain accurate segmentations and generate reliable patient-specific meshes. However, there are tools available to help to achieve a semi-automated process. Mardal *et al.* [196] used FreeSurfer [197] to extract the brain surfaces from T1-weighted images followed by creating the volume mesh with FreeSurfer and SVM-Tk [198]. Józsa *et al.* [199, 200] utilised SimNIBS [201] to generate masks of grey matter, white matter and CSF which were then manually adjusted, following human anatomy, to ensure that the brain tissue regions were well-separated. The mesh created by either approach has problems such as topological defeats and inaccurate connectivities, which require iterative adjustments to eliminate. Nonetheless, an accurate and reliable mesh would potentially greatly improve the accuracy of the simulation results.

7.2.4 Future work

The coupled flow-oxygen model has so far been implemented and tested under steady state. The next step, in addition to addressing the aforementioned limitations, is to reintroduce the temporal terms. Not only will this enable the incorporation of pathological parameter values, but also the ability to simulate the infarct evolution and incorporating important phenomena, such as oedema development. The volume of the ischaemic core and the penumbra could also be identified at any time point,

for example, by setting two hypoxia thresholds. However, in the long term, the ischaemic core and the penumbra should be computed based on well-fitted dynamic models.

Further validation of the model can be carried out by comparing the simulation results from a cohort of virtual patients [199, 200] to clinical imaging data. More specifically, initial and final imaging data of patients with unsuccessful treatments can be selected from clinical trials, such as the MR CLEAN trial [7], and the outcomes of the patients predicted by the model based on the initial imaging data can be compared against the outcomes obtained from the final imaging data. The model can then be extended to include a tissue death mechanism [30, 202] for treatment simulations where the blood supply is restored through thrombectomy, and patients who had favourable outcomes can be selected for model validation.

Nevertheless, validation itself remains an outstanding challenge. While these imaging data have high spatial resolution, they have very limited temporal resolution. This gap might be filled with experimental data from animals. In addition, the brain is a highly regulated organ and there is a tight coupling between tissue perfusion and metabolism due to the limited storage of oxygen and glucose. However, the model developed so far is purely passive. Incorporating active changes in blood flow in response to metabolic change in the future would further improve the model.

In conclusion, this thesis has developed a multi-scale, multi-compartment coupled flow-oxygen model that is capable of capturing the oxygen distribution followed by large vessel occlusions. The simulated lesion post R-MCA occlusion was shown to be in qualitative agreement with computed tomography images of a patient who suffered from a R-MCA stroke; the infarct volume estimated by the model compared well to quantitative data in the literature. With further validation and improvements, it is the hope that this model would be able to guide the development of novel treatments for ischaemic stroke and enable personalised treatment assessment and outcome prediction.

Appendix A

Transformation matrix for the permeability tensors

This appendix describes the transformation matrix that maps the permeability tensors from the reference coordinates to the local coordinates. The local permeability tensor for compartment i can be calculated as $\overline{\overline{K}}_i = \overline{\overline{R}}\overline{\overline{K}}_i^{ref}\overline{\overline{R}}^T$, where $\overline{\overline{R}}$ is the transformation matrix and it is calculated as

$$\overline{\overline{R}} = \cos(\theta)\overline{\overline{I}} + \sin(\theta)[\vec{e}_{rot}]_\times + [1 - \cos(\theta)](\vec{e}_{rot} \otimes \vec{e}_{rot}) \tag{A.1}$$

with $\overline{\overline{I}}$ representing the identity matrix and $\vec{e}_{rot}$ being the unit vector that defines the axis of rotation. The calculation of $\vec{e}_{rot}$ follows

$$\vec{e}_{rot} = \frac{\vec{e}_{ref} \times \vec{e}_{local}}{|\vec{e}_{ref} \times \vec{e}_{local}|}, \tag{A.2}$$

where $\vec{e}_{ref} = [0, 0, 1]$ is the unit vector of the reference coordinate system and $\vec{e}_{local}$ is the local characteristic direction described in Section 3.2 and computed as

$$\vec{e}_{local} = \frac{\nabla d}{|\nabla d|} \tag{A.3}$$

with d being the normalised brain tissue thickness [28].

The rotation angle θ is calculated as $\cos^{-1}(\vec{e}_{ref} \cdot \vec{e}_{local})$ and, finally, the cross product matrix of $\vec{e}_{rot}$ is

$$[\vec{e}_{rot}]_{\times} = \begin{bmatrix} 0 & -e_{rot,3} & e_{rot,2} \\ e_{rot,3} & 0 & -e_{rot,1} \\ -e_{rot,2} & e_{rot,1} & 0 \end{bmatrix}, \tag{A.4}$$

where $e_{rot,i}$ is the ith component of $\vec{e}_{rot}$.

Appendix B

Source terms of the manufactured solutions

Equation (B.1) below shows the source term expressions of the manufactured solutions constructed in Section 5.2.

$$
\begin{aligned}
R_a = &-66 + 192x - 176x^2 - 32x^3 + 16x^4 + 192y - 176y^2 - 32y^3 + 16y^4 + z^2 \\
&+ 102.4(x^2 - 2x^3 + x^4)(y^2 - 2y^3 + 4^4)(z-2)z^2 \\
&- 4096(x-1)^2 x^2 (y-1)^2 y^2 (z-1)^2 z^2 \\
&- 128(x-1)^2 x^2 (1-y)^2 y^2 z^2 (16x^2 - 32x^3 + 16x^4 + 16y^2 - 32y^3 + 16y^4 + z^2) \\
&\times (15 - 32z + 16z^2)(3 + \tanh(10z - 5))
\end{aligned} \tag{B.1a}
$$

$$
\begin{aligned}
R_c = &-16384(1 - 6x + 6x^2)(y-1)^2 y^2 (z-1)^2 z^2 + 4096(x-1)^2 x^2 (y-1)^2 y^2 (z-1)^2 z^2 \\
&- 16384(x-1)^2 x^2 (1 - 6y + 6y^2)(z-1)^2 z^2 \\
&- 16384(x-1)^2 x^2 (y-1)^2 y^2 (1 - 6z + 6z^2) \\
&- 1.34218 \times 10^7 (x^2 - 2x^3 + x^4)^2 (y^2 - 2y^3 + y^4)^2 (z - 3z^2 + 2z^3)^2 \\
&- 1.34218 \times 10^7 (x^2 - 2x^3 + x^4)^2 (y - 3y^2 + 2y^3)^2 (z^2 - 2z^3 + z^4)^2 \\
&- 1.34218 \times 10^7 (x - 3x^2 + 2x^3)^2 (y^2 - 2y^3 + y^4)^2 (z^2 - 2z^3 + z^4)^2 \\
&+ 3.35544 \times 10^7 (x-1)^4 x^4 (y-1)^4 y^4 (z-1)^4 z^4 (1.0625 - 2z + z^2) \\
&\times (3 + \tanh(10z - 5)) \\
&+ 128(x-1)^2 x^2 (1-y)^2 y^2 z^2 (16x^2 - 32x^3 + 16x^4 + 16y^2 - 32y^3 + 16y^4 + z^2)
\end{aligned}
$$

$$\times (15 - 32z + 16z^2)(3 + \tanh(10z - 5)) \tag{B.1b}$$

$$\begin{aligned} R_t = &- 16x^2 + 32x^3 - 16x^4 - 16y^2 + 32y^3 - 16y^4 - z^2 \\ &- 8192(1 - 6x + 6x^2)(y-1)^2 y^2 (z-1)^2 z^2 \\ &- 8192(x-1)^2 x^2 (1 - 6y + 6y^2)(z-1)^2 z^2 \\ &- 8192(x-1)^2 x^2 (y-1)^2 y^2 (1 - 6z + 6z^2) \\ &+ \frac{2048(x-1)^2 x^2 (y-1)^2 y^2 (z-1)^2 z^2 (1.5 + 0.5\tanh(10z - 5))}{1 + 4096(x-1)^2 x^2 (y-1)^2 y^2 (z-1)^2 z^2} \end{aligned} \tag{B.1c}$$

Bibliography

[1] GBD 2019 Stroke Collaborators, "Global, regional, and national burden of stroke and its risk factors, 1990–2019: a systematic analysis for the Global Burden of Disease Study 2019," *The Lancet Neurology*, vol. 20, no. 10, pp. 795–820, oct 2021.

[2] D. King, R. Wittenberg, A. Patel, Z. Quayyum, V. Berdunov, and M. Knapp, "The future incidence, prevalence and costs of stroke in the UK," *Age and Ageing*, vol. 49, no. 2, pp. 277–282, feb 2020.

[3] S. Strilciuc, D. Alecsandra Grad, C. Radu, D. Chira, A. Stan, M. Ungureanu, A. Gheorghe, and F.-D. Muresanu, "The economic burden of stroke: a systematic review of cost of illness studies," *Journal of Medicine and Life*, vol. 14, no. 5, pp. 606–619, jan 2021.

[4] D. Kuriakose and Z. Xiao, "Pathophysiology and Treatment of Stroke: Present Status and Future Perspectives," *International Journal of Molecular Sciences*, vol. 21, no. 20, p. 7609, oct 2020.

[5] P. Deb, S. Sharma, and K. M. Hassan, "Pathophysiologic mechanisms of acute ischemic stroke: An overview with emphasis on therapeutic significance beyond thrombolysis," *Pathophysiology*, vol. 17, no. 3, pp. 197–218, 2010.

[6] D. S. Liebeskind, "Reperfusion for acute ischemic stroke: arterial revascularization and collateral therapeutics," *Current Opinion in Neurology*, vol. 23, no. 1, pp. 36–45, feb 2010.

[7] P. S. Fransen, D. Beumer, O. A. Berkhemer, L. A. van den Berg, H. Lingsma, A. van der Lugt, W. H. van Zwam, R. J. van Oostenbrugge, Y. B. Roos, C. B. Majoie, and D. W. Dippel, "MR CLEAN, a multicenter randomized clinical trial of endovascular treatment for acute ischemic stroke in the Netherlands: Study protocol for a randomized controlled trial," *Trials*, vol. 15, no. 1, p. 343, 2014.

[8] O. A. Berkhemer, P. S. Fransen, D. Beumer, L. A. van den Berg, H. F. Lingsma, A. J. Yoo, W. J. Schonewille, J. A. Vos, P. J. Nederkoorn, M. J. Wermer, M. A. van Walderveen, J. Staals, J. Hofmeijer, J. A. van Oostayen, G. J. Lycklama à Nijeholt, J. Boiten, P. A. Brouwer, B. J. Emmer, S. F. de Bruijn, L. C. van Dijk, L. J. Kappelle, R. H. Lo, E. J. van Dijk, J. de Vries, P. L. de Kort, W. J. J. van Rooij, J. S. van den Berg, B. A. van Hasselt, L. A. Aerden, R. J. Dallinga, M. C. Visser, J. C. Bot, P. C. Vroomen, O. Eshghi, T. H. Schreuder, R. J. Heijboer, K. Keizer, A. V. Tielbeek, H. M. den Hertog,

D. G. Gerrits, R. M. van den Berg-Vos, G. B. Karas, E. W. Steyerberg, H. Z. Flach, H. A. Marquering, M. E. Sprengers, S. F. Jenniskens, L. F. Beenen, R. van den Berg, P. J. Koudstaal, W. H. van Zwam, Y. B. Roos, A. van der Lugt, R. J. van Oostenbrugge, C. B. Majoie, and D. W. Dippel, "A Randomized Trial of Intraarterial Treatment for Acute Ischemic Stroke," *New England Journal of Medicine*, vol. 372, no. 1, pp. 11–20, jan 2015.

[9] J. M. Wardlaw, V. Murray, E. Berge, G. Del Zoppo, P. Sandercock, R. L. Lindley, and G. Cohen, "Recombinant tissue plasminogen activator for acute ischaemic stroke: An updated systematic review and meta-analysis," *The Lancet*, vol. 379, no. 9834, pp. 2364–2372, jun 2012.

[10] M. S. Phipps and C. A. Cronin, "Management of acute ischemic stroke," *BMJ*, p. l6983, feb 2020.

[11] S. M. Pilgram-Pastor, E. I. Piechowiak, T. Dobrocky, J. Kaesmacher, J. Den Hollander, J. Gralla, and P. Mordasini, "Stroke thrombectomy complication management," *Journal of NeuroInterventional Surgery*, vol. 13, no. 10, pp. 912–917, oct 2021.

[12] C. J. Sommer, "Ischemic stroke: experimental models and reality," *Acta Neuropathologica*, vol. 133, no. 2, pp. 245–261, 2017.

[13] T. J. Moore, J. Heyward, G. Anderson, and G. C. Alexander, "Variation in the estimated costs of pivotal clinical benefit trials supporting the US approval of new therapeutic agents, 2015–2017: a cross-sectional study," *BMJ Open*, vol. 10, no. 6, p. e038863, jun 2020.

[14] G. C. Jickling and F. R. Sharp, "Improving the translation of animal ischemic stroke studies to humans," *Metabolic Brain Disease*, vol. 30, no. 2, pp. 461–467, 2015.

[15] M. Viceconti, F. Pappalardo, B. Rodriguez, M. Horner, J. Bischoff, and F. Musuamba Tshinanu, "In silico trials: Verification, validation and uncertainty quantification of predictive models used in the regulatory evaluation of biomedical products," *Methods*, vol. 185, pp. 120–127, jan 2021.

[16] A. Datta, V. Bansal, J. Diaz, J. Patel, D. Reato, and M. Bikson, "Gyri-precise head model of transcranial direct current stimulation: Improved spatial focality using a ring electrode versus conventional rectangular pad," *Brain Stimulation*, vol. 2, no. 4, pp. 201–207.e1, oct 2009.

[17] O. Puonti, G. B. Saturnino, K. H. Madsen, and A. Thielscher, "Value and limitations of intracranial recordings for validating electric field modeling for transcranial brain stimulation," *NeuroImage*, vol. 208, p. 116431, mar 2020.

[18] J. S. Giudice, W. Zeng, T. Wu, A. Alshareef, D. F. Shedd, and M. B. Panzer, "An Analytical Review of the Numerical Methods used for Finite Element Modeling of Traumatic Brain Injury," *Annals of Biomedical Engineering*, vol. 47, no. 9, pp. 1855–1872, sep 2019.

[19] P. Orlowski, D. O'Neill, V. Grau, Y. Ventikos, and S. Payne, "Modelling of the physiological response of the brain to ischaemic stroke," *Interface Focus*, vol. 3, no. 2, 2013.

[20] M. Mohamed Mokhtarudin and S. Payne, "Mathematical model of the effect of ischemia–reperfusion on brain capillary collapse and tissue swelling," *Mathematical Biosciences*, vol. 263, pp. 111–120, may 2015.

[21] G. E. Lang, D. Vella, S. L. Waters, and A. Goriely, "Propagation of damage in brain tissue: coupling the mechanics of oedema and oxygen delivery," *Biomechanics and Modeling in Mechanobiology*, vol. 14, no. 6, pp. 1197–1216, nov 2015.

[22] T. L. Fletcher, A. G. Kolias, P. J. A. Hutchinson, and M. P. F. Sutcliffe, "Development of a Finite Element Model of Decompressive Craniectomy," *PLoS ONE*, vol. 9, no. 7, p. e102131, jul 2014.

[23] T. L. Fletcher, B. Wirthl, A. G. Kolias, H. Adams, P. J. Hutchinson, and M. P. Sutcliffe, "Modelling of Brain Deformation After Decompressive Craniectomy," *Annals of Biomedical Engineering*, vol. 44, no. 12, pp. 3495–3509, 2016.

[24] P. R. Konduri, H. A. Marquering, E. E. van Bavel, A. Hoekstra, C. B. L. M. Majoie, and the INSIST Investigators, "In-Silico Trials for Treatment of Acute Ischemic Stroke," *Frontiers in Neurology*, vol. 11, sep 2020.

[25] C. Miller, R. M. Padmos, M. van der Kolk, T. I. Józsa, N. Samuels, Y. Xue, S. J. Payne, and A. G. Hoekstra, "In silico trials for treatment of acute ischemic stroke: Design and implementation," *Computers in Biology and Medicine*, vol. 137, p. 104802, oct 2021.

[26] R. M. Padmos, T. I. Józsa, W. K. El-Bouri, P. R. Konduri, S. J. Payne, and A. G. Hoekstra, "Coupling one-dimensional arterial blood flow to three-dimensional tissue perfusion models for in silico trials of acute ischaemic stroke," *Interface Focus*, vol. 11, no. 1, p. 20190125, 2021.

[27] R. M. Padmos, N. A. Terreros, T. I. Józsa, G. Závodszky, H. A. Marquering, C. B. Majoie, and A. G. Hoekstra, "Modelling the leptomeningeal collateral circulation during acute ischaemic stroke," *Medical Engineering and Physics*, vol. 91, pp. 1–11, 2021.

[28] T. I. Józsa, R. M. Padmos, N. Samuels, W. K. El-Bouri, A. G. Hoekstra, and S. J. Payne, "A porous circulation model of the human brain for in silico clinical trials in ischaemic stroke," *Interface Focus*, vol. 11, no. 1, p. 20190127, 2021, note that Figures 3.2, 6.1c and 6.8a–6.8c are used with permission of The Royal Society (U.K.), from this work; permission conveyed through Copyright Clearance Center, Inc.

[29] T. I. Józsa, R. M. Padmos, W. K. El-Bouri, A. G. Hoekstra, and S. J. Payne, "On the Sensitivity Analysis of Porous Finite Element Models for Cerebral Perfusion Estimation," *Annals of Biomedical Engineering*, jun 2021.

[30] Y. Xue, W. K. El-Bouri, T. I. Józsa, and S. J. Payne, "Modelling the effects of cerebral microthrombi on tissue oxygenation and cell death," *Journal of Biomechanics*, vol. 127, p. 110705, oct 2021.

[31] Y. Xue, T. Georgakopoulou, A.-E. van der Wijk, T. I. Józsa, E. van Bavel, and S. J. Payne, "Quantification of hypoxic regions distant from occlusions in cerebral penetrating arteriole trees," *PLOS Computational Biology*, vol. 18, no. 8, p. e1010166, aug 2022.

[32] M. Sharan, M. D. Jones, R. C. Koehler, R. J. Traystman, and A. S. Popel, "A compartmental model for oxygen transport in brain microcirculation," *Annals of Biomedical Engineering*, vol. 17, no. 1, pp. 13–38, jan 1989.

[33] D. A. Boas, S. R. Jones, A. Devor, T. J. Huppert, and A. M. Dale, "A vascular anatomical network model of the spatio-temporal response to brain activation," *NeuroImage*, vol. 40, no. 3, pp. 1116–1129, 2008.

[34] M. J. Barrett and V. Suresh, "Extra permeability is required to model dynamic oxygen measurements: Evidence for functional recruitment?" *Journal of Cerebral Blood Flow and Metabolism*, vol. 33, no. 9, pp. 1402–1411, sep 2013.

[35] S. J. Payne, *Cerebral Blood Flow and Metabolism: A Quantitative Approach*. World Scientific, nov 2017.

[36] A. Bacyinski, M. Xu, W. Wang, and J. Hu, "The Paravascular Pathway for Brain Waste Clearance: Current Understanding, Significance and Controversy," *Frontiers in Neuroanatomy*, vol. 11, nov 2017.

[37] S. Hall and J. Stephens, *Anatomy and physiology*, fifth edit ed., ser. Crash course. Amsterdam: Elsevier, 2018.

[38] S. W. Bothwell, D. Janigro, and A. Patabendige, "Cerebrospinal fluid dynamics and intracranial pressure elevation in neurological diseases," *Fluids and Barriers of the CNS*, vol. 16, no. 1, p. 9, dec 2019.

[39] N. Parker, M. Schneegurt, A. T. Tu, P. Lister, B. M. Forster, S. Allen, A. Auman, G. Brelles-Mariño, M. A. Feldman, P. Flowers, G. Pinchuk, B. Rowley, M. Sutherland, C. Franklund, and A. Paterson, *Microbiology*. Houston: Rice University, 2016. [Online]. Available: https://openstax.org/details/books/microbiology

[40] M. A. Clark, M. Douglas, and J. Choi, *Biology 2e*. Houston: Rice University, 2018. [Online]. Available: https://openstax.org/details/books/biology-2e

[41] J. G. Betts, K. A. Young, J. A. Wise, E. Johnson, B. Poe, D. H. Kruse, O. Korol, J. E. Johnson, M. Womble, and P. DeSaix, *Anatomy and Physiology*. Houston: Rice University, 2013. [Online]. Available: https://openstax.org/details/books/anatomy-and-physiology

[42] V. Papantchev, V. Stoinova, A. Aleksandrov, D. Todorova-Papantcheva, S. Hristov, D. Petkov, G. Nachev, and W. Ovtscharoff, "The role of Willis circle variations during unilateral selective cerebral perfusion: a study of 500

circles," *European Journal of Cardio-Thoracic Surgery*, vol. 44, no. 4, pp. 743–753, oct 2013.

[43] B. J. Alpers, R. G. Berry, and R. M. Paddison, "Anatomical Studies of the Circle of Willis in Normal Brain," *Archives of Neurology And Psychiatry*, vol. 81, no. 4, pp. 409–418, apr 1959.

[44] N. Tariq and R. Khatri, "Leptomeningeal collaterals in acute ischemic stroke." *Journal of vascular and interventional neurology*, vol. 1, no. 4, pp. 91–5, oct 2008.

[45] H. Duvernoy, S. Delon, and J. Vannson, "Cortical blood vessels of the human brain," *Brain Research Bulletin*, vol. 7, no. 5, pp. 519–579, nov 1981, note that Figure 2.3 is reprinted from this work, Copyright 1981, with permission from Elsevier.

[46] F. Reina-De La Torre, A. Rodriguez-Baeza, and J. Sahuquillo-Barris, "Morphological characteristics and distribution pattern of the arterial vessels in human cerebral cortex: A scanning electron microscope study," *Anatomical Record*, vol. 251, no. 1, pp. 87–96, 1998.

[47] F. Schmid, M. J. Barrett, P. Jenny, and B. Weber, "Vascular density and distribution in neocortex," *NeuroImage*, vol. 197, pp. 792–805, aug 2019, note that Figure 2.5 is reprinted from this work, Copyright 2019, with permission from Elsevier.

[48] S. Hirsch, J. Reichold, M. Schneider, G. Székely, and B. Weber, "Topology and hemodynamics of the cortical cerebrovascular system," *Journal of Cerebral Blood Flow & Metabolism*, vol. 32, no. 6, pp. 952–967, jun 2012.

[49] F. Cassot, F. Lauwers, C. Fouard, S. Prohaska, and V. Lauwers-Cances, "A novel three-dimensional computer-assisted method for a quantitative study of microvascular networks of the human cerebral cortex," *Microcirculation*, vol. 13, no. 1, pp. 1–18, jan 2006.

[50] L. Risser, F. Plouraboué, A. Steyer, P. Cloetens, G. Le Duc, and C. Fonta, "From Homogeneous to Fractal Normal and Tumorous Microvascular Networks in the Brain," *Journal of Cerebral Blood Flow & Metabolism*, vol. 27, no. 2, pp. 293–303, feb 2007.

[51] F. Lauwers, F. Cassot, V. Lauwers-Cances, P. Puwanarajah, and H. Duvernoy, "Morphometry of the human cerebral cortex microcirculation: General characteristics and space-related profiles," *NeuroImage*, vol. 39, no. 3, pp. 936–948, feb 2008.

[52] F. Cassot, F. Lauwers, S. Lorthois, P. Puwanarajah, and H. Duvernoy, "Scaling laws for branching vessels of human cerebral cortex," *Microcirculation*, vol. 16, no. 4, pp. 331–344, jan 2009.

[53] F. Cassot, F. Lauwers, S. Lorthois, P. Puwanarajah, V. Cances-Lauwers, and H. Duvernoy, "Branching patterns for arterioles and venules of the human cerebral cortex," *Brain Research*, vol. 1313, pp. 62–78, feb 2010.

[54] L. Risser, F. Plouraboué, P. Cloetens, and C. Fonta, "A 3D-investigation shows that angiogenesis in primate cerebral cortex mainly occurs at capillary level," *International Journal of Developmental Neuroscience*, vol. 27, no. 2, pp. 185–196, 2009.

[55] B. Weber, A. L. Keller, J. Reichold, and N. K. Logothetis, "The Microvascular System of the Striate and Extrastriate Visual Cortex of the Macaque," *Cerebral Cortex*, vol. 18, no. 10, pp. 2318–2330, oct 2008.

[56] S. Lorthois, F. Lauwers, and F. Cassot, "Tortuosity and other vessel attributes for arterioles and venules of the human cerebral cortex," *Microvascular Research*, vol. 91, pp. 99–109, 2014.

[57] R. Guibert, C. Fonta, L. Risser, and F. Plouraboué, "Coupling and robustness of intra-cortical vascular territories," *NeuroImage*, vol. 62, no. 1, pp. 408–417, aug 2012.

[58] D. L. Adams, V. Piserchia, J. R. Economides, and J. C. Horton, "Vascular supply of the cerebral cortex is specialized for cell layers but not columns," *Cerebral Cortex*, vol. 25, no. 10, pp. 3673–3681, oct 2015.

[59] M. J. Barrett, M. H. Tawhai, and V. Suresh, "Arteries dominate volume changes during brief functional hyperemia: Evidence from mathematical modelling," *NeuroImage*, vol. 62, no. 1, pp. 482–492, aug 2012.

[60] S. Lorthois, F. Cassot, and F. Lauwers, "Simulation study of brain blood flow regulation by intra-cortical arterioles in an anatomically accurate large human vascular network: Part I: Methodology and baseline flow," *NeuroImage*, vol. 54, no. 2, pp. 1031–1042, jan 2011.

[61] S. Lorthois and F. Cassot, "Fractal analysis of vascular networks: Insights from morphogenesis," *Journal of Theoretical Biology*, vol. 262, no. 4, pp. 614–633, feb 2010.

[62] K. A. Kasischke, E. M. Lambert, B. Panepento, A. Sun, H. A. Gelbard, R. W. Burgess, T. H. Foster, and M. Nedergaard, "Two-photon NADH imaging exposes boundaries of oxygen diffusion in cortical vascular supply regions," *Journal of Cerebral Blood Flow and Metabolism*, vol. 31, no. 1, pp. 68–81, 2011.

[63] A. Devor, S. Sakadzic, P. A. Saisan, M. A. Yaseen, E. Roussakis, V. J. Srinivasan, S. A. Vinogradov, B. R. Rosen, R. B. Buxton, A. M. Dale, and D. A. Boas, ""Overshoot" of O2 Is Required to Maintain Baseline Tissue Oxygenation at Locations Distal to Blood Vessels," *Journal of Neuroscience*, vol. 31, no. 38, pp. 13 676–13 681, sep 2011.

[64] S. Sakadžić, E. T. Mandeville, L. Gagnon, J. J. Musacchia, M. A. Yaseen, M. A. Yucel, J. Lefebvre, F. Lesage, A. M. Dale, K. Eikermann-Haerter, C. Ayata, V. J. Srinivasan, E. H. Lo, A. Devor, and D. A. Boas, "Large arteriolar component of oxygen delivery implies a safe margin of oxygen supply to cerebral tissue," *Nature Communications*, vol. 5, no. 1, p. 5734, dec 2014.

[65] S. Lorthois, F. Cassot, and F. Lauwers, "Simulation study of brain blood flow regulation by intra-cortical arterioles in an anatomically accurate large

human vascular network. Part II: Flow variations induced by global or localized modifications of arteriolar diameters," *NeuroImage*, vol. 54, no. 4, pp. 2840–2853, feb 2011.

[66] S.-W. Su, M. Catherall, and S. Payne, "The Influence of Network Structure on the Transport of Blood in the Human Cerebral Microvasculature," *Microcirculation*, vol. 19, no. 2, pp. 175–187, 2012.

[67] A. A. Linninger, I. G. Gould, T. Marinnan, C. Y. Hsu, M. Chojecki, and A. Alaraj, "Cerebral microcirculation and oxygen tension in the human secondary cortex," *Annals of Biomedical Engineering*, vol. 41, no. 11, pp. 2264–2284, jul 2013.

[68] W. K. El-Bouri and S. J. Payne, "Multi-scale homogenization of blood flow in 3-dimensional human cerebral microvascular networks," *Journal of Theoretical Biology*, vol. 380, pp. 40–47, sep 2015, note that Figure 4.1 is reprinted from this work, Copyright 2015, with permission from Elsevier.

[69] A. C. Burton, "Relation of Structure to Function of the Tissues of the Wall of Blood Vessels," *Physiological Reviews*, vol. 34, no. 4, pp. 619–642, oct 1954.

[70] K. Rakusan and P. Wicker, "Morphometry of the small arteries and arterioles in the rat heart: Effects of chronic hypertension and exercise," *Cardiovascular Research*, vol. 24, no. 4, pp. 278–284, 1990.

[71] B. Müller, S. Lang, M. Dominietto, M. Rudin, G. Schulz, H. Deyhle, M. Germann, F. Pfeiffer, C. David, and T. Weitkamp, "High-resolution tomographic imaging of microvessels," S. R. Stock, Ed., aug 2008, p. 70780B.

[72] S. J. Payne and C. Lucas, "Oxygen delivery from the cerebral microvasculature to tissue is governed by a single time constant of approximately 6 seconds," *Microcirculation*, vol. 25, no. 2, p. e12428, feb 2018.

[73] B. Koeppen and B. Stanton, *Berne and Levy Physiology*, 7th ed. Philadephia: Elsevier, 2018.

[74] H. Kadry, B. Noorani, and L. Cucullo, "A blood–brain barrier overview on structure, function, impairment, and biomarkers of integrity," *Fluids and Barriers of the CNS*, vol. 17, no. 1, p. 69, dec 2020.

[75] N. J. Abbott, A. A. Patabendige, D. E. Dolman, S. R. Yusof, and D. J. Begley, "Structure and function of the blood–brain barrier," *Neurobiology of Disease*, vol. 37, no. 1, pp. 13–25, jan 2010, note that Figure 2.7 is reprinted from this work, Copyright 2010, with permission from Elsevier.

[76] M. Cavaglia, S. M. Dombrowski, J. Drazba, A. Vasanji, P. M. Bokesch, and D. Janigro, "Regional variation in brain capillary density and vascular response to ischemia," *Brain Research*, vol. 910, no. 1-2, pp. 81–93, aug 2001.

[77] A. P. Fan, H. An, F. Moradi, J. Rosenberg, Y. Ishii, T. Nariai, H. Okazawa, and G. Zaharchuk, "Quantification of brain oxygen extraction and metabolism with [15O]-gas PET: A technical review in the era of PET/MRI," p. 117136, oct 2020.

[78] F. L. Powell, P. D. Wagner, and J. B. West, "Ventilation, Blood Flow, and Gas Exchange," in *Murray and Nadel's Textbook of Respiratory Medicine*. Elsevier, 2016, pp. 44–75.e3.

[79] J. A. Collins, A. Rudenski, J. Gibson, L. Howard, and R. O'Driscoll, "Relating oxygen partial pressure, saturation and content: The haemoglobin–oxygen dissociation curve," *Breathe*, vol. 11, no. 3, pp. 194–201, sep 2015.

[80] J. F. O'Riordan, T. K. Goldstick, J. Ditzel, and J. T. Ernest, "Characterization of Oxygen-Hemoglobin Equilibrium Curves Using Nonlinear Regression of the Hill Equation: Parameter Values for Normal Human Adults," in *Oxygen Transport to Tissue-IV*, H. I. Bicher, , and D. F. Bruley, Eds. Springer US, 1983, vol. 159, pp. 435–444.

[81] L. C. Clark, R. Wolf, D. Granger, and Z. Taylor, "Continuous Recording of Blood Oxygen Tensions by Polarography," *Journal of Applied Physiology*, vol. 6, no. 3, pp. 189–193, sep 1953.

[82] J. W. Severinghaus and P. B. Astrup, "History of blood gas analysis. IV. Leland Clark's oxygen electrode," *Journal of Clinical Monitoring*, vol. 2, no. 2, pp. 125–139, apr 1986.

[83] S. Sakadžić, E. Roussakis, M. A. Yaseen, E. T. Mandeville, V. J. Srinivasan, K. Arai, S. Ruvinskaya, A. Devor, E. H. Lo, S. A. Vinogradov, and D. A. Boas, "Two-photon high-resolution measurement of partial pressure of oxygen in cerebral vasculature and tissue," *Nature Methods*, vol. 7, no. 9, pp. 755–759, sep 2010.

[84] B. R. Duling, W. Kuschinsky, and M. Wahl, "Measurements of the perivascular PO2 in the vicinity of the pial vessels of the cat," *Pflügers Archiv European Journal of Physiology*, vol. 383, no. 1, pp. 29–34, 1979.

[85] E. Vovenko, "Distribution of oxygen tension on the surface of arterioles, capillaries and venules of brain cortex and in tissue in normoxia: An experimental study on rats," *Pflugers Archiv European Journal of Physiology*, vol. 437, no. 4, pp. 617–623, 1999.

[86] E. P. Vovenko and A. E. Chuikin, "Oxygen tension in rat cerebral cortex microvessels in acute anemia," *Neuroscience and Behavioral Physiology*, vol. 38, no. 5, pp. 493–500, jun 2008.

[87] A. L. Vazquez, M. Fukuda, M. L. Tasker, K. Masamoto, and S.-G. Kim, "Changes in Cerebral Arterial, Tissue and Venous Oxygenation with Evoked Neural Stimulation: Implications for Hemoglobin-Based Functional Neuroimaging," *Journal of Cerebral Blood Flow & Metabolism*, vol. 30, no. 2, pp. 428–439, feb 2010.

[88] M. A. Yaseen, V. J. Srinivasan, S. Sakadžić, H. Radhakrishnan, I. Gorczynska, W. Wu, J. G. Fujimoto, and D. A. Boas, "Microvascular Oxygen Tension and Flow Measurements in Rodent Cerebral Cortex during Baseline Conditions and Functional Activation," *Journal of Cerebral Blood Flow & Metabolism*, vol. 31, no. 4, pp. 1051–1063, apr 2011.

[89] M. G. Levitzky, "Chapter 7. Transport of Oxygen and Carbon Dioxide in the Blood," in *Pulmonary Physiology*, 8th ed. McGraw Hill, 2013.

[90] C. Thomas and A. B. Lumb, "Physiology of haemoglobin," *Continuing Education in Anaesthesia Critical Care & Pain*, vol. 12, no. 5, pp. 251–256, oct 2012.

[91] R. Zander, "Oxygen solubility in normal human blood," in *Oxygen Transport to Tissue*. Elsevier, 1981, pp. 331–332.

[92] T. W. Secomb, R. Hsu, E. Y. H. Park, and M. W. Dewhirst, "Green's Function Methods for Analysis of Oxygen Delivery to Tissue by Microvascular Networks," *Annals of Biomedical Engineering*, vol. 32, no. 11, pp. 1519–1529, nov 2004.

[93] A. S. Popel, R. N. Pittman, and M. L. Ellsworth, "Rate of oxygen loss from arterioles is an order of magnitude higher than expected," *American Journal of Physiology - Heart and Circulatory Physiology*, vol. 256, no. 3, 1989.

[94] A. Carreau, B. El Hafny-Rahbi, A. Matejuk, C. Grillon, and C. Kieda, "Why is the partial oxygen pressure of human tissues a crucial parameter? Small molecules and hypoxia." *Journal of cellular and molecular medicine*, vol. 15, no. 6, pp. 1239–53, jun 2011.

[95] J. Meixensberger, J. Dings, H. Kuhnigk, and K. Roosen, "Studies of Tissue PO2 in Normal and Pathological Human Brain Cortex," in *Monitoring of Cerebral Blood Flow and Metabolism in Intensive Care*. Vienna: Springer Vienna, 1993, pp. 58–63.

[96] W. Hoffman, F. Charbel, and G. Edelman, "Brain tissue oxygen, carbon dioxide, and pH in neurosurgical patients at risk for ischemia," *Anesthesia and Analgesia*, vol. 82, no. 3, pp. 582–586, 1996.

[97] J. Dings, J. Meixensberger, A. Jäger, and K. Roosen, "Clinical Experience with 118 Brain Tissue Oxygen Partial Pressure Catheter Probes," *Neurosurgery*, vol. 43, no. 5, pp. 1082–1094, nov 1998.

[98] D. K. Clark, W. Erdmann, J. H. Halsey, and E. Strong, "Oxygen diffusion, conductivity and solubility coefficients in the microarea of the brain. (Measurements with noble metal microelectrodes)." *Advances in Experimental Medicine and Biology*, vol. 94, pp. 697–704, 1977.

[99] M. A. Mintun, B. N. Lundstrom, A. Z. Snyder, A. G. Vlassenko, G. L. Shulman, and M. E. Raichle, "Blood flow and oxygen delivery to human brain during functional activity: Theoretical modeling and experimental data," *Proceedings of the National Academy of Sciences of the United States of America*, vol. 98, no. 12, pp. 6859–6864, jun 2001.

[100] C. Leithner and G. Royl, "The oxygen paradox of neurovascular coupling," *Journal of Cerebral Blood Flow and Metabolism*, vol. 34, no. 1, pp. 19–29, 2014.

[101] M. T. Wyss, R. Jolivet, A. Buck, P. J. Magistretti, and B. Weber, "In Vivo Evidence for Lactate as a Neuronal Energy Source," *Journal of Neuroscience*, vol. 31, no. 20, pp. 7477–7485, may 2011.

[102] A. Aubert and R. Costalat, "A model of the coupling between brain electrical activity, metabolism, and hemodynamics: Application to the interpretation of functional neuroimaging," *NeuroImage*, vol. 17, no. 3, pp. 1162–1181, 2002.

[103] ——, "Interaction between astrocytes and neurons studied using a mathematical model of compartmentalized energy metabolism," *Journal of Cerebral Blood Flow and Metabolism*, vol. 25, no. 11, pp. 1476–1490, 2005.

[104] M. Cloutier, F. B. Bolger, J. P. Lowry, and P. Wellstead, "An integrative dynamic model of brain energy metabolism using in vivo neurochemical measurements," *Journal of Computational Neuroscience*, vol. 27, no. 3, pp. 391–414, 2009.

[105] R. Jolivet, J. S. Coggan, I. Allaman, and P. J. Magistretti, "Multi-timescale Modeling of Activity-Dependent Metabolic Coupling in the Neuron-Glia-Vasculature Ensemble," *PLOS Computational Biology*, vol. 11, no. 2, p. e1004036, feb 2015.

[106] L. Michaelis and M. L. Menten, "Die Kinetik der Invertinwirkung," *Biochem Z*, vol. 49, no. February, pp. 333–369, 1913.

[107] M. A. Mintun, M. E. Raichie, W. R. Martin, and P. Herscovitch, "Brain oxygen utilization measured with O-15 radiotracers and positron emission tomography," *Journal of Nuclear Medicine*, vol. 25, no. 2, pp. 177–187, 1984.

[108] J. Cho, Y. Kee, P. Spincemaille, T. D. Nguyen, J. Zhang, A. Gupta, S. Zhang, and Y. Wang, "Cerebral metabolic rate of oxygen (CMRO2) mapping by combining quantitative susceptibility mapping (QSM) and quantitative blood oxygenation level-dependent imaging (qBOLD)," pp. 1595–1604, oct 2018.

[109] M. E. Raichle, A. M. MacLeod, A. Z. Snyder, W. J. Powers, D. A. Gusnard, and G. L. Shulman, "A default mode of brain function," *PNAS*, vol. 98, no. 2, pp. 676–82, 2001.

[110] A. Krogh, "The supply of oxygen to the tissues and the regulation of the capillary circulation," *The Journal of Physiology*, vol. 52, no. 6, pp. 457–474, may 1919.

[111] D. A. Beard and J. B. Bassingthwaighte, "Modeling advection and diffusion of oxygen in complex vascular networks," *Annals of Biomedical Engineering*, vol. 29, no. 4, pp. 298–310, apr 2001.

[112] T. D. Lagerlund and P. A. Low, "Axial diffusion and Michaelis-Menten kinetics in oxygen delivery in rat peripheral nerve," *American Journal of Physiology-Regulatory, Integrative and Comparative Physiology*, vol. 260, no. 2, pp. R430–R440, feb 1991.

[113] B. J. McGuire and T. W. Secomb, "Estimation of capillary density in human skeletal muscle based on maximal oxygen consumption rates," *American*

Journal of Physiology-Heart and Circulatory Physiology, vol. 285, no. 6, pp. H2382–H2391, dec 2003.

[114] T. D. Lagerlund and P. A. Low, "Mathematical modeling of time-dependent oxygen transport in rat peripheral nerve," *Computers in Biology and Medicine*, vol. 23, no. 1, pp. 29–47, jan 1993.

[115] J. E. Fletcher and R. W. Schubert, "Axial diffusion and wall permeability effects in perfused capillary-tissue structures," *Biosystems*, vol. 20, no. 2, pp. 153–174, jan 1987.

[116] P. A. Wieringa, H. G. Stassen, J. J. Van Kan, and J. A. Spaan, "Oxygen diffusion in a network model of the myocardial microcirculation." *International journal of microcirculation, clinical and experimental / sponsored by the European Society for Microcirculation*, vol. 13, no. 2, pp. 137–169, 1993.

[117] D. Goldman and A. S. Popel, "A Computational Study of the Effect of Capillary Network Anastomoses and Tortuosity on Oxygen Transport," *Journal of Theoretical Biology*, vol. 206, no. 2, pp. 181–194, sep 2000.

[118] R. Hsu and T. W. Secomb, "A Green's function method for analysis of oxygen delivery to tissue by microvascular networks," *Mathematical Biosciences*, vol. 96, no. 1, pp. 61–78, sep 1989.

[119] T. W. Secomb, R. Hsu, N. B. Beamer, and B. M. Coull, "Theoretical simulation of oxygen transport to brain by networks of microvessels: effects of oxygen supply and demand on tissue hypoxia." *Microcirculation*, vol. 7, no. 4, pp. 237–47, aug 2000.

[120] Q. Fang, S. Sakadžić, L. Ruvinskaya, A. Devor, A. M. Dale, and D. A. Boas, "Oxygen advection and diffusion in a three-dimensional vascular anatomical network," *Optics Express*, vol. 16, no. 22, p. 17530, 2008.

[121] L. Gagnon, S. Sakadžić, F. Lesage, J. J. Musacchia, X. Lefebvre, Q. Fang, M. A. Yücel, K. C. Evans, E. T. Mandeville, J. Cohen-Adad, J. R. Polimeni, M. A. Yaseen, E. H. Lo, D. N. Greve, R. B. Buxton, A. M. Dale, A. Devor, and D. A. Boas, "Quantifying the Microvascular Origin of BOLD-fMRI from First Principles with Two-Photon Microscopy and an Oxygen-Sensitive Nanoprobe," *Journal of Neuroscience*, vol. 35, no. 8, pp. 3663–3675, 2015.

[122] T. Köppl, E. Vidotto, and B. Wohlmuth, "A 3D-1D coupled blood flow and oxygen transport model to generate microvascular networks," *International Journal for Numerical Methods in Biomedical Engineering*, vol. 36, no. 10, oct 2020.

[123] W. K. El-Bouri and S. J. Payne, "A statistical model of the penetrating arterioles and venules in the human cerebral cortex," *Microcirculation*, vol. 23, no. 7, pp. 580–590, oct 2016.

[124] S.-w. Su, "Modelling Blood Flow and Oxygen Transport in the Human Cerebral," Ph.D. dissertation, University of Oxford, 2011.

[125] E. Hodneland, E. Hanson, O. Sævareid, G. Nævdal, A. Lundervold, V. Šoltészová, A. Z. Munthe-Kaas, A. Deistung, J. R. Reichenbach, and J. M.

Nordbotten, "A new framework for assessing subject-specific whole brain circulation and perfusion using mri-based measurements and a multiscale continuous flow model," *PLoS Computational Biology*, vol. 15, no. 6, 2019.

[126] F. Schmid, P. S. Tsai, D. Kleinfeld, P. Jenny, and B. Weber, "Depth-dependent flow and pressure characteristics in cortical microvascular networks," *PLoS Computational Biology*, vol. 13, no. 2, p. e1005392, feb 2017.

[127] L. Guo, Z. Li, J. Lyu, Y. Mei, J. C. Vardakis, D. Chen, C. Han, X. Lou, and Y. Ventikos, "On the Validation of a Multiple-Network Poroelastic Model Using Arterial Spin Labeling MRI Data," *Frontiers in Computational Neuroscience*, vol. 13, sep 2019.

[128] L. Guo, J. C. Vardakis, T. Lassila, M. Mitolo, N. Ravikumar, D. Chou, M. Lange, A. Sarrami-Foroushani, B. J. Tully, Z. A. Taylor, S. Varma, A. Venneri, A. F. Frangi, and Y. Ventikos, "Subject-specific multi-poroelastic model for exploring the risk factors associated with the early stages of Alzheimer's disease," *Interface Focus*, vol. 8, no. 1, p. 20170019, feb 2018.

[129] L. Guo, J. C. Vardakis, D. Chou, and Y. Ventikos, "A multiple-network poroelastic model for biological systems and application to subject-specific modelling of cerebral fluid transport," *International Journal of Engineering Science*, vol. 147, p. 103204, feb 2020.

[130] T. Hasegawa, J. R. Ravens, and J. F. Toole, "Precapillary Arteriovenous Anastomoses: "Thoroughfare Channels" in the Brain," *Archives of Neurology*, vol. 16, no. 2, pp. 217–224, 1967.

[131] B. S. Gardiner, S. L. Thompson, J. P. Ngo, D. W. Smith, A. Abdelkader, B. R. Broughton, J. F. Bertram, and R. G. Evans, "Diffusive oxygen shunting between vessels in the preglomerular renal vasculature: Anatomic observations and computational modeling," *American Journal of Physiology - Renal Physiology*, vol. 303, no. 5, sep 2012.

[132] J. Lecoq, A. Parpaleix, E. Roussakis, M. Ducros, Y. G. Houssen, S. A. Vinogradov, and S. Charpak, "Simultaneous two-photon imaging of oxygen and blood flow in deep cerebral vessels," *Nature Medicine*, vol. 17, no. 7, pp. 893–898, jul 2011.

[133] K. Masamoto and K. Tanishita, "Oxygen Transport in Brain Tissue," *Journal of Biomechanical Engineering*, vol. 131, no. 7, p. 074002, 2009.

[134] G. Závodszky, B. van Rooij, B. Czaja, V. Azizi, D. de Kanter, and A. G. Hoekstra, "Red blood cell and platelet diffusivity and margination in the presence of cross-stream gradients in blood flows," *Physics of Fluids*, vol. 31, no. 3, p. 031903, mar 2019.

[135] J. C. Cruz Hernández, O. Bracko, C. J. Kersbergen, V. Muse, M. Haft-Javaherian, M. Berg, L. Park, L. K. Vinarcsik, I. Ivasyk, D. A. Rivera, Y. Kang, M. Cortes-Canteli, M. Peyrounette, V. Doyeux, A. Smith, J. Zhou, G. Otte, J. D. Beverly, E. Davenport, Y. Davit, C. P. Lin, S. Strickland, C. Iadecola, S. Lorthois, N. Nishimura, and C. B. Schaffer, "Neutrophil adhesion in brain capillaries reduces cortical blood flow and impairs memory

function in Alzheimer's disease mouse models," *Nature Neuroscience*, vol. 22, no. 3, pp. 413–420, mar 2019.

[136] M. Berg, Y. Davit, M. Quintard, and S. Lorthois, "Modelling solute transport in the brain microcirculation: is it really well mixed inside the blood vessels?" *Journal of Fluid Mechanics*, vol. 884, p. A39, feb 2020.

[137] P. W. Sweeney, S. Walker-Samuel, and R. J. Shipley, "Insights into cerebral haemodynamics and oxygenation utilising in vivo mural cell imaging and mathematical modelling," *Scientific Reports*, vol. 8, no. 1, p. 1373, dec 2018.

[138] Y. Davit, C. G. Bell, H. M. Byrne, L. A. Chapman, L. S. Kimpton, G. E. Lang, K. H. Leonard, J. M. Oliver, N. C. Pearson, R. J. Shipley, S. L. Waters, J. P. Whiteley, B. D. Wood, and M. Quintard, "Homogenization via formal multiscale asymptotics and volume averaging: How do the two techniques compare?" *Advances in Water Resources*, vol. 62, pp. 178–206, dec 2013.

[139] Y. Zheng, J. Martindale, D. Johnston, M. Jones, J. Berwick, and J. Mayhew, "A model of the hemodynamic response and oxygen delivery to brain," *NeuroImage*, vol. 16, no. 3 I, pp. 617–637, jul 2002.

[140] C. Nicholson, "Diffusion and related transport mechanisms in brain tissue," *Reports on Progress in Physics*, vol. 64, no. 7, pp. 815–884, 2001.

[141] A. J. Mcgoron, P. Nair, and R. W. Schubert, "Michaelis-Menten kinetics model of oxygen consumption by rat brain slices following hypoxia," *Annals of Biomedical Engineering*, vol. 25, no. 3, pp. 565–572, 1997.

[142] D. G. Buerk and P. Nair, "PtiO2 and CMRO2 changes in cortex and hippocampus of aging gerbil brain," *Journal of Applied Physiology*, vol. 74, no. 4, pp. 1723–1728, apr 1993.

[143] D. G. Buerk and G. M. Saidel, "Local kinetics of oxygen metabolism in brain and liver tissues," *Microvascular Research*, vol. 16, no. 3, pp. 391–405, nov 1978.

[144] D. Hershey and T. Karhan, "Diffusion coefficients for oxygen transport in whole blood," *AIChE Journal*, vol. 14, no. 6, pp. 969–972, nov 1968.

[145] T. K. Goldstick, V. T. Ciuryla, and L. Zuckerman, "Diffusion of oxygen in plasma and blood." *Advances in experimental medicine and biology*, vol. 75, pp. 183–190, 1976.

[146] R. Valabregue, A. Aubert, J. Burger, J. Bittoun, and R. Costalat, "Relation between cerebral blood flow and metabolism explained by a model of oxygen exchange," *Journal of Cerebral Blood Flow & Metabolism*, vol. 23, no. 5, pp. 536–545, may 2003.

[147] H. An, W. Lin, A. Celik, and Y. Z. Lee, "Quantitative measurements of cerebral metabolic rate of oxygen utilization using MRI: A volunteer study," *NMR in Biomedicine*, vol. 14, no. 7-8, pp. 441–447, 2001.

[148] D. Paech, A. M. Nagel, M. N. Schultheiss, R. Umathum, S. Regnery, M. Scherer, A. Wick, T. Platt, W. Wick, M. Bendszus, A. Unterberg, H. P.

Schlemmer, M. E. Ladd, and S. C. Niesporek, "Quantitative dynamic oxygen 17 MRI at 7.0 T for the cerebral oxygen metabolism in glioma," *Radiology*, vol. 295, no. 1, pp. 181–189, 2020.

[149] J. Bear, *Dynamics of Fluids in Porous Media*. New York: Dover Publications, 1988.

[150] T. W. Anderson and D. A. Darling, "Asymptotic Theory of Certain "Goodness of Fit" Criteria Based on Stochastic Processes," *The Annals of Mathematical Statistics*, vol. 23, no. 2, pp. 193–212, 1952.

[151] R. Fåhræus and T. Lindqvist, "The viscosity of the blood in narrow capillary tubes," *American Journal of Physiology-Legacy Content*, vol. 96, no. 3, pp. 562–568, mar 1931.

[152] A. Logg, K. A. Mardal, and G. Wells, ser. Lecture Notes in Computational Science and Engineering, A. Logg, K.-A. Mardal, and G. Wells, Eds. Berlin, Heidelberg: Springer Berlin Heidelberg, 2012, vol. 84.

[153] T. J. R. Hughes, *The Finite Element Method: Linear Static and Dynamic Finite Element Analysis*. New York: Dover Publications, 2003.

[154] K. Salari and P. Knupp, "Code verification by the method of manufactured solutions," Sandia National Laboratories, Albuquerque, Tech. Rep. 1, 2002.

[155] P. J. Roache, "The Method of Manufactured Solutions for Code Verification," in *Computer Simulation Validation*, C. Beisbart and N. Saam, Eds. Springer Chem, 2019, pp. 295–318.

[156] Wolfram Research, Inc., "Mathematica, Version 12.0," champaign, IL, 2019.

[157] L. Vazquez, Alberto, K. Masamoto, M. Fukuda, and S.-G. Kim, "Cerebral oxygen delivery and consumption during evoked neural activity," *Frontiers in Neuroenergetics*, vol. 2, 2010.

[158] P. Pantano, J. C. Baron, P. Lebrun-Grandié, N. Duquesnoy, M. G. Bousser, and D. Comar, "Regional cerebral blood flow and oxygen consumption in human aging." *Stroke*, vol. 15, no. 4, pp. 635–641, jul 1984.

[159] J. S. Perlmutter, W. J. Powers, P. Herscovitch, P. T. Fox, and M. E. Raichle, "Regional Asymmetries of Cerebral Blood Flow, Blood Volume, and Oxygen Utilization and Extraction in Normal Subjects," *Journal of Cerebral Blood Flow & Metabolism*, vol. 7, no. 1, pp. 64–67, feb 1987.

[160] I. Uwano, K. Kudo, R. Sato, K. Ogasawara, H. Kameda, J. I. Nomura, F. Mori, F. Yamashita, K. Ito, K. Yoshioka, and M. Sasaki, "Noninvasive Assessment of Oxygen Extraction Fraction in Chronic Ischemia Using Quantitative Susceptibility Mapping at 7 Tesla," *Stroke*, vol. 48, no. 8, pp. 2136–2141, aug 2017.

[161] Q. Qin, K. Grgac, and P. C. van Zijl, "Determination of whole-brain oxygen extraction fractions by fast measurement of blood T 2 in the jugular vein," *Magnetic Resonance in Medicine*, vol. 65, no. 2, pp. 471–479, feb 2011.

[162] C. Zhu, R. H. Byrd, P. Lu, and J. Nocedal, "Algorithm 778: L-BFGS-B," *ACM Transactions on Mathematical Software*, vol. 23, no. 4, pp. 550–560, dec 1997.

[163] J. A. Nelder and R. Mead, "A Simplex Method for Function Minimization," *The Computer Journal*, vol. 7, no. 4, pp. 308–313, jan 1965.

[164] Z.-C. Feng, E. L. Roberts, T. J. Sick, and M. Rosenthal, "Depth profile of local oxygen tension and blood flow in rat cerebral cortex, white matter and hippocampus," *Brain Research*, vol. 445, no. 2, pp. 280–288, apr 1988.

[165] R. H. Smith, E. J. Guilbeau, and D. D. Reneau, "The oxygen tension field within a discrete volume of cerebral cortex," *Microvascular Research*, vol. 13, no. 2, pp. 233–240, mar 1977.

[166] H. Metzger and S. Heuber, "Local oxygen tension and spike activity of the cerebral grey matter of the rat and its response to short intervals of O2 deficiency or CO2 excess," *Pflügers Archiv European Journal of Physiology*, vol. 370, no. 2, pp. 201–209, 1977.

[167] R. Pittman, "Oxygen Transport," in *Regulation of Tissue Oxygenation*. Morgan & Claypool Life Sciences, 2011, ch. 4.

[168] D. Garcia-Gonzalez, J. Jayamohan, S. N. Sotiropoulos, S. H. Yoon, J. Cook, C. R. Siviour, A. Arias, and A. Jérusalem, "On the mechanical behaviour of PEEK and HA cranial implants under impact loading," *Journal of the Mechanical Behavior of Biomedical Materials*, vol. 69, pp. 342–354, may 2017.

[169] D. Garcia-Gonzalez, N. S. Race, N. L. Voets, D. R. Jenkins, S. N. Sotiropoulos, G. Acosta, M. Cruz-Haces, J. Tang, R. Shi, and A. Jérusalem, "Cognition based bTBI mechanistic criteria; a tool for preventive and therapeutic innovations," *Scientific Reports*, vol. 8, no. 1, p. 10273, 2018.

[170] J. Weickenmeier, M. Jucker, A. Goriely, and E. Kuhl, "A physics-based model explains the prion-like features of neurodegeneration in Alzheimer's disease, Parkinson's disease, and amyotrophic lateral sclerosis," *Journal of the Mechanics and Physics of Solids*, vol. 124, pp. 264–281, mar 2019.

[171] K. C. J. Compagne, A. M. M. Boers, H. A. Marquering, O. A. Berkhemer, A. J. Yoo, L. F. M. Beenen, R. J. van Oostenbrugge, W. van Zwam, Y. B. W. E. M. Roos, C. B. Majoie, A. C. G. M. van Es, A. van der Lugt, D. W. J. Dippel, and H. Lingsma, "Follow-up infarct volume as a mediator of endovascular treatment effect on functional outcome in ischaemic stroke," *European Radiology*, vol. 29, no. 2, pp. 736–744, feb 2019.

[172] B. G. Anderson and W. D. Anderson, "Shunting in intracranial microvasculature demonstrated by sem of corrosion-casts," *American Journal of Anatomy*, vol. 153, no. 4, pp. 617–624, dec 1978.

[173] M. A. De Georgia, "Brain Tissue Oxygen Monitoring in Neurocritical Care," *Journal of Intensive Care Medicine*, vol. 30, no. 8, pp. 473–483, dec 2015.

[174] T. Georgakopoulou, A.-E. van der Wijk, E. N. Bakker, and E. VanBavel, "Recovery of Hypoxic Regions in a Rat Model of Microembolism," *Journal of Stroke and Cerebrovascular Diseases*, vol. 30, no. 6, p. 105739, jun 2021.

[175] J. Meixensberger, "Brain tissue oxygen guided treatment supplementing ICP/CPP therapy after traumatic brain injury," *Journal of Neurology, Neurosurgery & Psychiatry*, vol. 74, no. 6, pp. 760–764, jun 2003.

[176] T. F. Bardt, A. W. Unterberg, R. Härtl, K. L. Kiening, G. H. Schneider, and W. R. Lanksch, "Monitoring of Brain Tissue PO2 in Traumatic Brain Injury: Effect of Cerebral Hypoxia on Outcome," in *Intracranial Pressure and Neuromonitoring in Brain Injury.* Vienna: Springer Vienna, 1998, pp. 153–156.

[177] R. Hirschi, G. W. J. Hawryluk, J. L. Nielson, J. R. Huie, L. L. Zimmermann, R. Saigal, Q. Ding, A. R. Ferguson, and G. Manley, "Analysis of high-frequency PbtO2 measures in traumatic brain injury: insights into the treatment threshold," *Journal of Neurosurgery*, vol. 131, no. 4, pp. 1216–1226, oct 2019.

[178] J. M. Schmidt, S.-B. Ko, R. Helbok, P. Kurtz, R. M. Stuart, M. Presciutti, L. Fernandez, K. Lee, N. Badjatia, E. S. Connolly, J. Claassen, and S. A. Mayer, "Cerebral Perfusion Pressure Thresholds for Brain Tissue Hypoxia and Metabolic Crisis After Poor-Grade Subarachnoid Hemorrhage," *Stroke*, vol. 42, no. 5, pp. 1351–1356, may 2011.

[179] R. L. Hoiland, P. N. Ainslie, C. L. Wellington, J. Cooper, S. Stukas, S. Thiara, D. Foster, N. A. Fergusson, E. M. Conway, D. K. Menon, P. Gooderham, V. Hirsch-Reinshagen, D. E. Griesdale, and M. S. Sekhon, "Brain Hypoxia Is Associated With Neuroglial Injury in Humans Post–Cardiac Arrest," *Circulation Research*, vol. 129, no. 5, pp. 583–597, aug 2021.

[180] B. C. Campbell, P. J. Mitchell, T. J. Kleinig, H. M. Dewey, L. Churilov, N. Yassi, B. Yan, R. J. Dowling, M. W. Parsons, T. J. Oxley, T. Y. Wu, M. Brooks, M. A. Simpson, F. Miteff, C. R. Levi, M. Krause, T. J. Harrington, K. C. Faulder, B. S. Steinfort, M. Priglinger, T. Ang, R. Scroop, P. A. Barber, B. McGuinness, T. Wijeratne, T. G. Phan, W. Chong, R. V. Chandra, C. F. Bladin, M. Badve, H. Rice, L. de Villiers, H. Ma, P. M. Desmond, G. A. Donnan, and S. M. Davis, "Endovascular Therapy for Ischemic Stroke with Perfusion-Imaging Selection," *New England Journal of Medicine*, vol. 372, no. 11, pp. 1009–1018, mar 2015.

[181] T. G. Jovin, J. L. Saver, M. Ribo, V. Pereira, A. Furlan, A. Bonafe, B. Baxter, R. Gupta, D. Lopes, O. Jansen, W. Smith, D. Gress, S. Hetts, R. J. Lewis, R. Shields, S. M. Berry, T. L. Graves, T. Malisch, A. Rai, K. N. Sheth, D. S. Liebeskind, and R. G. Nogueira, "Diffusion-weighted imaging or computerized tomography perfusion assessment with clinical mismatch in the triage of wake up and late presenting strokes undergoing neurointervention with Trevo (DAWN) trial methods," *International Journal of Stroke*, vol. 12, no. 6, pp. 641–652, aug 2017.

[182] A. C. Pereira, D. E. Saunders, V. L. Doyle, J. M. Bland, F. A. Howe, J. R. Griffiths, and M. M. Brown, "Measurement of Initial N-Acetyl Aspartate Concentration by Magnetic Resonance Spectroscopy and Initial Infarct Volume by MRI Predicts Outcome in Patients With Middle Cerebral Artery Territory Infarction," *Stroke*, vol. 30, no. 8, pp. 1577–1582, aug 1999.

[183] A. Boers, H. Marquering, J. Jochem, N. Besselink, O. Berkhemer, A. van der Lugt, L. Beenen, and C. Majoie, "Automated Cerebral Infarct Volume Measurement in Follow-up Noncontrast CT Scans of Patients with Acute Ischemic Stroke," *American Journal of Neuroradiology*, vol. 34, no. 8, pp. 1522–1527, aug 2013.

[184] A. Shuaib, K. Butcher, A. A. Mohammad, M. Saqqur, and D. S. Liebeskind, "Collateral blood vessels in acute ischaemic stroke: A potential therapeutic target," *The Lancet Neurology*, vol. 10, no. 10, pp. 909–921, 2011.

[185] K. Malhotra and D. S. Liebeskind, "Collaterals in ischemic stroke," *Brain Hemorrhages*, vol. 1, no. 1, pp. 6–12, mar 2020.

[186] S. D. Treadwell and B. Thanvi, "Malignant middle cerebral artery (MCA) infarction: pathophysiology, diagnosis and management," *Postgraduate Medical Journal*, jan 2010.

[187] S. Kamran, N. Akhtar, A. Alboudi, K. Kamran, A. Ahmad, J. Inshasi, A. Salam, A. Shuaib, and U. Qidwai, "Prediction of infarction volume and infarction growth rate in acute ischemic stroke," *Scientific Reports*, vol. 7, no. 1, 2017.

[188] T. D. Faizy, R. Kabiri, S. Christensen, M. Mlynash, G. Kuraitis, G. Broocks, U. Hanning, J. Nawabi, M. G. Lansberg, M. P. Marks, G. W. Albers, J. Fiehler, M. Wintermark, and J. J. Heit, "Perfusion imaging-based tissue-level collaterals predict ischemic lesion net water uptake in patients with acute ischemic stroke and large vessel occlusion," *Journal of Cerebral Blood Flow and Metabolism*, vol. 41, no. 8, pp. 2067–2075, 2021.

[189] T. D. Faizy, R. Kabiri, S. Christensen, M. Mlynash, G. M. Kuraitis, G. Broocks, F. Flottmann, M. P. Marks, M. G. Lansberg, G. W. Albers, J. Fiehler, M. Wintermark, and J. J. Heit, "Favorable Venous Outflow Profiles Correlate With Favorable Tissue-Level Collaterals and Clinical Outcome," *Stroke*, vol. 52, no. 5, pp. 1761–1767, may 2021.

[190] J. M. Olivot, M. Mlynash, M. Inoue, M. P. Marks, H. M. Wheeler, S. Kemp, M. Straka, G. Zaharchuk, R. Bammer, M. G. Lansberg, and G. W. Albers, "Hypoperfusion Intensity Ratio Predicts Infarct Progression and Functional Outcome in the DEFUSE 2 Cohort," *Stroke*, vol. 45, no. 4, pp. 1018–1023, apr 2014.

[191] A. Guenego, D. G. Marcellus, B. W. Martin, S. Christensen, G. W. Albers, M. G. Lansberg, M. P. Marks, M. Wintermark, and J. J. Heit, "Hypoperfusion Intensity Ratio Is Correlated With Patient Eligibility for Thrombectomy," *Stroke*, vol. 50, no. 4, pp. 917–922, 2019.

[192] A. de Havenon, M. Mlynash, M. A. Kim-Tenser, M. G. Lansberg, T. Leslie-Mazwi, S. Christensen, R. A. McTaggart, M. Alexander, G. Albers, J. Broderick, M. P. Marks, and J. J. Heit, "Results From DEFUSE 3: Good Collaterals Are Associated With Reduced Ischemic Core Growth but Not Neurologic Outcome," vol. 50, no. 3, pp. 632–638, mar 2019.

[193] M. Peyrounette, Y. Davit, M. Quintard, and S. Lorthois, "Multiscale modelling of blood flow in cerebral microcirculation: Details at capillary scale control accuracy at the level of the cortex," *PLOS ONE*, vol. 13, no. 1, p. e0189474, jan 2018.

[194] S. Buch, Y. Wang, M.-G. Park, P. K. Jella, J. Hu, Y. Chen, K. Shah, Y. Ge, and E. M. Haacke, "Subvoxel vascular imaging of the midbrain using USPIO-Enhanced MRI," *NeuroImage*, vol. 220, p. 117106, oct 2020.

[195] "IXI Dataset." [Online]. Available: https://brain-development.org/ixi-dataset/

[196] K.-A. Mardal, M. E. Rognes, T. B. Thompson, and L. M. Valnes, "Getting started: from T1 images to simulation," in *Mathematical Modeling of the Human Brain*, 2022, pp. 23–46.

[197] B. Fischl, "FreeSurfer," *NeuroImage*, vol. 62, no. 2, pp. 774–81, aug 2012.

[198] K.-A. Mardal, M. E. Rognes, T. B. Thompson, and L. M. Valnes, "Working with magnetic resonance images of the brain," in *Mathematical Modeling of the Human Brain*, 2022, pp. 7–21.

[199] T. Józsa, J. Petr, A. M. Wink, F. Barkhof, H. Mutsaerts, and S. Payne, "Generating virtual brains for MRI-based 3D cerebral blood flow simulations," in *ISMRM '21: Proceedings of the ISMRM 29th Annual Meeting and Exhibition*, vol. 29, 2021, p. 4147.

[200] T. Józsa, J. Petr, S. Payne, and H. Mutsaerts, "MRI-based parameter inference for cerebral perfusion modelling in health and ischaemic stroke," *Computers in Biology and Medicine*, vol. 166, p. 107543, nov 2023.

[201] J. D. Nielsen, K. H. Madsen, O. Puonti, H. R. Siebner, C. Bauer, C. G. Madsen, G. B. Saturnino, and A. Thielscher, "Automatic skull segmentation from MR images for realistic volume conductor models of the head: Assessment of the state-of-the-art," *NeuroImage*, vol. 174, pp. 587–598, jul 2018.

[202] D. P. O'Neill, T. Peng, P. Stiegler, U. Mayrhauser, S. Koestenbauer, K. Tscheliessnigg, and S. J. Payne, "A Three-State Mathematical Model of Hyperthermic Cell Death," *Annals of Biomedical Engineering*, vol. 39, no. 1, pp. 570–579, jan 2011.